

UNIVERSITY OF OKLAHOMA  
GRADUATE COLLEGE

RADAR CROSS SECTION ANALYSIS OF TORNADIC DEBRIS

A THESIS  
SUBMITTED TO THE GRADUATE FACULTY  
in partial fulfillment of the requirements for the  
Degree of  
MASTER OF SCIENCE

By  
JAVIER LUJAN  
Norman, Oklahoma  
2016

RADAR CROSS SECTION ANALYSIS OF TORNADIC DEBRIS

A THESIS APPROVED FOR THE  
SCHOOL OF ELECTRICAL AND COMPUTER ENGINEERING

BY

---

Dr. Caleb J. Fulton, Chair

---

Dr. Robert Palmer

---

Dr. Boon-Leng Cheong



## Table of Contents

<b>List of Tables</b>	<b>vi</b>
<b>List of Figures</b>	<b>vii</b>
<b>Abstract</b>	<b>xii</b>
<b>1 Introduction</b>	<b>1</b>
<b>2 Radar Cross Section Theory</b>	<b>9</b>
2.1 Introduction . . . . .	9
2.2 RCS Definition . . . . .	11
2.3 Scattering Regimes . . . . .	13
2.4 Plate Scattering . . . . .	17
2.5 Cylinder Scattering . . . . .	20
2.6 Conclusion . . . . .	24
<b>3 Radar Cross Section Simulations</b>	<b>25</b>
3.1 Introduction . . . . .	25
3.2 Analytical Method in MATLAB . . . . .	26
3.3 FEKO Simulations . . . . .	35
3.4 HFSS Simulations . . . . .	57
3.5 Conclusion . . . . .	64
<b>4 Radar Cross Section Measurements</b>	<b>66</b>
4.1 Introduction . . . . .	66
4.2 Monostatic vs Quasi-Monostatic Measurements . . . . .	68
4.3 Calibration . . . . .	69
4.4 Chamber Characteristics . . . . .	71
4.5 Results . . . . .	74
4.6 Conclusion . . . . .	80
<b>5 Multiple Scattering</b>	<b>81</b>
5.1 Introduction . . . . .	81
5.2 Cylinder Multiple Scattering . . . . .	82



5.3	Plate Multiple Scattering . . . . .	96
5.4	Conclusion . . . . .	102
<b>6</b>	<b>Conclusion</b>	<b>104</b>
	<b>References</b>	<b>106</b>
	<b>Appendix A Derivations</b>	<b>110</b>
A.1	Equivalence of Transmit and Receive Antennas . . . . .	110
	<b>Appendix B Code</b>	<b>113</b>
B.1	Leaf RCS . . . . .	113
B.2	Chamber Measurements RCS . . . . .	119
B.3	Cylinder Multiple Scattering . . . . .	122
B.4	Plate Multiple Scattering . . . . .	125

## List of Tables

3.1	Dielectric properties for the scatterers to be modeled. The leaf's dielectric properties were obtained at 80% gravimetric moisture content at 25°C while the wood dielectric constants were for 13% gravimetric moisture content at 25°C. . . . .	30
3.2	Dimensions for the wooden targets to be simulated and measured in meters. . . . .	43

## List of Figures

1.1	A screenshot of the radar simulator. In this figure, the simulated space can be seen with a simulated tornado. The white and blue dots are the injected hydrometeors while the purple and green objects are simulated debris. A simulated radar beam sweeps through the volume and records the polarimetric products produced by the simulated tornado. [6]. . . . .	5
2.1	Normalized RCS of a sphere as a function of normalized circumference showing the different scattering regimes. Scatterers may fall in the Rayleigh regime (towards the left of the plot), Mie regime (towards the middle of the plot), or optical regime (towards the right of the plot) [17]. . . . .	14
3.1	Orientation of the simulated leaf in global coordinates. For all simulations, the leaf and other simulated debris have their longest dimension along the $y$ axis while their face is normal to the $z$ axis. . .	27
3.2	Coordinate system rotation using Euler rotation. The angles $\alpha$ , $\beta$ , and $\gamma$ control the rotation to achieve any orientation in 3D space. Angle $\alpha$ rotates the coordinate system around the $z$ axis. Next, the $\beta$ angle rotates the coordinate system around the $y'$ axis. And finally, the $\gamma$ angle rotates the coordinate system around the $z''$ axis to finally obtain a $x''' - y''' - z'''$ coordinate system [6]. . . . .	28
3.3	RCS pattern of simulated leaf for HH-pol. Notice the contribution from the cylinder's end-caps, creating small lobes along the $y$ axis. The polarization is perpendicular to the cylinder and the side of the sheet, creating low scattering along the $y - z$ plane. . . . .	32
3.4	RCS pattern of simulated leaf for VV-pol. Contribution from the cylinder's end-caps can be seen again with the additional contribution along the $y - z$ plane from the leaf's side and cylinder due to the polarization being parallel to the leaf side. . . . .	33
3.5	RCS pattern of simulated leaf for HV-pol. Some cross polarization contribution can be seen here. As expected, cross polarization is larger a broadside. . . . .	34

3.6	RCS pattern of FEKO simulated leaf for HH-pol. The contributions from the end-caps of the cylinder can be seen here just as seen in the MATLAB simulations. . . . .	37
3.7	RCS pattern of FEKO simulated leaf for VV-pol. The cylinder's end-cap contribution can be seen here as well. But notice that the cylinder's and leaf's side contribution is not seen here around the $y - z$ plane as seen in the MATLAB simulation. . . . .	38
3.8	RCS pattern of FEKO simulated leaf for HV-pol. A small cross polarization contribution is shown. . . . .	39
3.9	RCS pattern of FEKO and MATLAB simulated leaf for HH-pol. The RCS pattern shapes agree between MATLAB and FEKO but the magnitude of the pattern is lower for MATLAB. . . . .	41
3.10	RCS pattern of FEKO and MATLAB simulated leaf for VV-pol. Similar to the previous figure, the pattern shapes between FEKO and MATLAB agree but MATLAB produces a lower magnitude pattern. . . . .	42
3.11	RCS pattern of FEKO simulated wood board 1 for HH-pol. A large peak is centered at broadside and it is stretched in the $x$ axis due to the difference in the ratio of dimensions along the length and width of the board. . . . .	44
3.12	RCS pattern of FEKO simulated wood board 1 for VV-pol. The RCS pattern is similar to that of the HH polarization. . . . .	45
3.13	RCS pattern of FEKO simulated wood board 1 for HV-pol. A small cross polarization contribution can be seen. . . . .	46
3.14	RCS pattern of FEKO simulated wood board 2 for HH-pol. This wooden board is thicker and shorter, creating an even more elongated RCS peak at broadside along the $x$ axis. . . . .	47
3.15	RCS pattern of FEKO simulated wood board 2 for VV-pol. Now that the polarization is parallel to the largest dimension of the target, the RCS pattern near broadside becomes even more elongated and the RCS levels on the sides are higher. . . . .	48
3.16	RCS pattern of FEKO simulated wood board 2 for HV-pol. A small cross polarization contribution is seen. . . . .	49
3.17	RCS pattern of FEKO simulated wood board 3 for HH-pol. The peak RCS level is slightly larger than that of wooden board 2 due to its slightly larger dimensions. . . . .	50
3.18	RCS pattern of FEKO simulated wood board 3 for VV-pol. RCS pattern similar to that of the HH polarization. . . . .	51
3.19	RCS pattern of FEKO simulated wood board 3 for HV-pol. . . . .	52
3.20	RCS pattern of FEKO simulated wood sheet for HH-pol. This is the largest target and it can be seen that it has the highest RCS, the most number of lobes, and the most number of nulls. . . . .	53

3.21	RCS pattern of FEKO simulated wood sheet for VV-pol. The RCS pattern is almost identical to that of the HH polarization. . . . .	54
3.22	RCS pattern of FEKO simulated wood sheet for HV-pol. A small contribution from the cross polarization is seen here. . . . .	55
3.23	RCS pattern of HFSS simulated leaf for HH-pol. RCS pattern is similar to that of MATLAB and FEKO for the same polarization, where the RCS contribution by the cylinder's end-caps can be seen along the $y$ axis. . . . .	59
3.24	RCS pattern of HFSS simulated leaf for VV-pol. Notice that the cylinder provides a contribution to the RCS when the polarization is parallel to it as previously seen in the MATLAB simulation but was not present in the FEKO simulation. . . . .	60
3.25	RCS pattern of HFSS simulated leaf for HV-pol. A small cross polarization contribution can be seen here and it is not entirely negligible at certain angles near broadside. . . . .	61
3.26	RCS pattern of HFSS simulated wood board 2 for HH-pol. RCS pattern is almost identical to the FEKO RCS pattern. . . . .	62
3.27	RCS pattern of HFSS simulated wood board 2 for VV-pol. RCS pattern is almost identical to the FEKO RCS pattern. . . . .	63
4.1	Inside the far-field anechoic chamber. The transmit and receive antennas are located in the far right of the picture, while the target to be measured rests in the pedestal on the left of the picture. . . . .	68
4.2	Difference between the monostatic and quasi-monostatic RCS configuration of a sphere. While the VV polarization exhibits the largest difference, both polarizations exhibit a negligible contribution from the quasi-monostatic configuration. . . . .	69
4.3	12 inch diameter calibration sphere. A metallic perfect sphere is used here for chamber calibration procedures since its RCS is independent of aspect angle. . . . .	70
4.4	Calibration by taking the difference between the measured and calculated RCS of a 12 inch diameter calibration sphere. The difference is the combined effective loss from the chamber, cables, and instrumentation. This loss is added to future measurements to obtain the target's true RCS. . . . .	70
4.5	RCS difference of 2 sphere measurements taken at different times. Measurements taken within a day exhibit very little difference while measurements taken a day apart have a much larger difference that may impact the overall result. . . . .	73
4.6	Picture of Wood board 1 to be measured. Length: 0.2794 m. Width: 0.1397 m. Thickness: 0.01587 m. . . . .	74

4.7	Comparison between measurement and FEKO simulation of wood board 1. Agreement between measurement and simulation is excellent at and near broadside with the larger discrepancies being around grazing angle. . . . .	75
4.8	Picture of Wood board 2 to be measured. Length: 0.3683 m. Width: 0.0889 m. Thickness: 0.0381 m. . . . .	75
4.9	Comparison between measurement and FEKO simulation of wood board 2. There is discrepancy in the magnitude between the measured and calculated pattern throughout all angles. Misalignment of target to the main beam may be the cause. . . . .	76
4.10	Picture of Wood board 3 to be measured. Length: 0.3937 m. Width: 0.1397. Thickness: 0.0381 m. . . . .	76
4.11	Comparison between measurement and FEKO simulation of wood-board 3. Magnitude discrepancies can be seen again between the measurement and the simulation, thought to be from misalignment between target and antenna beam. The patterns, however, are consistent between them. . . . .	77
4.12	Picture of Wood sheet to be measured. Length: 0.4572 m. Width: 0.4572. Thickness: 0.009525 m. . . . .	77
4.13	Comparison between measurement and FEKO simulation of wood sheet. Just like with Wood board 1, the patterns between the measurement and simulation agree well throughout most angles except near grazing angle. . . . .	78
5.1	MATLAB RCS simulation of 2 cylinders with no multiple scattering taken into account (3D view). The RCS changes as a function of distance but due to the constructive/destructive interference at every time the dipoles are placed $\lambda/4$ or $\lambda/2$ distance apart. The RCS does increase as a function of size but this is to be expected since larger objects create larger RCS levels. . . . .	86
5.2	MATLAB RCS simulation of 2 cylinders with no multiple scattering taken into account (2D view). Same as Figure 5.1 but in 2D for easier viewing. . . . .	87
5.3	MATLAB RCS simulation of 2 cylinders with multiple scattering taken into account (3D view). In this plot, the effects of multiple scattering can be seen clearly for the RCS of the dipoles decreases as the distance between them increases. This can be seen for larger dipoles and multiple scattering has little effect with smaller dipoles. . . . .	88
5.4	MATLAB RCS simulation of 2 cylinders with no multiple scattering taken into account (2D view). Same as Figure 5.3 but in 2D for easier viewing. . . . .	89

5.5	Difference between RCS simulation of 2 cylinders with and without multiple scattering (3D view). Notice how the larger differences occur for larger dipoles as the distance decreases between them. . . .	90
5.6	Difference between RCS simulation of 2 cylinders with and without multiple scattering (2D view). Same as Figure 5.5 but in 2D for easier viewing. . . . .	91
5.7	Placement of simulated dipoles in a global coordinate system. The first dipole is placed at the origin while the second dipole is placed 50 cm away in the positive $z$ axis. . . . .	93
5.8	MATLAB and FEKO Scattering simulations from 2 dipoles placed 50 cm apart. The agreement between both simulations is excellent, meaning that the MATLAB model is functional and accurate. . . .	94
5.9	MATLAB and FEKO Scattering simulations from 2 arbitrarily rotated and placed dipoles. There is good agreement at the larger lobes and large discrepancies around the nulls. . . . .	95
5.10	Geometry of the simulated dihedral reflector. The first plate is placed on the origin and rotated 90 degrees while the second plate is placed 3 cm along the positive $x$ axis and 3 cm along the negative $z$ axis without rotating the plate. . . . .	97
5.11	RCS pattern for the dihedral simulated in MATLAB and FEKO using PO. The FEKO simulation using PO failed to capture the multiple scattering. . . . .	98
5.12	RCS pattern for the dihedral simulated in MATLAB and FEKO using MoM. Here FEKO did capture the multiple scattering effect while the MATLAB result does not match it well. A small lobe is seen at 45 degrees but the magnitude is too low. . . . .	99
5.13	Geometry of the simulated separated dihedral reflector. The first plate is rotated 90 degrees and placed 10 cm along the positive $z$ axis. The second plate is not rotated and placed 10 cm along the positive $x$ axis. . . . .	100
5.14	RCS pattern for the separated dihedral simulated in MATLAB. The peak at 45 degrees agrees better than in Figure 5.12 but some discrepancies can still be seen especially around the nulls. . . . .	101

## **Abstract**

Weather radar is a powerful tool for detecting hazardous weather that may impact citizens. Among these dangerous weather phenomena, tornadoes have a high potential for destruction of property and loss of life due to its rapid formation. It has been observed that a tornado may produce a Tornadic Debris Signature (TDS) when producing heavy damage. To get a better understanding of the TDS, a tornado simulator was created by the Radar Innovations Laboratory where polarimetric variables are simulated by simulating a tornado with hydrometeors and debris and simulating a radar beam scanning said tornado. Scattering by hydrometeors is well known but not for debris as it is random in orientation and shape. To obtain accurate polarimetric products, accurate scattering from the debris is needed.

In order to provide the simulator with accurate scattering from debris, the Radar Cross Section (RCS) from simple objects such as wooden boards and a leaf are simulated using electromagnetic solvers. To validate the simulations, measurements of the simulated debris are taken in an anechoic chamber and compared.

The radar simulator does not take multiple scattering into effect which may impact the results of the polarimetric products. To explore the possibility of needing multiple scattering in the tornado simulator, the multiple scattering by small cylinders and plates is analyzed by using closed analytical solutions by using reaction and reciprocity theorem on the cylinders and Physical Optics (PO) for the plates.



# Chapter 1

## Introduction

With the recent advent of dual-polarization weather radars, a new wealth of information is now available to researchers in comparison to the data provided by past single-polarization radar systems. Single-polarization weather radars have three useful output products, horizontal reflectivity factor  $Z_H$ , which is determined by measuring the strength of the returned signal, radial velocity  $V_r$ , which is determined by the Doppler shift in the radar echo return and shows the radial component of the target's velocity, and spectrum width  $\sigma_v$  which describes the dispersion speed components in a resolution volume [1], [2]. These products are certainly useful to roughly estimate precipitation rate and observe how fast storms move [1], [3], but they do not provide any more useful information about the weather phenomena of interest. Dual-polarization radars, on the other hand, have many other useful products thanks to polarization diversity such as horizontal reflectivity  $Z_{HH}$ , vertical reflectivity  $Z_{VV}$ , differential reflectivity  $Z_{DR}$ , correlation coefficient  $\rho_{HV}$ , and specific differential phase  $K_{DP}$ . Both horizontal and vertical reflectivity factors show how much backscattered power is received at the radar for each polarization, respectively [1]–[3]:

$$Z_{H/V} = 10 \log_{10} \left( \frac{z_{H/V}}{1 \text{mm}^6/\text{m}^3} \right). \quad (1.1)$$

where

$$z_{H/V} = \frac{1024 l n(2) P_r r^2 \lambda^2}{\pi^3 P_t g^2 \theta \phi c \tau |K|^2 l}. \quad (1.2)$$

where  $P_r$  is the power received,  $r$  is the distance from the radar to the target,  $\lambda$  is the wavelength,  $P_t$  is the power transmitted,  $g$  is the gain of the antenna,  $\theta$  and  $\phi$  are the horizontal and vertical beamwidth,  $c$  is the speed of light,  $\tau$  is the pulse length,  $K$  is the complex index of refraction, and  $l$  is the attenuation.

Differential reflectivity is the logarithm of the ratio of  $Z_{HH}$  over  $Z_{VV}$  [1]–[3].

$$Z_{DR} = 10 \log_{10} \left( \frac{z_H}{z_V} \right). \quad (1.3)$$

where  $z_H$  is the horizontal reflectivity factor and  $z_V$  is the vertical reflectivity factor in linear units. A positive value of  $Z_{DR}$  indicates stronger return from the horizontal polarized signal and negative  $Z_{DR}$  indicates a stronger return from the vertical signal, providing information about the orientation of the targets. Correlation coefficient tells us the behavior of the H and V pulses in a resolution volume [1]–[3]. The values of correlation coefficient are 1 for drizzle and rain, 0.8 for hail, and lower for non-hydrometeor targets so it is very useful for determining whether the scatterers within a resolution volume are hydrometeors or not.

$$\rho_{HV} = \frac{\langle S_{vv} S_{hh}^* \rangle}{\langle |S_{hh}|^2 \rangle^{1/2} \langle |S_{vv}|^2 \rangle^{1/2}}. \quad (1.4)$$

Specific differential phase tells us how much the phase from the horizontal signal lags/leads from the vertical signal as a function of range [1]–[3].

$$K_{\text{DP}} = \frac{\phi_{\text{DP}}(r_2) - \phi_{\text{DP}}(r_1)}{2(r_2 - r_1)}. \quad (1.5)$$

where  $\phi_{\text{DP}}$  is the differential phase

$$\phi_{\text{DP}} = \phi_{\text{HH}} - \phi_{\text{VV}}. \quad (1.6)$$

where  $\phi_{\text{HH}}$  is the horizontal co-pol phase and  $\phi_{\text{VV}}$  is the vertical co-pol phase. It is dependent on scatterer shape and orientation and it is helpful for obtaining accurate rainfall rates. With these extra polarimetric variables hydrometeor classification is possible, rainfall rates can be estimated with better accuracy, and non-hydrometeors such as biota, clutter, and debris can also be identified [3], [4]. Each precipitation type has a unique polarimetric signature thanks to their physical nature. Raindrops are mostly spherical and become more oblate as they grow in size due to drag and internal forces as they fall through the air [4]. They are characterized by having high  $\rho_{\text{HV}}$ , higher  $Z_{\text{H}}$  and  $Z_{\text{DR}}$  as the drops grow larger [1]–[4]. Snowflakes come in different shapes in sizes from plate like structures to needles so their radar characteristics range quite a bit [4]. Because the mechanisms that create hydrometeors are very well known, the dual polarization products, such as reflectivity, differential reflectivity, and correlation coefficient, are known and each type of precipitation has a particular radar signature. In the case of tornadoes, however, not only are hydrometeors observed in the resolution volume but debris may also be present as the tornado lifts objects into the air as it travels over and wreaks destruction to vegetation and man-made structures. Debris lofted by the tornado, on the other hand, is random in shape, the orientation is unknown, and the dielectric properties are unknown so it is not known what to expect from the polarimetric variables for a tornado containing debris. The polarimetric signature that is observed

for a tornado containing debris is called the Tornadic Debris Signature (TDS). Studies have shown that low to negative  $Z_{DR}$  and low  $\rho_{HV}$  around the vortex has been commonly observed in the TDS [5]. Low  $\rho_{HV}$  happens at lower scan elevations and increases at higher elevations while  $Z_{HH}$  is highest on the lower elevations scans [5]. This is believed to be due to large number of debris being concentrated at the lowest elevations as it's being picked up by the tornadic winds and then having debris centrifuge and fall out of the tornado at higher elevations. The large diversity of debris shape, aspect ratio, and orientation of the debris contribute to this low  $\rho_{HV}$  present in the TDS and because debris pieces may be larger than raindrops it contributes to the observed high  $Z_{HH}$ . If the debris' orientation is randomly distributed, a near zero average  $Z_{DR}$  would be expected in the tornado but observations have shown that negative  $Z_{DR}$  is sometimes present in the TDS [5]. It is hypothesized that the tornadic winds are responsible for a preferred vertical alignment within the debris created by the aerodynamics and drag forces exerted on it. Another hypothesis is that there may be mechanisms in the electromagnetic scattering generated by the debris that may cause a negative  $Z_{DR}$  return. To help explain the TDS phenomenon, a computerized tornado simulator was created by the Advanced Radar Research Center [6].

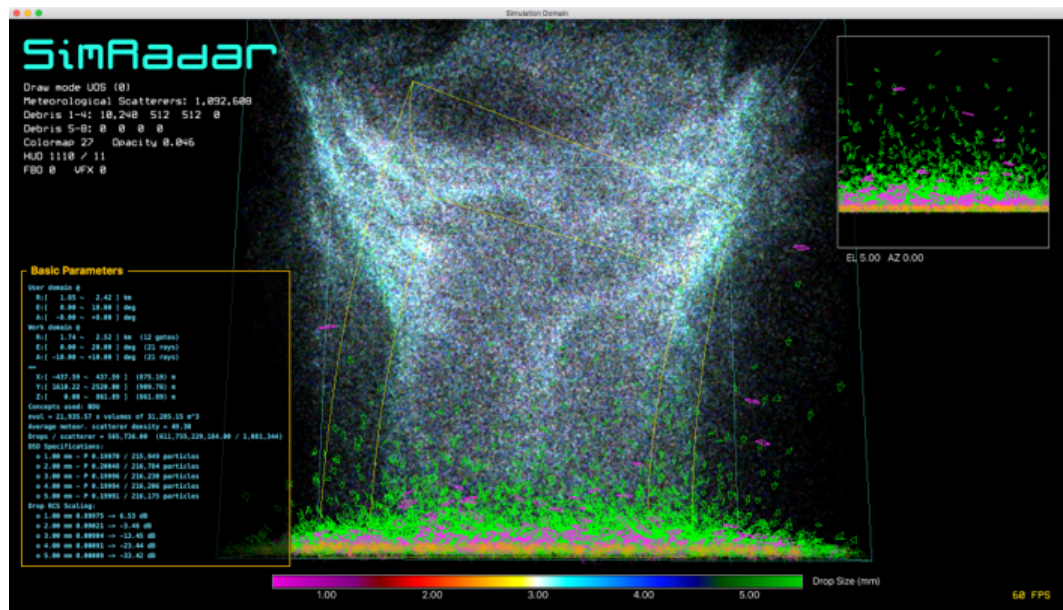


Figure 1.1: A screenshot of the radar simulator. In this figure, the simulated space can be seen with a simulated tornado. The white and blue dots are the injected hydrometeors while the purple and green objects are simulated debris. A simulated radar beam sweeps through the volume and records the polarimetric products produced by the simulated tornado. [6].

This simulator can be populated with hydrometeors, debris, and fed with wind fields including multiple vortex tornadoes and obtain the computed polarimetric signals. It is important to note, however, that multiple scattering was not implemented in the simulator and its importance will be discussed in later chapters.

An important parameter that the simulator uses is the Radar Cross Section (RCS) of the objects in the simulation. The RCS of an object determines how much power is scattered back to the radar and it depends on the frequency and polarization of the radar, the size, orientation, and electric properties of the target. The scattering of raindrops has already been well described by using the T-Matrix solution which is used for rotationally symmetric and dielectric bodies [3]. To compute the scattering and RCS of debris, other methods must be employed due to their random shapes.

The present thesis will explore the RCS of several common objects that are thought to be lofted by tornadoes such as leaves from trees and wooden boards. This enables the creation of an RCS library for the tornado simulator so that it may populate the simulation space with debris and its appropriate RCS pattern. Figure 1.1 shows the how the RCS library is created and implemented. RCS measurements of several pieces of debris are taken to obtain a base truth. Computational RCS models of the measured debris are compared to the measurements to validate the results while the analytical models are compared to the simulations to validate approximations used to simplify the problem. After validation, the simulated RCS patterns are exported into a file to be added to the RCS library for the tornado simulator.

The RCS of these objects are simulated by electromagnetic solvers HFSS and FEKO and mathematically in MATLAB. These objects will remain simple shape-wise because the mathematical complexity for the RCS of an object increases as the

complexity of the object's geometry increases. Moreover, simple shapes take less time and computational resources when simulating in the electromagnetic solvers. A tornado not always comes across man-made structures so the source of the TDS from some cases comes from the local vegetation. Leaves are a common component of vegetation in the mid-latitudes, leaves can create a TDS if enough are ingested into the tornado [5]. Because leaves are relatively simple in shape and geometry its scattering characteristics have been measured and modeled [7]. The leaf itself can be modeled as a thin resistive sheet where its reflection coefficient and dielectric constant is a function of gravimetric moisture content which is the amount of water contained in the leaf [7], [8]. In this thesis leaves will be part of the modeled debris which is a sum of the scattering by a thin dielectric sheet in addition to the scattering by a dielectric cylinder which will act as the stem of the leaf. The stem is added to ensure a more accurate representation of the leaf.

Measurements of the RCS of the objects used for simulation are taken at the laboratory's far field anechoic chamber to validate the simulated RCS of the objects. To simplify matters in the tornado simulator, multiple scattering was not implemented and only direct scattering was developed. Multiple scattering is a phenomenon that happens in reality when multiple scatterers are present and evidence of that is in the 3 body scattering as seen with hail shafts [9]. Because of this, multiple scattering can be important as it may have a significant contribution in the radar return signal. For the last chapter of this thesis, first-order multiple scattering between pieces of debris is explored and analyzed.

In chapter 2 the theory behind RCS is explored to give the reader more familiarity with the definition of RCS and what it entails. Chapter 3 is concerned with the simulations of the debris RCS patterns by using analytical and computational methods. Chapter 4 reveals the measurements of the simulated debris and are compared

to validate the solutions from the simulations. In chapter 5, the first order multiple scattering by simple objects is explored to determine if it is necessary to implement in the tornado simulator. And in the last chapter, chapter 6, the conclusion and future work for this thesis is presented.



## **Chapter 2**

### **Radar Cross Section Theory**

#### **2.1 Introduction**

Radars were invented in the early 20th century. The term Radar was coined in the 1940's during World War 2 as an acronym for RAdio Detection And Ranging and what propelled its fast development was the need for detection and early warning from enemy airplanes. What make radar systems attractive as a detection tool is the advantage that they can observe and track targets from very large distances, can still track and detect through clouds, and do not rely on daylight as an illumination source so it can operate anytime. During their observations during the war, operators worked on estimating the attenuation by clouds and precipitation, strongly indicating that radars at the time detected weather echoes [1]. After the war was over, military surplus was made available to civilians giving the scientific community a chance to experiment with radars to detect weather echoes [2].

The modern weather radar used today in the United States is called the Weather Surveillance Radar 1988 Doppler (WSR-88D). The dense network of weather radars cover most of the mainland and are used to keep track of weather systems and help meteorologists warn citizens when hazardous weather is imminent. The WSR-88D operates at a frequency of 2.8 GHz which is located in the microwave range known

as S-Band. At S-Band, attenuation of the electromagnetic wave as it propagates through the air is low which means that the transmitted wave will lose little power as it travels through the atmosphere, giving the radar the ability to detect echoes at longer distances. Its native resolution is rather coarse, which is 1000 m in range for reflectivity and 250 m for velocity and 1 degree in azimuth, but for surveillance purposes it is sufficient [10].

For radars to detect a target, the target has to scatter some of the incident power towards the radar. By deriving the radar range equation for a point target it becomes easier to observe what parameters dictate the amount of power received by the radar. First it is assumed that an isotropic antenna radiates a transmitted power  $P_t$ . As the antenna radiates power, the power density  $S_i$  will decay as it travels through space by a factor of  $4\pi R^2$ , where  $R$  is the range, so that [11]:

$$S_i = \frac{P_t}{4\pi R^2}. \quad (2.1)$$

Antennas are not isotropic in practice and have a gain so a more realistic power density would be to the gain of the transmit antenna  $G_t$  into the transmitted power:

$$S_i = \frac{P_t G_t}{4\pi R^2}. \quad (2.2)$$

The power intercepted by the target will be the incident power density times the echo area of the target  $\sigma$ :

$$P_i = \frac{P_t G_t \sigma}{4\pi R^2}. \quad (2.3)$$

The power density of the scattered wave  $S_r$  radiates in an isotropic manner so that:

$$S_r = \frac{P_t G_t \sigma}{(4\pi)^2 R^4}. \quad (2.4)$$

The power at the receiver will depend on the effective area of the antenna  $A_e$  which is:

$$A_e = \frac{G_r \lambda^2}{4\pi}. \quad (2.5)$$

where  $\lambda$  is the radar wavelength. By multiplying the scattered power density times the effective area of the antenna, we get:

$$P_r = \frac{P_t G_t G_r \lambda^2 \sigma}{(4\pi)^3 R^4}. \quad (2.6)$$

Because the radar of interest is a monostatic radar, meaning that the transmit and receive antenna are collocated, the gain is the same so the final form of the radar equation is:

$$P_r = \frac{P_t G^2 \lambda^2 \sigma}{(4\pi)^3 R^4}. \quad (2.7)$$

The amount of power scattered is dictated by several parameters as seen from the radar equation. Most of the parameters for the received power are fixed with the exception of the range and a radar parameter called the echo area, or RCS,  $\sigma$ . It is on this latter parameter, the RCS, that this thesis focuses on.

## 2.2 RCS Definition

Radar Cross Section is the amount of scattered power that a target reflects back at the radar. The IEEE defines RCS as “a measure of reflective strength of a target

defined as  $4\pi$  times the ratio of the power per unit solid angle scattered in a specified direction to the power per unit area in a plane wave incident on the scatterer from a specified direction” [11]. A more intuitive definition is that the RCS is the ratio of the incident power density to the power density scattered by an object. It is effectively the echo area of the target and dictates how much power it scatters back. For defense applications this parameter is of utmost importance as it determines the visibility of a target to a radar [12]. For weather radar applications however, it is related to how much power the hydrometeors scatter back to the radar, yielding a different reflectivity factor depending on the size and concentration of the hydrometeors [1], [3].

The larger the RCS of an object is the more power it will scatter back to the radar and it can be shown by looking back at the radar equation previously derived and realize there is a direct relationship between power received and RCS. The RCS of the target itself depends on many factors such as electrical size and material properties as we will see later.

The WSR-88D is a monostatic radar, which means that the transmit and receive antennas are collocated. The scattering detected by a monostatic radar system is called backscattering, meaning that the illuminated target scatters energy back in the direction of the incident wave. Bistatic radars, on the other hand, have the receive and transmit antennas in different locations. Because the present thesis only deals with the WSR-88D radar, only backscattering and monostatic RCS is explored.

The general equation for the RCS is [13]:

$$\sigma = \lim_{R \rightarrow \infty} 4\pi R^2 \frac{|E_s|^2}{|E_i|^2}. \quad (2.8)$$

The RCS is the ratio of the scattered power density over the incident power density

on the target. The strength of the scattered power from the target is related to the frequency, which dictates the electrical size of the target, orientation, polarization, and constitutive parameters of the target [11], [14], [15]. The electrical size of an object relates to how big is the object physically compared to a wavelength of the incident wave and it dictates where in the scattering regime it falls in as it will be shown shortly. Constitutive parameters are the electric properties of the material, such as permeability and permittivity. A metallic target will scatter more energy while a dielectric target will generally scatter less energy due its lower reflection coefficient and to losses in the material that converts part of the incident microwave energy into heat. In the case of tornadic debris, vegetation is often lofted, so moisture content in the vegetation will also play a role in the amount of scattered energy. A freshly cut leaf will have more moisture than an old cut leaf that has dried up [7]. Man-made structures are made of diverse materials, from wood, to glass, to bricks, which all have different constitutive parameters that are also frequency dependent [16]. All of these factors have to be taken into account when calculating the scattering of random pieces of debris and it makes it an enormous challenge to calculate it quickly when needed. An important factor that makes calculating debris scattering more difficult than raindrop scattering is the fact that depending of the size of the object it will fall in a different scattering regime which will change the mechanisms behind the scattering. In the next section the scattering regimes will be explained.

## **2.3 Scattering Regimes**

It was previously mentioned that the RCS depends on the electrical size of the target, which itself depends on the wavelength of the transmitted wave. It would be convenient if the RCS of a target was directly proportional to the wavelength, but

that is not the case. There are three regimes that dictate the RCS of an object: The Rayleigh region (low-frequency region), the Mie region (Resonant region), and the Optical region (high-frequency region). To give a better picture of these regimes it is convenient to study the RCS of a Perfectly Electric Conductive (PEC) sphere as a function of the electrical size of the radius (ratio of radius to wavelength) since its RCS is independent of aspect angle.

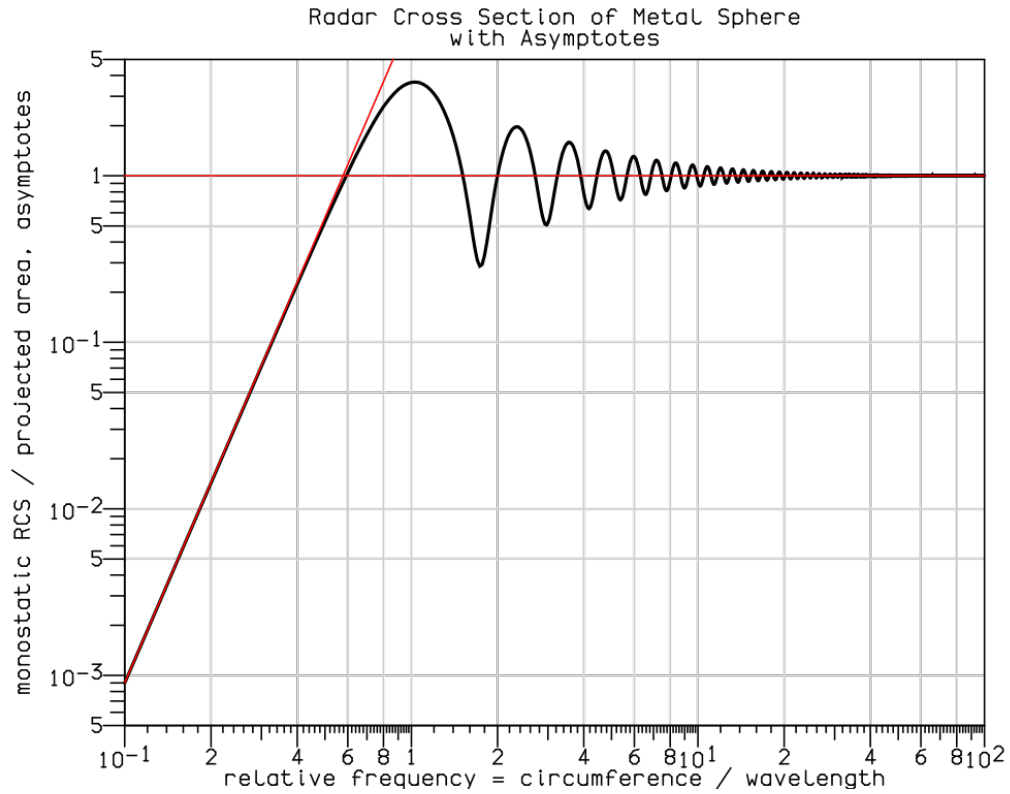


Figure 2.1: Normalized RCS of a sphere as a function of normalized circumference showing the different scattering regimes. Scatterers may fall in the Rayleigh regime (towards the left of the plot), Mie regime (towards the middle of the plot), or optical regime (towards the right of the plot) [17].

In the Rayleigh regime the wavelength of the incident field is larger than any dimension of the target ( $\lambda \gg L$ ). Because of this the phase variation that the target experiences is so small it's almost negligible. This induces charges on opposite sides of the target and creates a dipole moment. The strength of this dipole mo-

ment will depend on the orientation and size of the object since dipole moment is a function of charge and distance between charges [11], [12]. As seen in Figure 2.1, this means that as the size of the sphere grows the more it will scatter as it creates a stronger dipole moment. This goes on until the dimension of the object is comparable to the wavelength of the incident wave where it will transition to the Mie regime.

Rain drop scattering falls in the Rayleigh regime, greatly simplifying the analytical solution for its RCS. Rain drops are modeled as spheroids since drops are not perfectly spherical as they fall due to drag forces. The RCS of a drop is then the RCS of a spheroid[4]:

$$\sigma = 4\pi |\mathbf{s}(\hat{k}_s, \hat{k}_i)|^2 \quad (2.9)$$

which is directly related to the Rayleigh scattering by a spheroid [4]:

$$\mathbf{s}(\hat{k}_s, \hat{k}_i) = k^2 a^2 b \frac{\epsilon_r - 1}{3[1 + L(\epsilon_r - 1)]} \sin \chi \hat{e}_s \quad (2.10)$$

Where  $k$  is the wavenumber,  $a$  is the major axis length,  $b$  is the minor axis length,  $\epsilon_r$  is the dielectric constant of the spheroid,  $L$  is the shape factor,  $\chi$  is the angle between scattering direction and the incident wave polarization,  $\hat{e}_s$  is the scattered wave polarization, and  $\hat{k}_s$  and  $\hat{k}_i$  are the scattering and incident direction respectively. The tornado simulator computes the RCS of rain drops by using the above equations which are not computationally intensive.

The derivation of the RCS for a sphere is a well-known solution where the plane wave is transformed into spherical waves which involve Bessel and Hankel functions. For the Rayleigh scattering, the full scattering equation for a sphere can be simplified to come up with an easy formula. As the radius approaches zero, the

RCS can be reduced to [13]:

$$\sigma \approx \frac{9\lambda^2}{4\pi}(\beta a)^6. \quad (2.11)$$

In the Mie region the size of the object is comparable to the incident wavelength ( $\lambda \approx L$ ). In this case the phase of the incident wave changes considerably over the extent of the target and the simplicity of the dipole moment induced on the target is gone. Because of all these different charges induced on the body, the scattering is now dictated by surface wave effects and optical mechanisms whose interactions with each other will result in constructive/destructive interference making the RCS fluctuate as the object increases in size [11].

The equation for Mie scattering by a sphere is the full equation for the scattering of a sphere for all frequencies, but it is usually simplified for the Rayleigh and optical regime to make it easier to work with at those regimes. It has Hankel functions which are not easy to calculate analytically unless a computer is used [13].

$$\sigma = \frac{\lambda^2}{4\pi} \left| \sum_{n=1}^{\infty} \frac{(-1)^n(2n+1)}{\hat{H}_n^{(2)'}(\beta a) \hat{H}_n^{(2)}(\beta a)} \right|^2. \quad (2.12)$$

In the optical region, the target is a many times larger than the incident wavelength ( $\lambda \ll L$ ). At these high frequencies the small details in the target become important and the scattering target will be treated as a collection of independent scattering centers [11]. The overall RCS of the target will be an addition of the contribution from all the scattering centers [11]. The RCS is independent of physical size and it is only dictated by the orientation. In the case that the sphere is in the optical region, the RCS of the sphere as the radius approaches infinity reduces to [13]



$$\sigma \approx \pi a^2. \quad (2.13)$$

which is the physical area of the cross section of the sphere [13].

The scattering regimes were explored by using a sphere as a target, but it is also valid for any target. Hydrometeors fall in the Rayleigh regime with the WSR-88D frequency of 2.8 GHz keeping the scattering proportional to the hydrometeor's dimension. An exception to this are very large hailstones and tornadic debris. Tornadic debris may fall into any of the regimes which adds a degree of complexity to calculating its RCS especially for arbitrary shapes.

There are some simple shapes for who the RCS is well known and calculated mathematically, these are called canonical objects. Spheres, spheroids, plates, cylinders, wires, and ogives are part of these canonical shapes. For the purpose of this thesis we will focus on the RCS of spheres, plates, and cylinders which are the shapes that are used for the simulation of debris. The sphere is used as a calibration target for the anechoic chamber measurements, the cylinder is used as the stem of the simulated leaf, and the plate is used as the body of the simulated leaf and wooden targets. The cylinders and plates are also used as the targets for the multiple scattering experiment in a later chapter.

## 2.4 Plate Scattering

Plates are a simple but important shape as they can be used to model planar surfaces for scattering problems. Normally solving for the induced currents in a body involves using rigorous methods such as Method of Moments (MoM) or Finite Element Method (FEM) which are only feasible to do through computers due to their complexity. A method that is constantly used to calculate scattering from flat sur-

faces is the Physical Optics (PO) approximation. The PO method approximates the currents induced in the scattering body so that the scattered fields can be more easily calculated. It is most accurate when the body is smooth, electrically large, and at specular directions. This method only approximates currents on the illuminated surface and the current is zero in the shadow region.

$$\mathbf{J}_s \approx \begin{cases} 2\hat{\mathbf{n}} \times \mathbf{H} & \text{Illuminated} \\ 0 & \text{Shadow Region} \end{cases}. \quad (2.14)$$

The derivation for the PO scattering of a plate starts off with a plate placed in the  $y - z$  plane. By approximating the surface current on the scatterer, the scattered field is easily calculated using the vector potential integral equations for scattering [13]

$$\mathbf{A} = \frac{\mu}{4\pi} \iint_s \mathbf{J}_s \frac{e^{-j\beta R}}{R} ds' \approx \frac{\mu e^{-j\beta R}}{4\pi R} \mathbf{N}. \quad (2.15)$$

where

$$\mathbf{N} = \iint_s \mathbf{J}_s e^{-j\beta r' \cos \psi} ds'. \quad (2.16)$$

which for rectangular coordinates the integral is expressed as [13]

$$\mathbf{N} = \iint_s (\hat{\mathbf{x}}J_x + \hat{\mathbf{y}}J_y + \hat{\mathbf{z}}J_z) e^{-j\beta r' \cos \psi} ds'. \quad (2.17)$$

These rectangular form integrals are useful but do not express the scattering in terms of the polarizations  $\theta$  (H) and  $\phi$  (V); a rectangular to spherical transformation is used to express the result of the integrals in spherical coordinates. By using the rectangular to spherical coordinate transformation the rectangular coordinate

current components are transformed to their spherical counterparts

$$N_\theta = \iint_s (J_x \cos \theta \cos \phi + J_y \cos \theta \sin \phi - J_z \sin \theta) e^{-j\beta r' \cos \psi} ds'. \quad (2.18)$$

$$N_\phi = \iint_s (-J_x \sin \phi + J_y \cos \phi) e^{-j\beta r' \cos \psi} ds'. \quad (2.19)$$

To solve for the scattered fields, the PO approximation is implemented. Once the current is calculated the scattering integrals are used to solve for the far-field scattered fields using the equations

$$E_\theta^s \approx -\frac{j\beta e^{-j\beta r}}{4\pi r} \eta N_\theta = C \frac{e^{-j\beta r}}{r} \left\{ \cos \theta_s \sin \phi_s \left[ \frac{\sin(X)}{X} \right] \left[ \frac{\sin(Y)}{Y} \right] \right\}. \quad (2.20)$$

$$E_\phi^s \approx -\frac{j\beta e^{-j\beta r}}{4\pi r} \eta N_\phi = C \frac{e^{-j\beta r}}{r} \left\{ \cos \phi_s \left[ \frac{\sin(X)}{X} \right] \left[ \frac{\sin(Y)}{Y} \right] \right\}. \quad (2.21)$$

where

$$X = \frac{\beta a}{2} \sin \theta_s \cos \phi_s \quad (2.22)$$

$$Y = \frac{\beta b}{2} (\sin \theta_s \sin \phi_s - \sin \theta_i) \quad (2.23)$$

and

$$C = -j\eta \frac{ab\beta H_0}{2\pi} \quad (2.24)$$

The general equation for RCS (2.8) is used to compute the RCS of the plate, resulting in [13]

$$\sigma = 4\pi \frac{ab}{\lambda} (\cos^2 \theta_s \sin^2 \phi_s + \cos^2 \phi_s) \left[ \frac{\sin(X)}{X} \right]^2 \left[ \frac{\sin(Y)}{Y} \right]^2 \quad (2.25)$$

Notice that this RCS equation is used for both  $\theta$  and  $\phi$  polarizations so there is no discernible difference, but by using dielectric plates, as seen in chapter 3, this is corrected. These formulas are employed in the next chapter to calculate the RCS from the body of a leaf in MATLAB.

## 2.5 Cylinder Scattering

Scattering by a cylinder at normal incidence has been a scattering problem that has been solved long ago by Rayleigh [18]. For the purpose of this research, oblique incidence scattering by a cylinder is needed to compute its 3D RCS pattern. Several authors have solved this and proposed closed solutions [13], [19]. The formulas used by [19] are modal solutions that will be implemented in the next chapter to calculate the RCS of a thin cylinder. The RCS of a cylinder is derived by starting with a cylinder aligned with the  $z$  axis occupying the space  $\rho \leq a$  and an incident  $TM^z$  wave in cylindrical coordinates by using an addition theorem for Bessel functions [19]

$$E_z^i = E_0 \sin \theta \sum_{n=-\infty}^{\infty} j^n J_n(\lambda_2 \rho) F_n. \quad (2.26)$$

The scattered field by the cylinder is then

$$E_z^s = \sum_{n=-\infty}^{\infty} a_n^s H_n^{(2)}(\lambda_2 \rho) F_n. \quad (2.27)$$

The internal field in the cylinder is

$$E_z = \sum_{n=-\infty}^{\infty} a_n J_n(\lambda_1 \rho) F_n. \quad (2.28)$$

The components of the magnetic field are also expressed by the Bessel function addition theorem

$$H_z^i = 0. \quad (2.29)$$

$$H_z^s = \sum_{n=-\infty}^{\infty} b_n^s H_n^{(2)}(\lambda_2 \rho) F_n. \quad (2.30)$$

$$H_z = \sum_{n=-\infty}^{\infty} b_n J_n(\lambda_1 \rho) F_n. \quad (2.31)$$

The variables  $a_n^s$  and  $b_n^s$  are the magnitude coefficients of the TM and TE modes respectively [19] and need to be found in order to solve for the scattering of the cylinder. The coefficients are solved by matching the fields on the inside and outside of the cylinder by using boundary conditions [19]. For this the  $\phi$  component of the fields are obtained from Maxwell's equations [19]

$$E_\phi^i = \sum_{n=-\infty}^{\infty} -\frac{hnE_0 \sin \theta j^n J_n(\lambda_2 \rho) F_n}{\rho \lambda_2^2}. \quad (2.32)$$

$$E_\phi^s = \sum_{n=-\infty}^{\infty} \left[ -\frac{hna_n^s}{\rho \lambda_2^2} H_n^{(2)}(\lambda_2 \rho) + \frac{j\mu_2 \omega b_n^s}{\lambda_2} H_n^{(2)'}(\lambda_2 \rho) \right] F_n. \quad (2.33)$$

$$E_\phi = \sum_{n=-\infty}^{\infty} \left[ -\frac{hna_n}{\rho \lambda_1^2} J_n(\lambda_1 \rho) + \frac{j\mu_1 \omega b_n}{\lambda_1} J_n'(\lambda_1 \rho) \right] F_n. \quad (2.34)$$

$$H_\phi^i = \sum_{n=-\infty}^{\infty} -\frac{j\beta_2^2 E_0 \sin \theta j^n J_n'(\lambda_2 \rho) F_n}{\mu_2 \omega \lambda_2}. \quad (2.35)$$

$$H_\phi^s = \sum_{n=-\infty}^{\infty} \left[ -\frac{h n b_n^s}{\rho \lambda_2^2} H_n^{(2)}(\lambda_2 \rho) - \frac{j\beta_2^2 a_n^s}{\mu_2 \omega \lambda_2} H_n^{(2)'}(\lambda_2 \rho) \right] F_n. \quad (2.36)$$

$$H_\phi = \sum_{n=-\infty}^{\infty} \left[ -\frac{h n b_n}{\rho \lambda_1^2} J_n(\lambda_1 \rho) - \frac{j\beta_1^2 a_n}{\mu_1 \omega \lambda_1} J_n'(\lambda_1 \rho) \right] F_n. \quad (2.37)$$

where  $h = \beta_2 \cos \theta$  and the  $(.)'$  on the Bessel and Hankel functions means a derivative [19]. The boundary conditions are written [19]

$$\begin{cases} E_\phi^i + E_\phi^s = E_\phi & \text{at } \rho = a \\ H_z^i + H_z^s = H_z \end{cases}. \quad (2.38)$$

$$\begin{cases} E_z^i + E_z^s = E_z & \text{at } \rho = a \\ H_\phi^i + H_\phi^s = H_\phi \end{cases}. \quad (2.39)$$

These equations are solved to give [19]

$$a_n^s = E_0 \sin \theta j^n \left[ -\frac{J_n(v)}{H_n^{(2)'}(v)} - \frac{2j \left( \frac{H_n^{(2)'}(v)}{v H_n^{(2)}(v)} - \frac{K J_n'(u)}{u J_n(u)} \right)}{\pi v^2 [H_n^{(2)}(v)]^2 D} \right]. \quad (2.40)$$

$$b_n^s = \frac{\beta_2}{\epsilon_2 \omega} E_0 \sin \theta j^n \left[ \frac{2}{\pi v^2} \left( \frac{1}{v^2} - \frac{1}{u^2} \right) \frac{n \cos \theta}{H_n^{(2)}(v) D} \right]. \quad (2.41)$$

$$D = \left( \frac{H_n^{(2)'}(v)}{v H_n^{(2)}(v)} - \frac{K J_n'(u)}{u J_n(u)} \right) \left( \frac{H_n^{(2)'}(v)}{v H_n^{(2)}(v)} - \frac{N^2 J_n'(u)}{K u J_n(u)} \right) - \left( \frac{1}{v^2} - \frac{1}{u^2} \right)^2 n^2 \cos^2 \theta. \quad (2.42)$$

$$K = \frac{\epsilon_1}{\epsilon_2}. \quad (2.43)$$

$$N^2 = \frac{\beta_1^2}{\beta_2^2} = \frac{\epsilon_1 \mu_1}{\epsilon_2 \mu_2}. \quad (2.44)$$

$$u = \lambda_1 a = (\beta_1^2 - \beta_2^2 \cos^2 \theta)^{1/2} a. \quad (2.45)$$

$$v = \lambda_2 a = \beta_2 \sin \theta a. \quad (2.46)$$

The scattering coefficients  $a_n^s$  and  $b_n^s$  are of utmost importance as it will dictate the scattering by a dielectric cylinder. Using the equations derived by [13] for the RCS of a conducting cylinder by an oblique incidence plane wave, the scattering coefficients are plugged in and the RCS for a dielectric cylinder by an oblique incidence plane wave is obtained.

$$\sigma_{HH} \approx \frac{4l^2}{\pi} \frac{\sin^2 \theta_s}{\sin \theta_i} \left| \sum_{n=0}^{\infty} \epsilon_n a_n \cos(n\phi) \right|^2 \left\{ \frac{\sin[\frac{\beta l}{2}(\cos \theta_i + \cos \theta_s)]}{\frac{\beta l}{2}(\cos \theta_i + \cos \theta_s)} \right\}^2. \quad (2.47)$$

$$\sigma_{VV} \approx \frac{4l^2}{\pi} \frac{\sin^2 \theta_s}{\sin \theta_i} \left| \sum_{n=0}^{\infty} \epsilon_n b_n \cos(n\phi) \right|^2 \left\{ \frac{\sin[\frac{\beta l}{2}(\cos \theta_i + \cos \theta_s)]}{\frac{\beta l}{2}(\cos \theta_i + \cos \theta_s)} \right\}^2. \quad (2.48)$$

These scattering equations are used in the next chapter to simulate the stem of a leaf in MATLAB.

## 2.6 Conclusion

The theory behind the scattering regimes and its impacts on the RCS of objects has been explored. Hydrometeors fall in the Rayleigh regime making it easier to compute their RCS. Debris may fall anywhere in the scattering regime making it harder to simulate quickly without taking .

Analytical methods for the scattering of simple shapes are possible by using the PO approximation on flat surfaces and modal analysis on cylinders. Additionally, the scattering for a plate and a dielectric cylinder was presented and are used together in the next chapter to obtain the RCS of a leaf. And in general, the closed solutions for the RCS of canonical objects can lead to more complex scatterers if superposition is used to combine the RCS of several canonical objects.



## **Chapter 3**

### **Radar Cross Section Simulations**

#### **3.1 Introduction**

In recent years, the calculation of the RCS of complex objects has been faster to obtain thanks to the advance in computational power. It has opened the path for the development of electromagnetic solvers to simulate a wide variety of electromagnetic structures such as antennas and scattering targets.

An electromagnetic solver created by ANSYS, HFSS, uses FEM while FEKO uses MoM and can also use PO and other schemes to solve for the scattered fields. While not being an electromagnetic solver, MATLAB is a computational mathematics program that is used to solve scientific and engineering problems. It can be used to find the RCS of objects using the PO approximation due to its low complexity and easy implementation. These software packages were used to simulate the RCS of the desired target and compare the results with each other to make sure there is consistency between the results. To further confirm that the simulation's results are accurate, RCS measurements of the simulated targets are taken in an anechoic chamber and then compared to the simulated results which will be shown in the following chapter.

Because the dual polarization nature of weather radars, all simulations for all

platforms will record the Horizontal polarization (HH), also called  $\theta$  polarization, and Vertical polarization (VV), also called  $\phi$  polarization. Cross polarization, HV/VH is recorded too. Since The following sections will show HH, VV, and HV RCS pattern results from MATLAB, FEKO, and HFSS for the simulated debris.

### 3.2 Analytical Method in MATLAB

In MATLAB, a leaf is simulated to be used as a debris type in the tornado simulator. To keep the math simple and make the simulation faster the PO approximation is used. Like stated in the previous chapter, when using PO the result is most accurate at specular directions and it becomes less accurate as we move away from the specular direction, but overall it still remains a good approximation. The leaf was simulated using a resistive sheet as a plate for the body of the leaf and a dielectric thin cylinder for the stem. The RCS of the sheet and cylinder are calculated by MATLAB functions separately. Once the RCS of both objects are computed, their complex RCS are added together to obtain the total RCS of the simulated leaf.

To standardize the rotation and orientation of the leaf between the electromagnetic area of this research and the aerodynamic part of the research, a coordinate system and rotation scheme is defined for it. It is defined as an orthogonal local coordinate system with unit vectors  $x - y - z$  where the object's longest dimension is directed along the  $y$  axis and the object's face is normal to the  $z$  axis.

The rotation is done using Euler rotation through three rotation angles,  $\alpha$ ,  $\beta$ , and  $\gamma$ . These three angles can represent the object in any orientation possible in 3D space and will rotate the coordinate system according to the right hand rule. The  $\alpha$  angle rotates the coordinate system around the  $z$  vector and transforms the coordinate system into  $x' - y' - z'$ . A  $\beta$  angle rotation will rotate the  $x' - y' - z'$

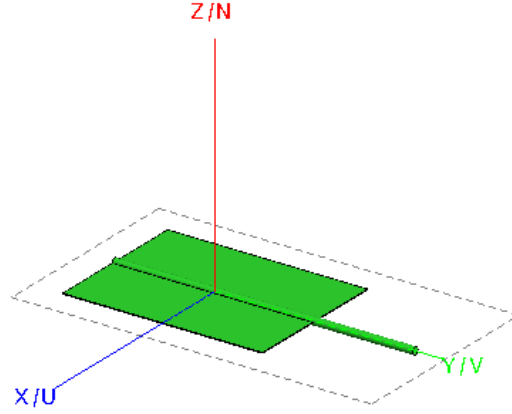


Figure 3.1: Orientation of the simulated leaf in global coordinates. For all simulations, the leaf and other simulated debris have their longest dimension along the  $y$  axis while their face is normal to the  $z$  axis.

coordinates around the  $y'$  vector and a  $x'' - y'' - z''$  coordinate system is obtained. And finally, a rotation of  $\gamma$  angle will rotate around the  $z''$  ending with the final coordinate system  $x''' - y''' - z'''$ . Figure 3.2 shows a clear picture of the Euler rotations used for the coordinate system and the end result.

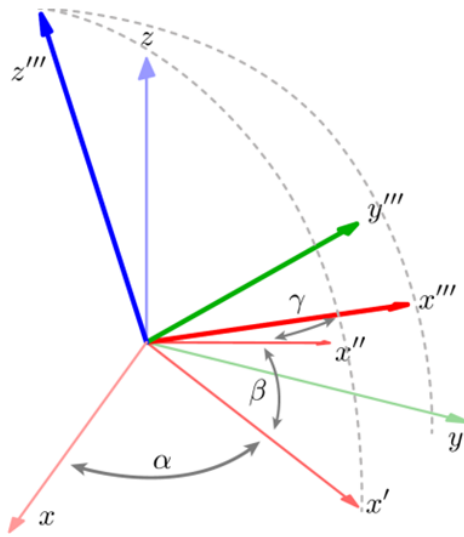


Figure 3.2: Coordinate system rotation using Euler rotation. The angles  $\alpha$ ,  $\beta$ , and  $\gamma$  control the rotation to achieve any orientation in 3D space. Angle  $\alpha$  rotates the coordinate system around the  $z$  axis. Next, the  $\beta$  angle rotates the coordinate system around the  $y'$  axis. And finally, the  $\gamma$  angle rotates the coordinate system around the  $z''$  axis to finally obtain a  $x''' - y''' - z'''$  coordinate system [6].

The transformation is done through a transformation matrix

$$T = \begin{bmatrix} \cos \alpha \cos \beta \cos \gamma - \sin \alpha \sin \gamma & \cos \alpha \cos \beta \sin \gamma + \sin \alpha \cos \gamma & -\cos \alpha \sin \beta \\ -\sin \alpha \cos \beta \cos \gamma - \sin \alpha \sin \gamma & -\sin \alpha \cos \beta \sin \gamma + \sin \alpha \cos \gamma & \sin \alpha \sin \beta \\ \sin \beta \cos \gamma & \sin \beta \sin \gamma & \cos \beta \end{bmatrix} \quad (3.1)$$

which is done by multiplying the transformation matrices of each individual rotation in order

$$T_\alpha = \begin{bmatrix} \cos \alpha & \sin \alpha & 0 \\ -\sin \alpha & \cos \alpha & 0 \\ 0 & 0 & 1 \end{bmatrix} \quad (3.2)$$

$$T_\beta = \begin{bmatrix} \cos \beta & 0 & -\sin \beta \\ 0 & 1 & 0 \\ \sin \beta & 0 & \cos \beta \end{bmatrix} \quad (3.3)$$

$$T_\gamma = \begin{bmatrix} \cos \gamma & \sin \gamma & 0 \\ -\sin \gamma & \cos \gamma & 0 \\ 0 & 0 & 1 \end{bmatrix} \quad (3.4)$$

where  $T_\alpha$  is the transformation matrix for the  $\alpha$  angle rotation,  $T_\beta$  is the transformation matrix for the  $\beta$  angle rotation, and  $T_\gamma$  is the transformation matrix for the  $\gamma$  angle rotation.

All the following simulations in all platforms are done at 2.8 GHz which is the WSR-88D's operating frequency. The leaf is 6 cm wide, 8 cm long, and 0.5 mm thick while the stem is 12 cm long and has a radius of 1.5 mm. The dielectric properties for the leaf were extracted from [7]. By using the gravimetric moisture of the leaf, the dielectric constant and tangent loss can be calculated. It is important to

	Leaf	Sylvester Pine
Dielectric Constant	34.558	2.314
Tangent Loss	0.357	0.247

Table 3.1: Dielectric properties for the scatterers to be modeled. The leaf's dielectric properties were obtained at 80% gravimetric moisture content at 25°C while the wood dielectric constants were for 13% gravimetric moisture content at 25°C.

get the correct dielectric properties for the debris as this is an important parameter that determines the scattering of a dielectric body. The formulas for the dielectric properties of a leaf are [7]:

$$\epsilon' = 3.95 \exp 2.79Mg - 2.25. \quad (3.5)$$

$$\epsilon'' = 2.69 \exp 2.15Mg - 2.68. \quad (3.6)$$

where  $Mg$  is the gravimetric moisture. Fresh leaves are assumed to be swept into a tornado so a gravimetric moisture content of 0.8 (80%) is used. This result in the leaf having dielectric constant and tangent loss of 34.558 and 0.357 respectively and will be used for all simulations of the leaf on all platforms.

The scattering for a resistive sheet provided by [7] will be used for the simulations. The scattering by a resistive sheet will depend on its reflection coefficients which are determined by [7]

$$\Gamma_E = (1 + \frac{2R}{Z} \cos \theta_0)^{-1}. \quad (3.7)$$

$$\Gamma_H = (1 + \frac{2R}{Z} \sec \theta_0)^{-1}. \quad (3.8)$$

$$Z = 377. \quad (3.9)$$

$$R = \frac{jZ}{\kappa\tau(\epsilon - 1)}. \quad (3.10)$$

$$\tau = 0.032Mg^2 + 0.091Mg + 0.075. \quad (3.11)$$

where  $Z$  is the intrinsic impedance of free space,  $R$  is the resistivity of the dielectric sheet,  $\kappa$  is the wavenumber, and  $\tau$  is the thickness of the sheet in millimeters.

Using the PO approximation and the reflection coefficients (3.7), (3.8), the scattering by a leaf is [7]:

$$\sigma_E = 4\pi \left| \frac{ab}{\lambda} \cos \theta_0 \Gamma_E \frac{\sin X}{X} \right|^2. \quad (3.12)$$

$$\sigma_H = 4\pi \left| \frac{ab}{\lambda} \cos \theta_0 \Gamma_H \frac{\sin X}{X} \right|^2. \quad (3.13)$$

where

$$X = \frac{ka}{2}(\sin \theta + \sin \theta_0). \quad (3.14)$$

where  $a$  and  $b$  are the width and length of the leaf respectively. Note that equations (3.12) and (3.13) are very similar to the RCS of a PEC plate given in (2.25) except for the fact that for the RCS of a dielectric plate, a reflection coefficient is added to account for its dielectric properties. By adding the scattering of the resistive sheet and the dielectric cylinder the total RCS for the simulated leaf is obtained. The resulting RCS patterns are shown in the next following figures.

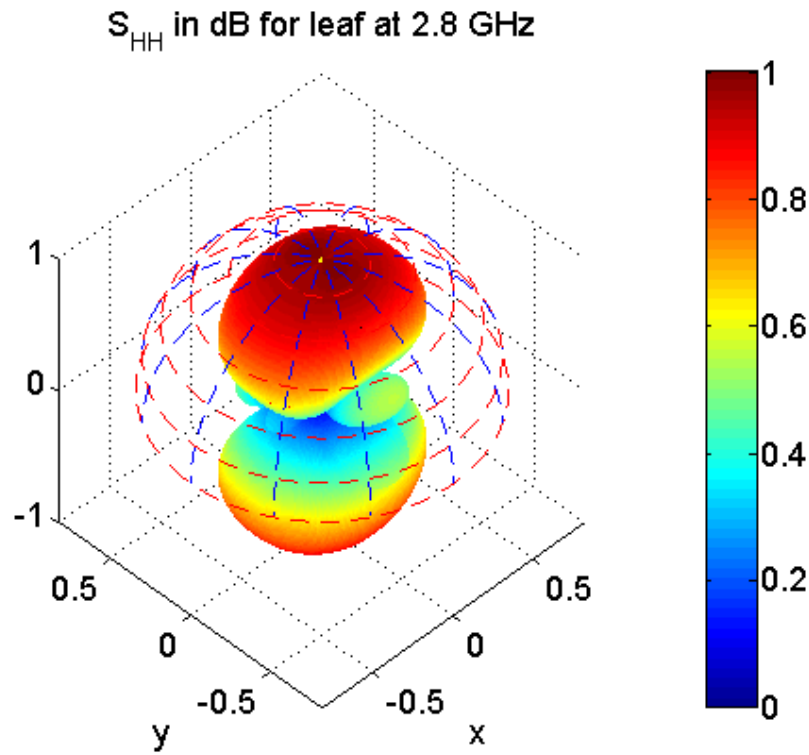


Figure 3.3: RCS pattern of simulated leaf for HH-pol. Notice the contribution from the cylinder's end-caps, creating small lobes along the  $y$  axis. The polarization is perpendicular to the cylinder and the side of the sheet, creating low scattering along the  $y - z$  plane.



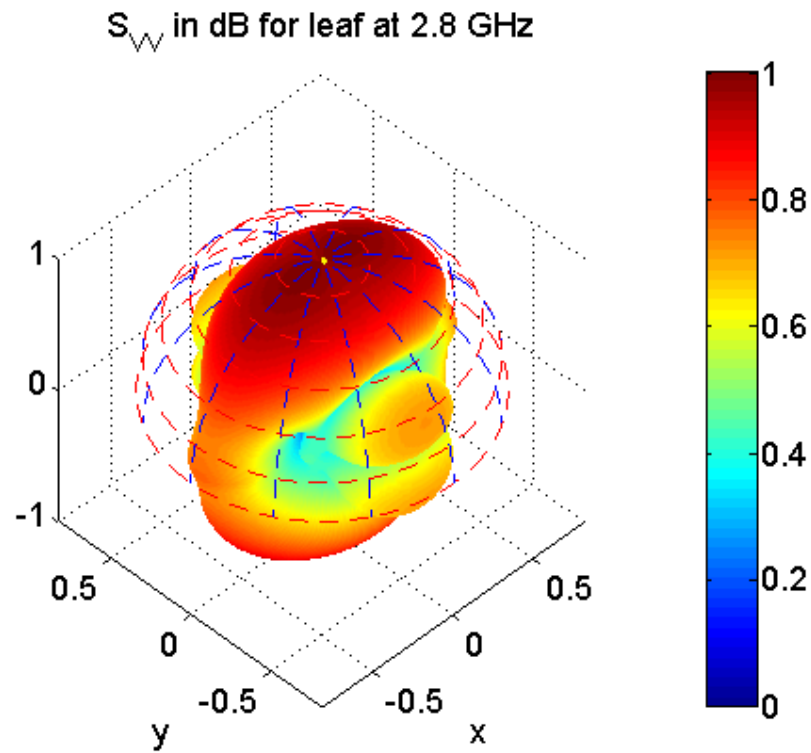


Figure 3.4: RCS pattern of simulated leaf for VV-pol. Contribution from the cylinder's end-caps can be seen again with the additional contribution along the  $y - z$  plane from the leaf's side and cylinder due to the polarization being parallel to the leaf side.

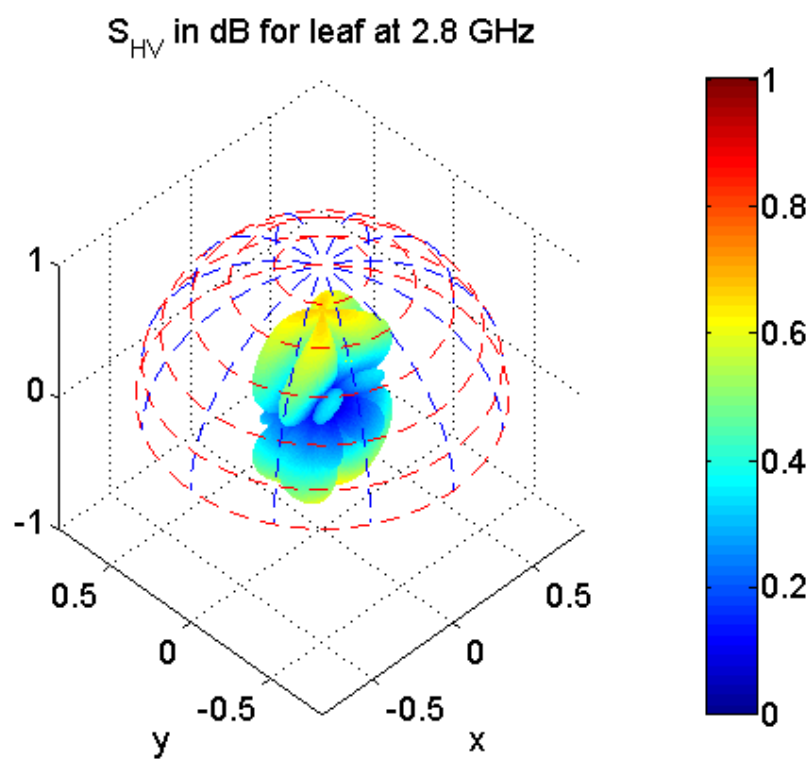


Figure 3.5: RCS pattern of simulated leaf for HV-pol. Some cross polarization contribution can be seen here. As expected, cross polarization is larger a broadside.

The results from the MATLAB simulations can be very intuitive if looked at closely. The cylinder runs along the  $y$  axis and a couple of small lobes can be seen at the  $y$  axis, indicating scattering due to the end-caps of the cylinder. As small as the cylinder is, this shows that it still contributes to the overall RCS of the leaf. The sheet may be thin but it has a larger contribution depending on the polarization of the incident wave. For Figure 3.3 the polarization is perpendicular to the side of the sheet, creating a very low RCS signature. On the other hand, in Figure 3.4, the polarization is parallel to the side of the leaf and the cylinder producing a noticeable contribution to the total RCS even if that dimension is very small compared to the rest of the structure.

The PO approximation on PEC plates creates the same RCS pattern for both HH and VV polarizations which would not be helpful for our case. Because the plates have to be dielectric for the leaf, polarizations HH and VV are now discernible and will produce the polarizations of interest, even cross polarization patterns HV as seen in Figure 3.5. This means that the use of analytical models to create RCS patterns quickly and effectively is achievable and can be used to create the RCS library for the tornado simulator. It is, however, beneficial to compare the MATLAB results with the electromagnetic solvers available to see how the analytical model fares to full wave solvers.

### 3.3 FEKO Simulations

The second software package used for simulations was FEKO because of its easy implementation. The setup is simple as only the target has to be drawn and no additional structures, such as an Absorbing Boundary Condition (ABC), are needed. By drawing a cuboid with the leaf's dimension we obtain the leaf's body. Drawing

a cylinder with the appropriate dimensions give us the stem. Once the two objects are drawn they are joined to make a single object. FEKO offers a wide library of dielectric media but not the one we require for the leaf so the previously derived constants are imported manually. A plane wave excitation is requested and is swept from  $\theta \in [0^\circ, 180^\circ]$  while  $\phi$  is swept from  $\phi \in [-180^\circ, 180^\circ]$  to obtain measurements over spherical angles. To make the simulations faster and to reduce computational costs the angle step for both phi and theta angles is 2 degrees giving us a total of 16471 observation points. The solution scheme here is selected to be PO to directly compare with the MATLAB results. Because FEKO uses a hybrid MoM/PO solving technique, the object still has to be meshed as it is needed for MoM solutions. A standard meshing is selected which means the object is segmented in triangles that are  $\lambda/10$  or larger for standard meshing settings [20]. Once the meshing is done the setup is complete and the simulation is run. The results of the simulation are plotted in 3D polar plots.

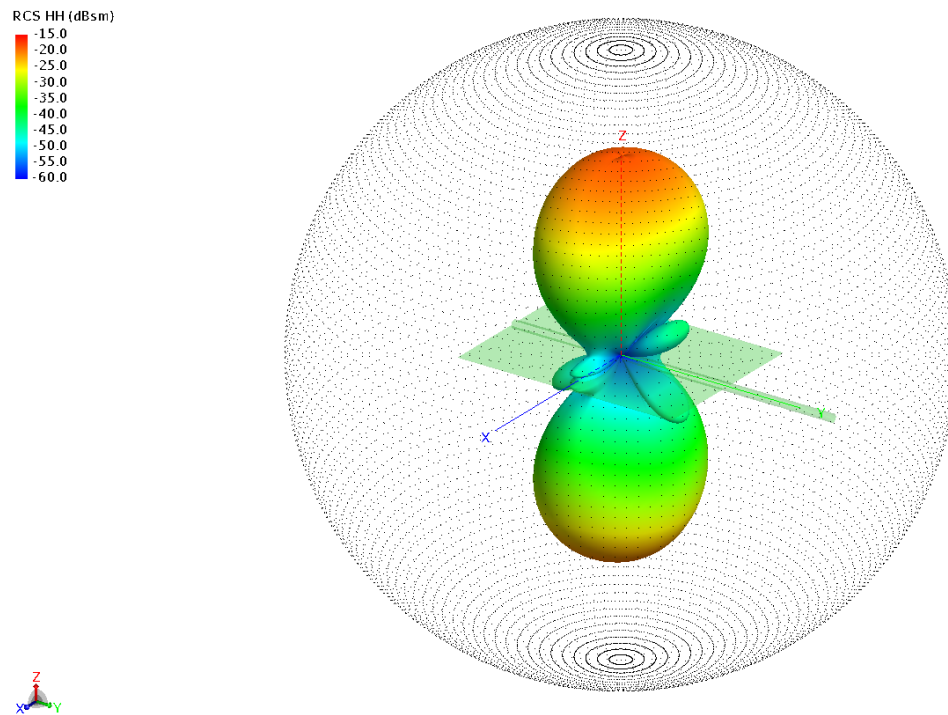


Figure 3.6: RCS pattern of FEKO simulated leaf for HH-pol. The contributions from the end-caps of the cylinder can be seen here just as seen in the MATLAB simulations.

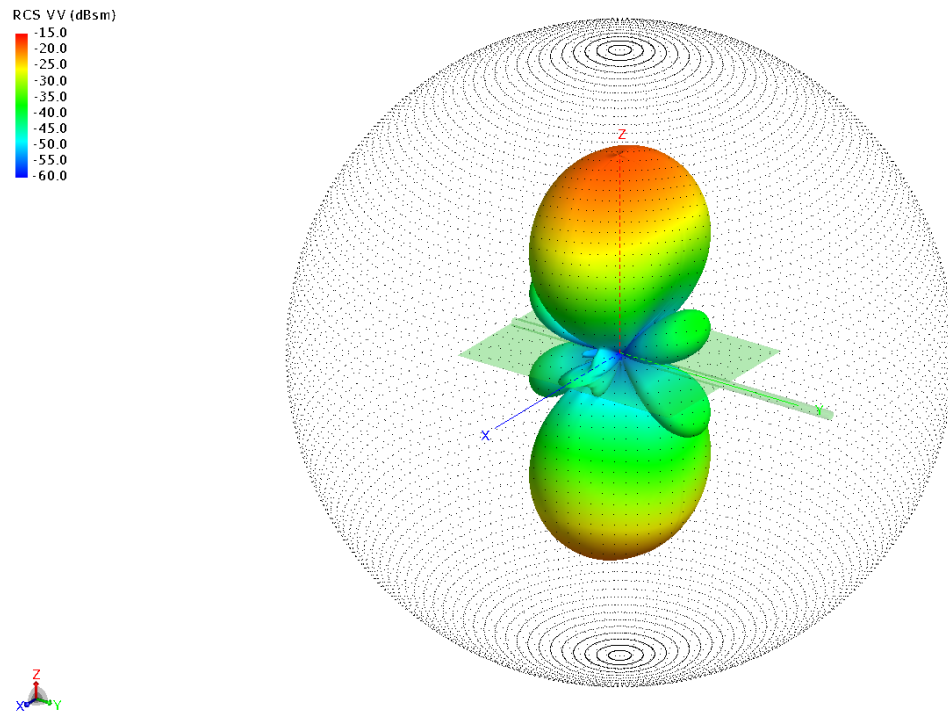


Figure 3.7: RCS pattern of FEKO simulated leaf for VV-pol. The cylinder's end-cap contribution can be seen here as well. But notice that the cylinder's and leaf's side contribution is not seen here around the  $y - z$  plane as seen in the MATLAB simulation.

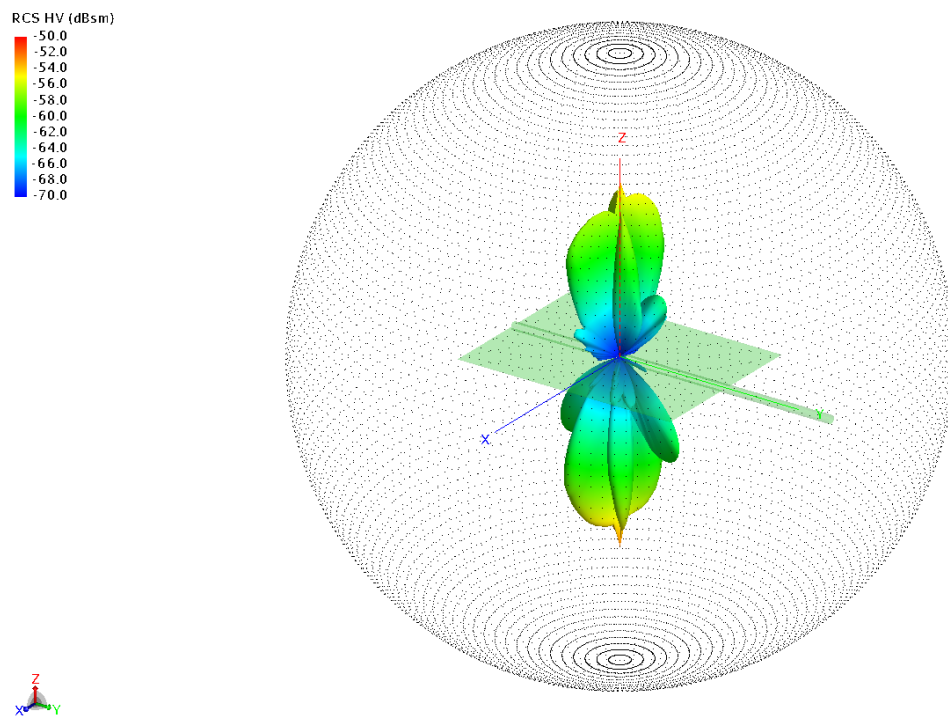


Figure 3.8: RCS pattern of FEKO simulated leaf for HV-pol. A small cross polarization contribution is shown.

In Figure 3.6, the RCS pattern of the leaf using HH polarization can be seen. As with the MATLAB simulations, the contribution from the cylinder's endcaps can be seen as the small lobes along the  $y$  axis, indicating that this small cylinder has an impact on the overall RCS pattern. The pattern for VV polarization is similar to MATLAB, but as seen in Figure 3.7, the contribution from the cylinder's and sheet's side is not present, meaning that FEKO was not able to capture this effect. As for the cross polarization pattern HV, as seen in Figure 3.8, is still present and very similar to the result from MATLAB.

To compare the accuracy of the MATLAB simulations, they are plotted with the FEKO simulations for comparison. The results agree very well except for a small offset in magnitude. This may be due to the fact that the dielectric properties taken from [7] are actually for measurements at 10 GHz. There is high confidence that if dielectric properties for a leaf at 2.8 GHz are found it would match the FEKO simulations very well.



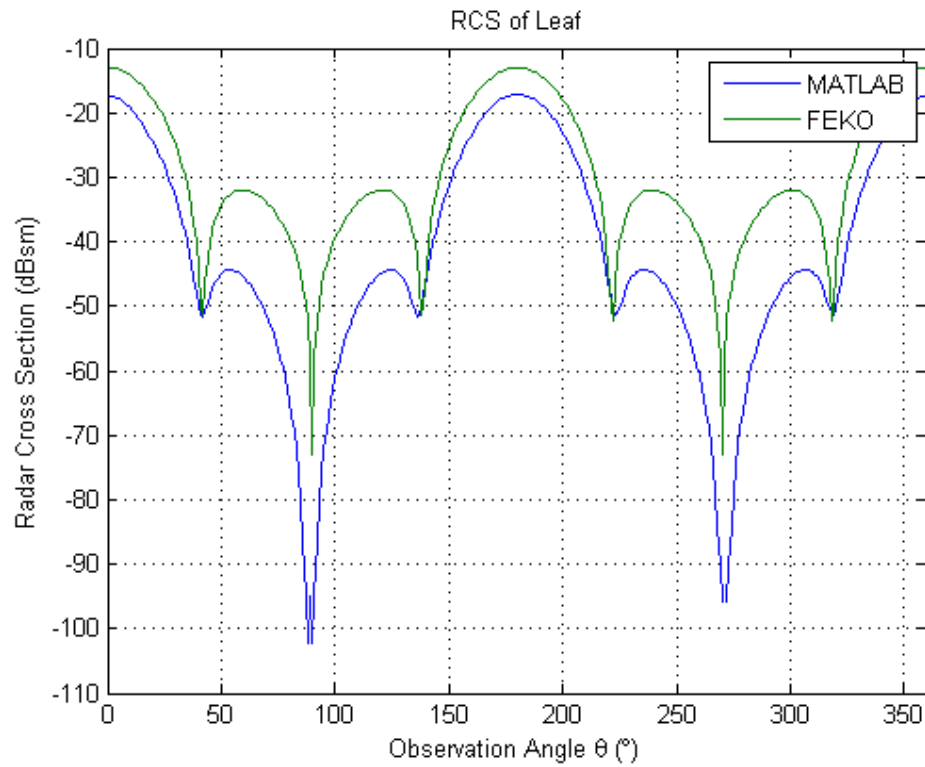


Figure 3.9: RCS pattern of FEKO and MATLAB simulated leaf for HH-pol. The RCS pattern shapes agree between MATLAB and FEKO but the magnitude of the pattern is lower for MATLAB.

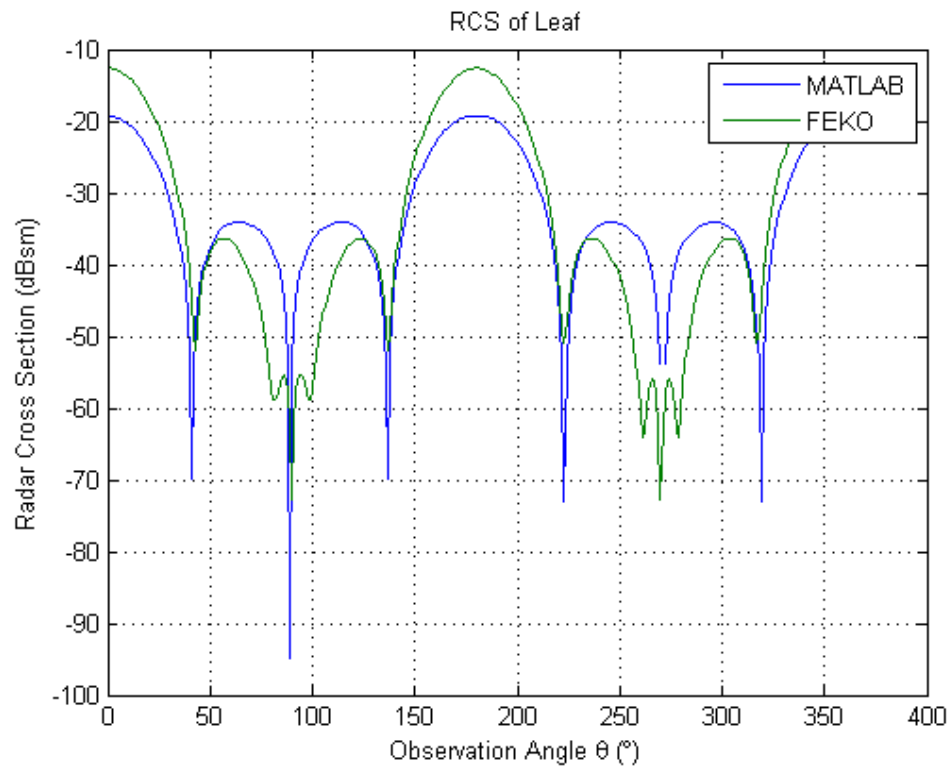


Figure 3.10: RCS pattern of FEKO and MATLAB simulated leaf for VV-pol. Similar to the previous figure, the pattern shapes between FEKO and MATLAB agree but MATLAB produces a lower magnitude pattern.

Another common type of debris that comes from man-made structures are wooden boards from buildings such as houses. Three wooden boards of different size are simulated as well as a large wooden sheet. The wooden objects simulated were modeled to be like wooden boards that were available at the lab which were determined, through trial and error, to be made of Sylvester pine. The dielectric properties of the wooden objects were determined by [21] where the dielectric constant is 2.314 and the tangent loss is 0.247. The measurements of the dielectric properties from [21] are for a gravimetric moisture content of 13% and at a temperature of 25°C which is dry wood and considered acceptable for our simulations. The dimensions of the wooden targets are shown in Table 3.2. By using the same setup as the one used for the leaf, the 3D RCS pattern is obtained for the wooden boards and wooden sheet.

	Length	Width	Thickness
Wood Board 1	0.2794	0.1397	0.01587
Wood Board 2	0.3683	0.0889	0.0381
Wood Board 3	0.3937	0.1397	0.0381
Wood Sheet	0.4572	0.4572	0.009525

Table 3.2: Dimensions for the wooden targets to be simulated and measured in meters.

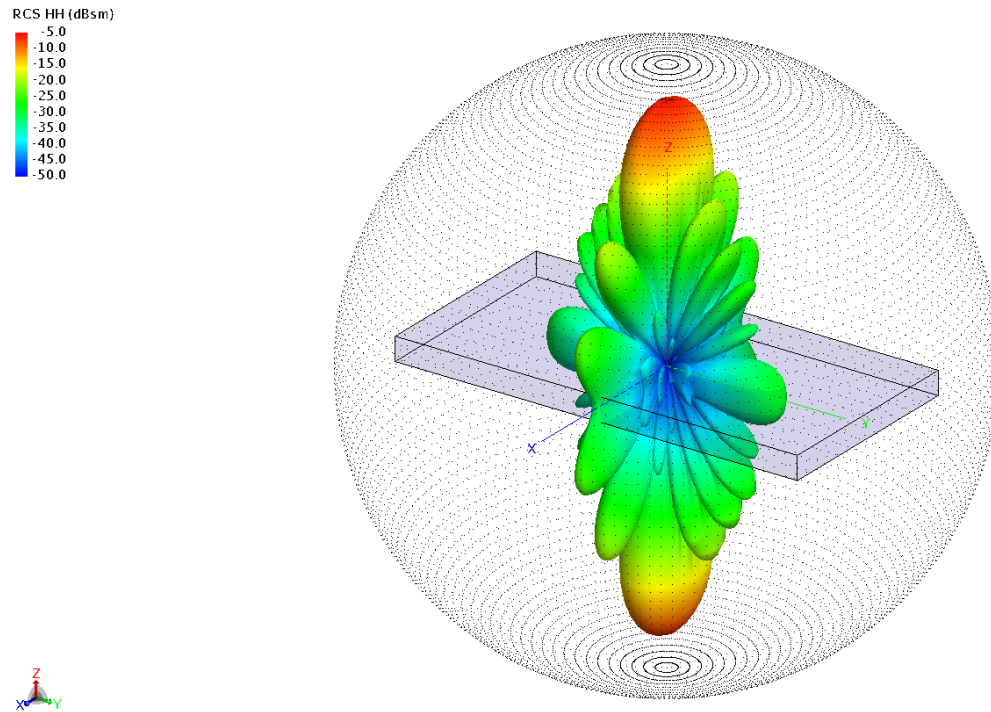


Figure 3.11: RCS pattern of FEKO simulated wood board 1 for HH-pol. A large peak is centered at broadside and it is stretched in the  $x$  axis due to the difference in the ratio of dimensions along the length and width of the board.

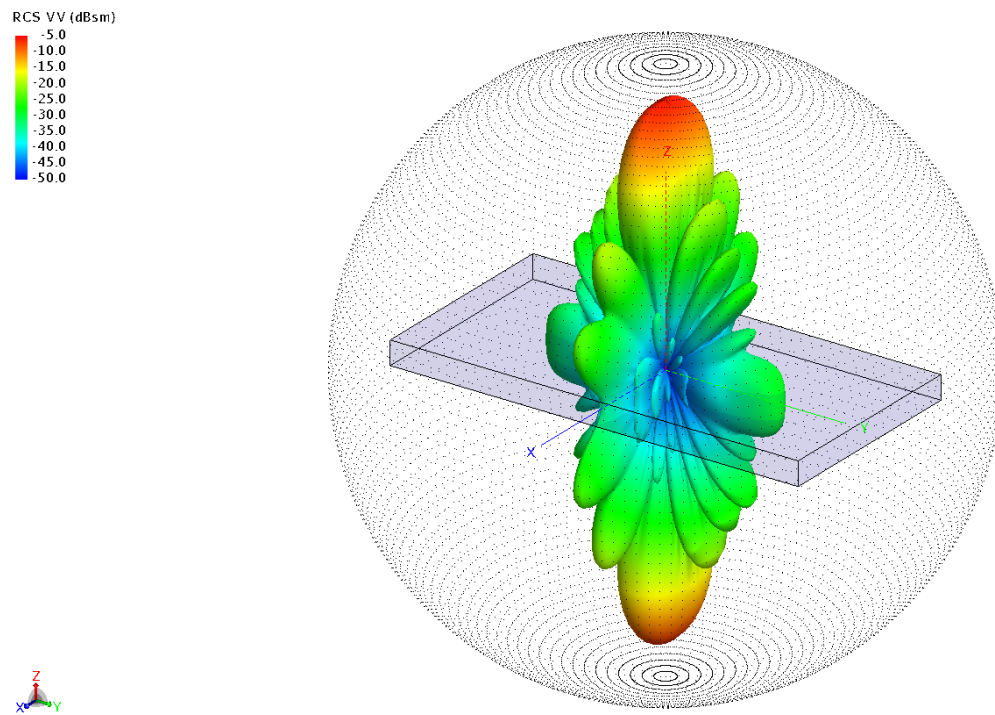


Figure 3.12: RCS pattern of FEKO simulated wood board 1 for VV-pol. The RCS pattern is similar to that of the HH polarization.

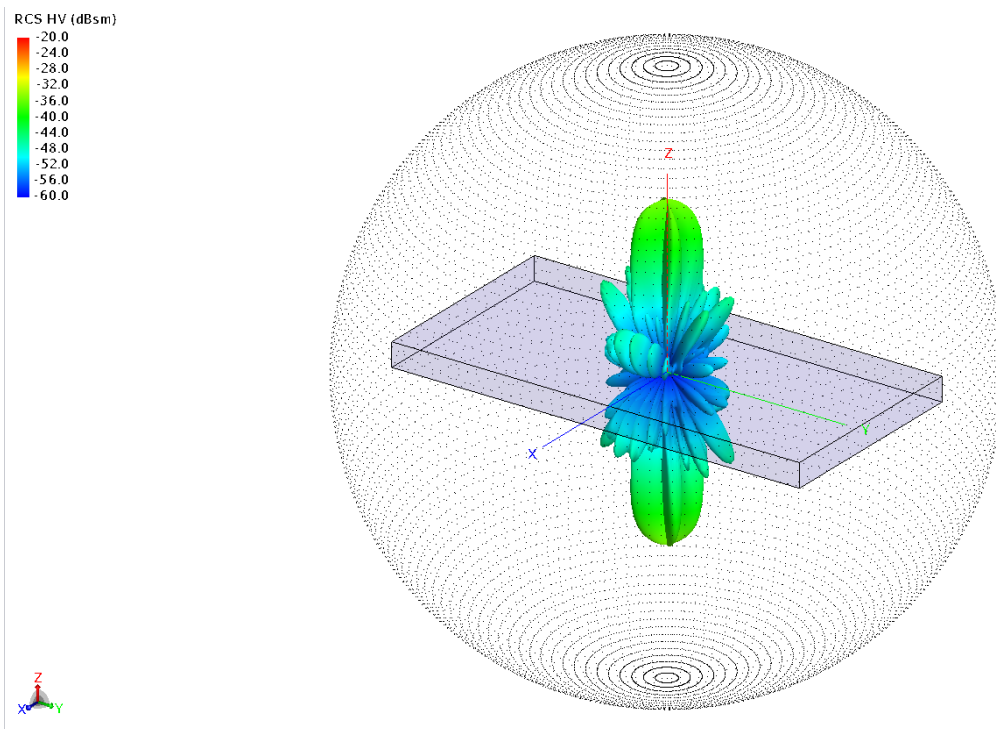


Figure 3.13: RCS pattern of FEKO simulated wood board 1 for HV-pol. A small cross polarization contribution can be seen.

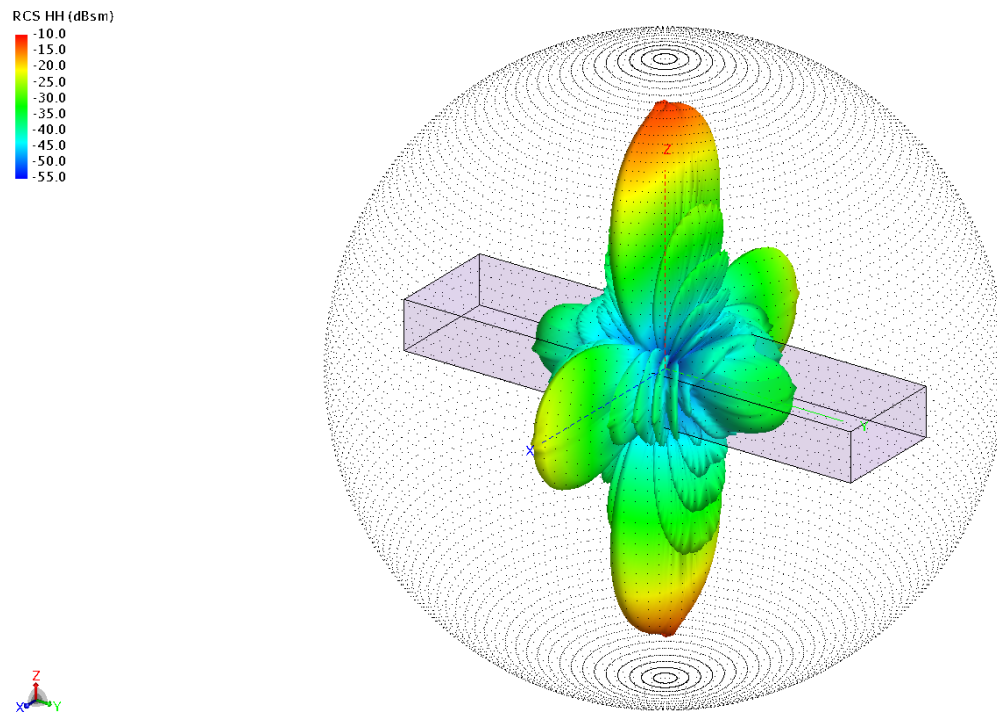


Figure 3.14: RCS pattern of FEKO simulated wood board 2 for HH-pol. This wooden board is thicker and shorter, creating an even more elongated RCS peak at broadside along the  $x$  axis.

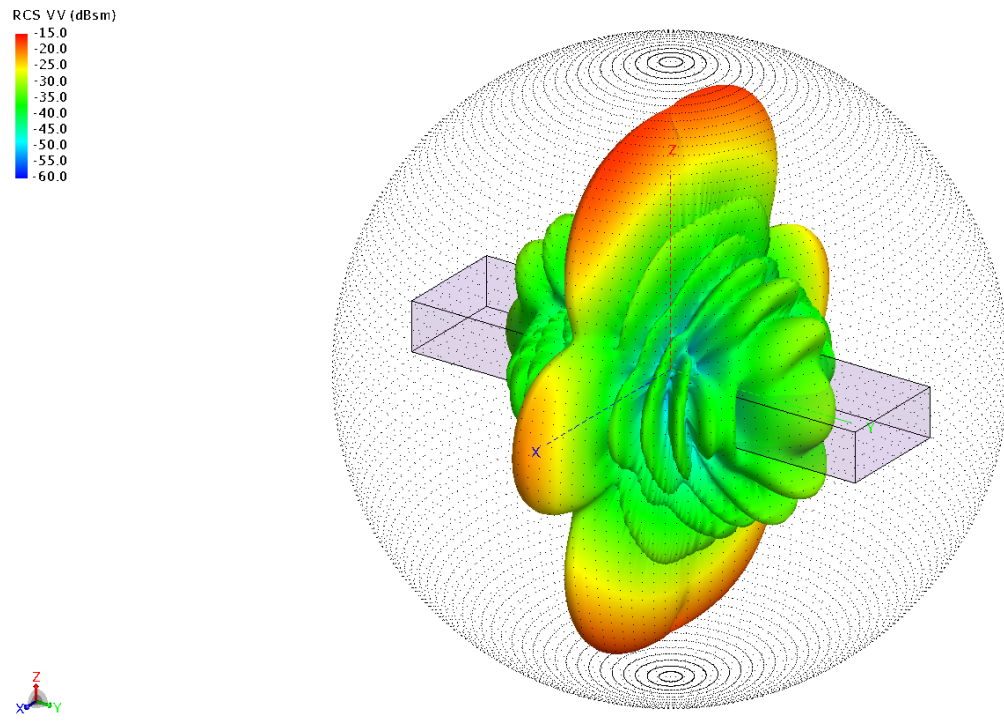


Figure 3.15: RCS pattern of FEKO simulated wood board 2 for VV-pol. Now that the polarization is parallel to the largest dimension of the target, the RCS pattern near broadside becomes even more elongated and the RCS levels on the sides are higher.



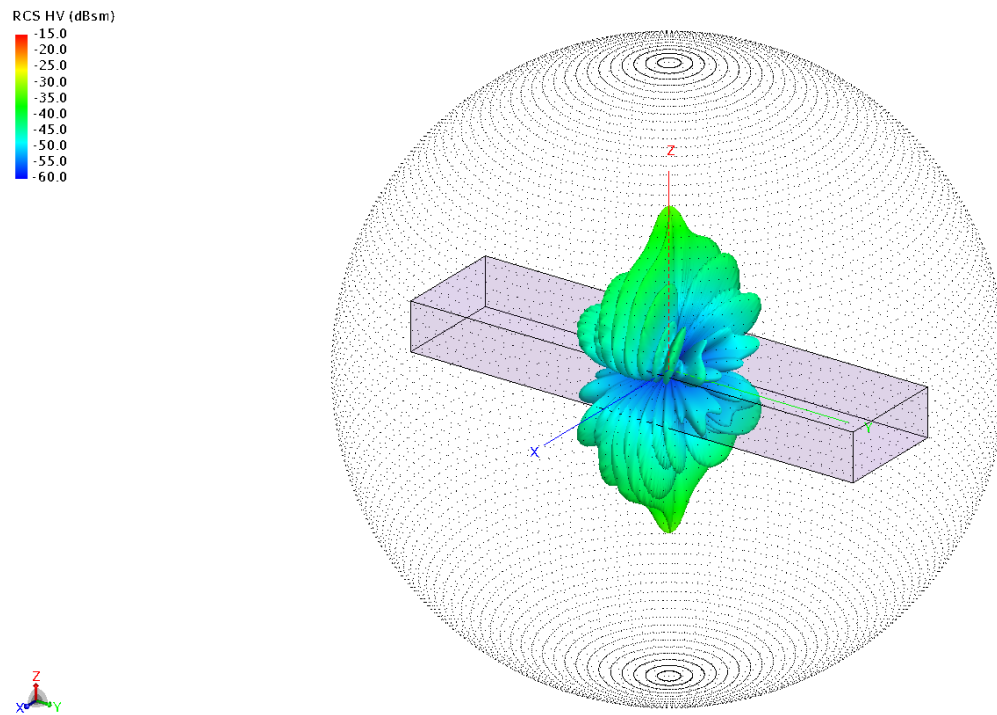


Figure 3.16: RCS pattern of FEKO simulated wood board 2 for HV-pol. A small cross polarization contribution is seen.

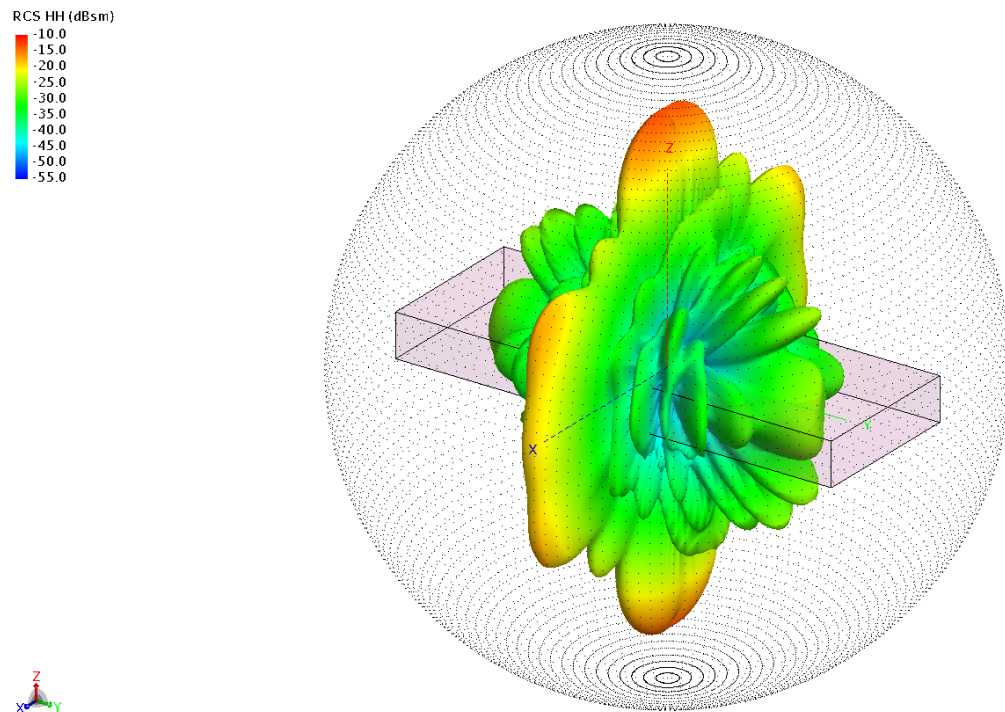


Figure 3.17: RCS pattern of FEKO simulated wood board 3 for HH-pol. The peak RCS level is slightly larger than that of wooden board 2 due to its slightly larger dimensions.

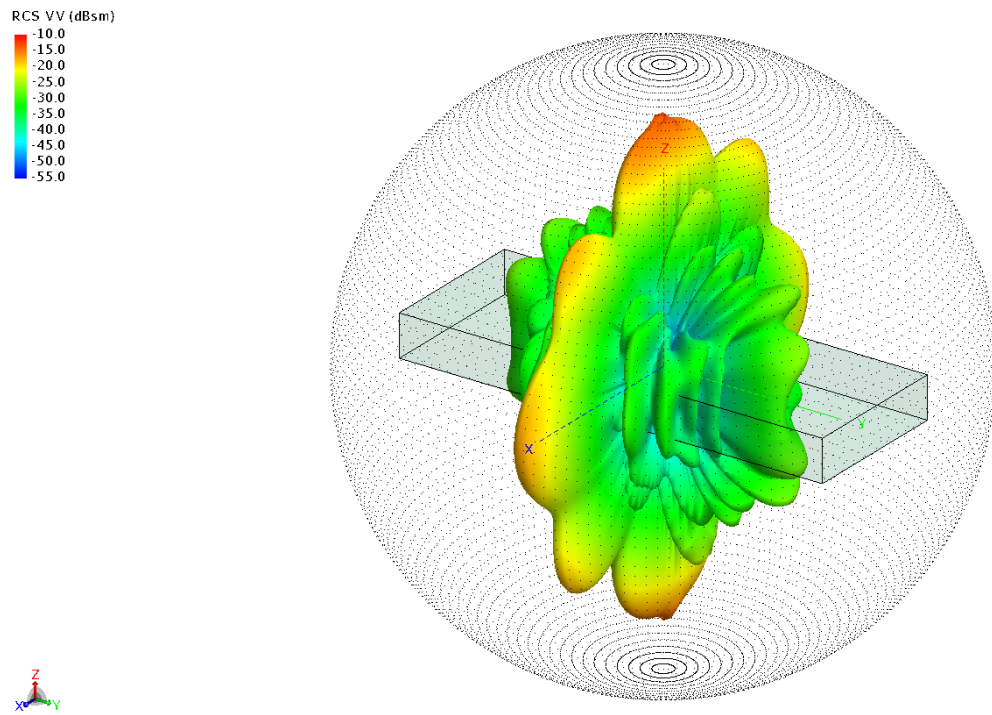


Figure 3.18: RCS pattern of FEKO simulated wood board 3 for VV-pol. RCS pattern similar to that of the HH polarization.

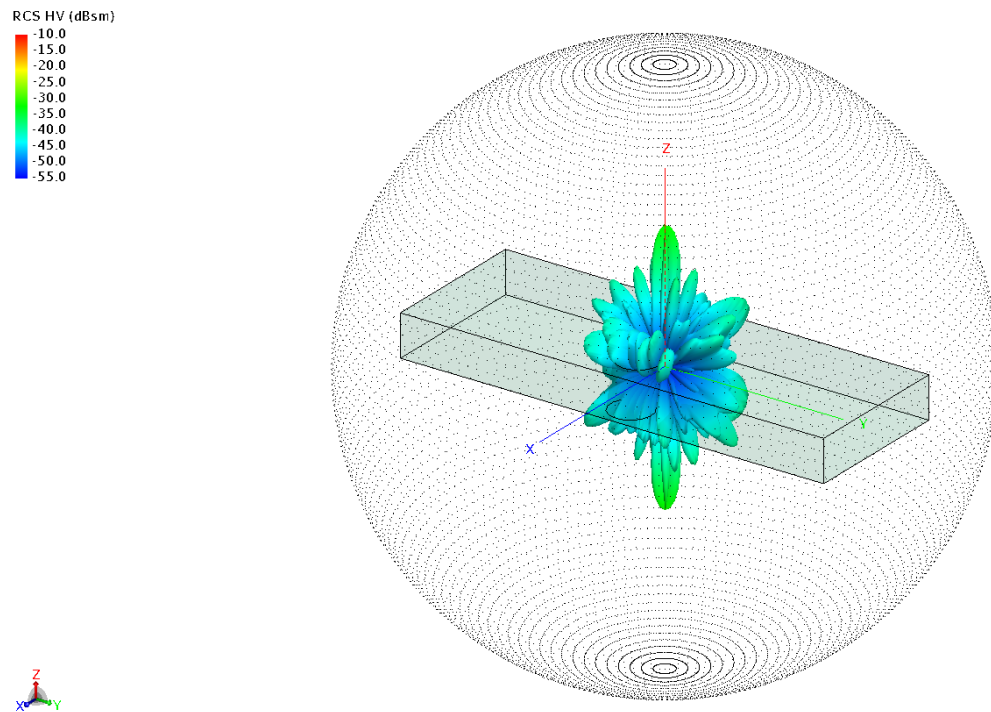


Figure 3.19: RCS pattern of FEKO simulated wood board 3 for HV-pol.

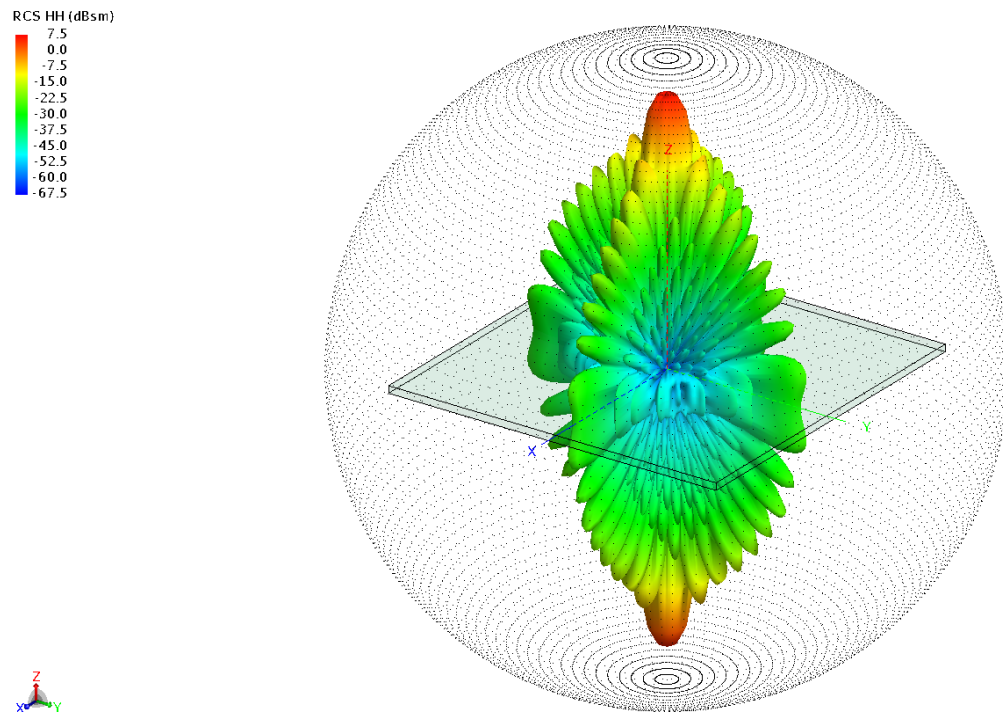


Figure 3.20: RCS pattern of FEKO simulated wood sheet for HH-pol. This is the largest target and it can be seen that it has the highest RCS, the most number of lobes, and the most number of nulls.

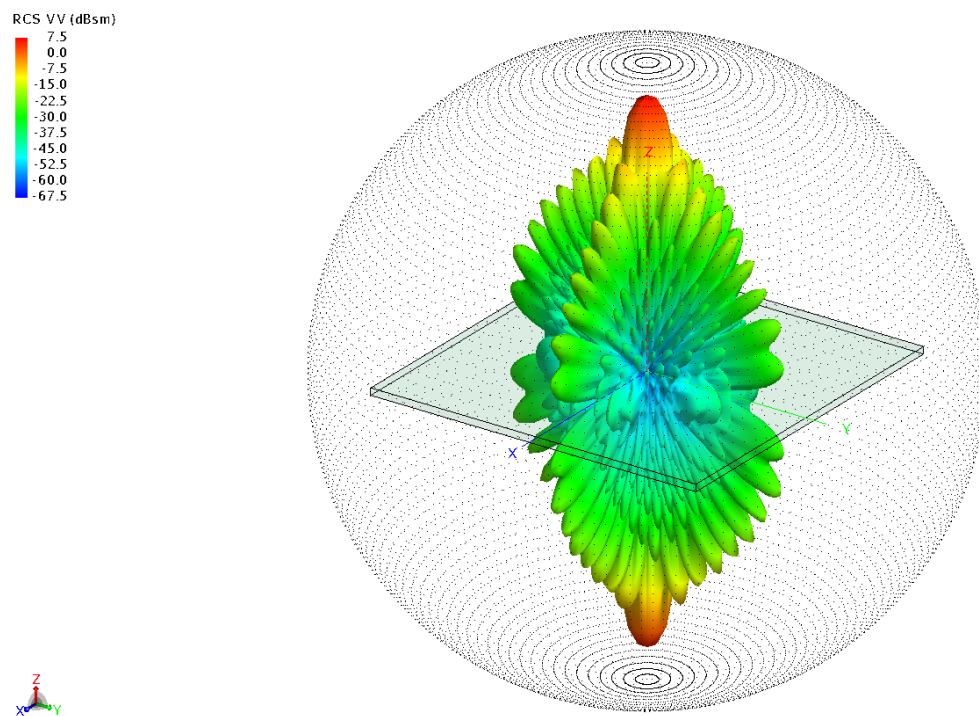


Figure 3.21: RCS pattern of FEKO simulated wood sheet for VV-pol. The RCS pattern is almost identical to that of the HH polarization.

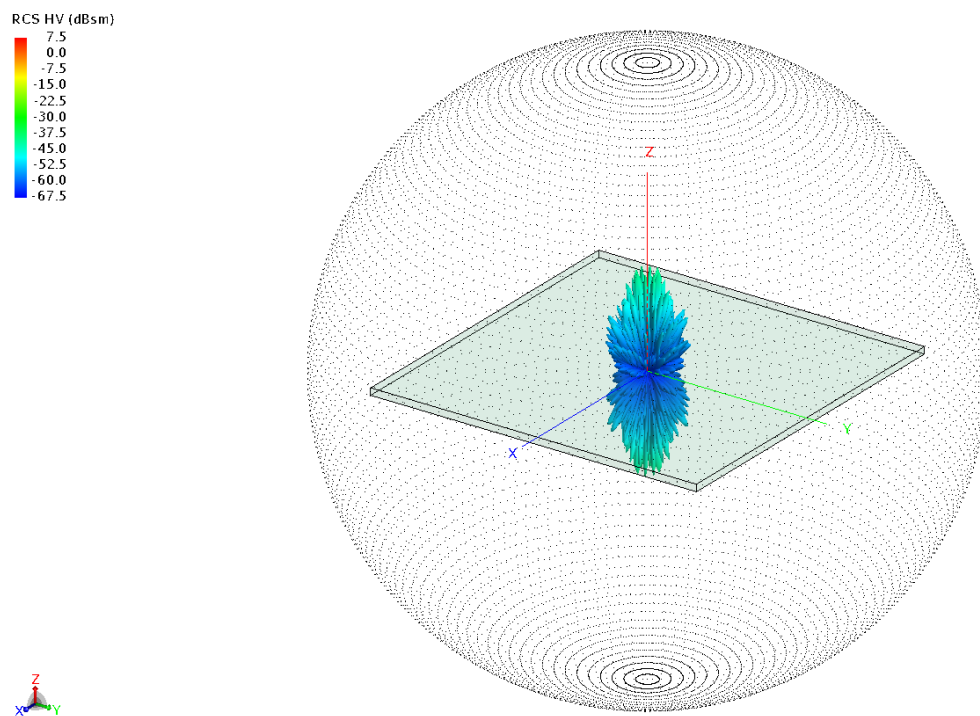


Figure 3.22: RCS pattern of FEKO simulated wood sheet for HV-pol. A small contribution from the cross polarization is seen here.

Figure 3.11 shows the RCS pattern for the Wood board 1 with HH polarization. The peak RCS level, located at broadside, is much higher than that of the leaf due to its larger dimensions. More lobes and nulls can be seen too compared to the leaf so the RCS will vary more with changing aspect angle. The RCS pattern for VV polarization (Figure 3.12) is almost identical to the RCS pattern for HH polarization. Figure 3.13 shows a small contribution from the cross polarization measurement which may be negligible anywhere but broadside.

The simulations for the Wooden board 2 are next. Figure 3.14 shows the simulated RCS pattern for the HH polarization. Compared to the leaf and Wood board 1, the peak RCS is lower and the main lobe at broadside is elongated along the x axis due to the larger difference between the length and width dimensions. The RCS for the VV polarization, as seen in Figure 3.15, is very similar to the HH polarization pattern, except that the elongation of the main lobe is even more pronounced due to the fact that the polarization is aligned to the largest dimension of the wooden board. The pattern for the HV polarization is seen in Figure 3.16 where its contribution is negligible except at broadside.

The RCS patterns for the Wooden board 3 are analyzed next. Figure 3.17 shows the HH polarization RCS pattern for Wooden board 3. It is fairly similar to the RCS pattern of Wooden board 2 in terms of magnitude and overall pattern, but the nulls near broadside are smaller. Figure 3.18 shows the pattern for VV polarization, which is similar to the pattern for HH polarization with the exception of a larger RCS along the x axis. And Figure 3.19 shows the cross polarization RCS pattern, which is small across the entire RCS pattern.

The last wooden target is the Wood sheet, which is also the largest object simulated. Figures 3.20 and 3.21 show the patterns for HH and VV polarization respectively and they are both extremely similar due to the fact that the face is a square.



The RCS peak is the largest of all objects which corresponds to the largest dimensions of all the objects. It can also be seen that it has the largest number of nulls and lobes which is characteristic as the target in question gets larger and approaches the optical scattering regime. The HV polarization pattern, shown in Figure 3.22, is extremely small compared to the HH and VV polarizations.

Different wooden targets were simulated in FEKO. A couple of features can be seen from these simulations. The peak RCS of the object increases as the dimensions increase and is located broadside of the largest face. Even though the RCS may be large at broadside, there are many nulls along the RCS pattern meaning that the objects will have negligible RCS at certain angles regardless of size. The largest object, the wooden sheet, has the largest peak RCS and also has the most number of lobes and nulls. It is also important to note that the wooden targets do not produce a significant cross polarization RCS signature shown in Figures 3.13, 3.16, 3.19, and 3.22.

### **3.4 HFSS Simulations**

A second solver was used to corroborate simulation results. Unlike FEKO, HFSS does require an ABC or a Perfectly Matched Layer (PML) to terminate the outgoing radiation. The way to draw objects in HFSS is very similar to FEKO where a cuboid and cylinder with the appropriate dimensions are joined together to get a single leaf. To create the PML needed an airbox around the target needs to be drawn where its dimensions have to be so that the sides are at least  $\lambda/4$  away from the target [22]. If time and resources are important then this airbox must be as small as possible following the  $\lambda/4$  rule because as the airbox increases so will the simulation space and it will take longer and require more computational resources to complete. Plane

wave excitations are requested for a whole sphere with steps of 2 degrees. Just like in FEKO the dielectric constants and loss tangents have to be imported. All targets were originally intended to be simulated on HFSS, but the larger wooden targets proved impossible to simulate due to the excessive memory and processing requirements they needed.

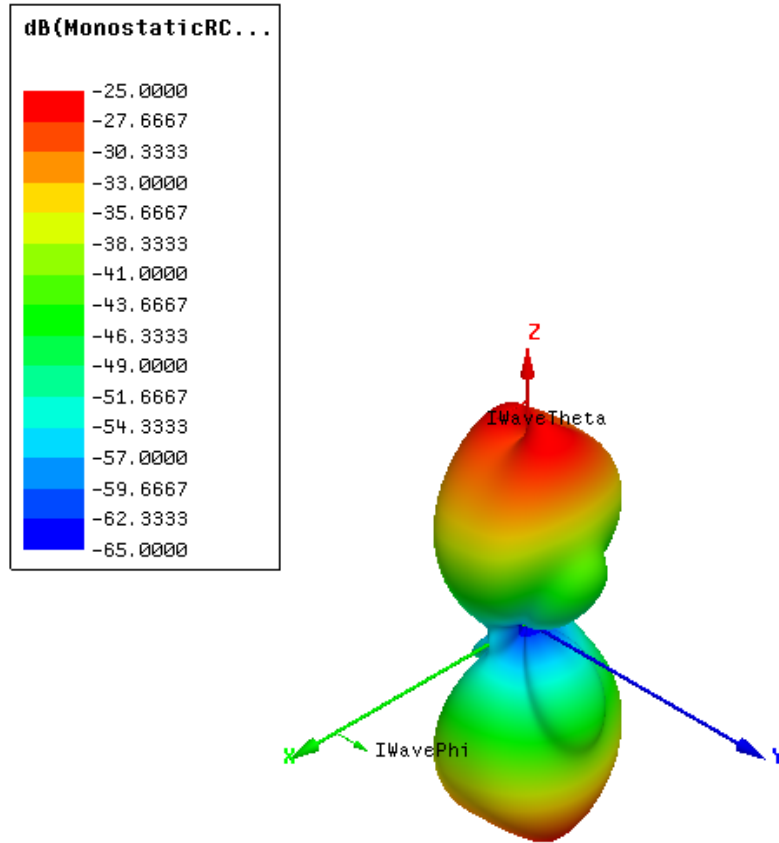


Figure 3.23: RCS pattern of HFSS simulated leaf for HH-pol. RCS pattern is similar to that of MATLAB and FEKO for the same polarization, where the RCS contribution by the cylinder's end-caps can be seen along the  $y$  axis.

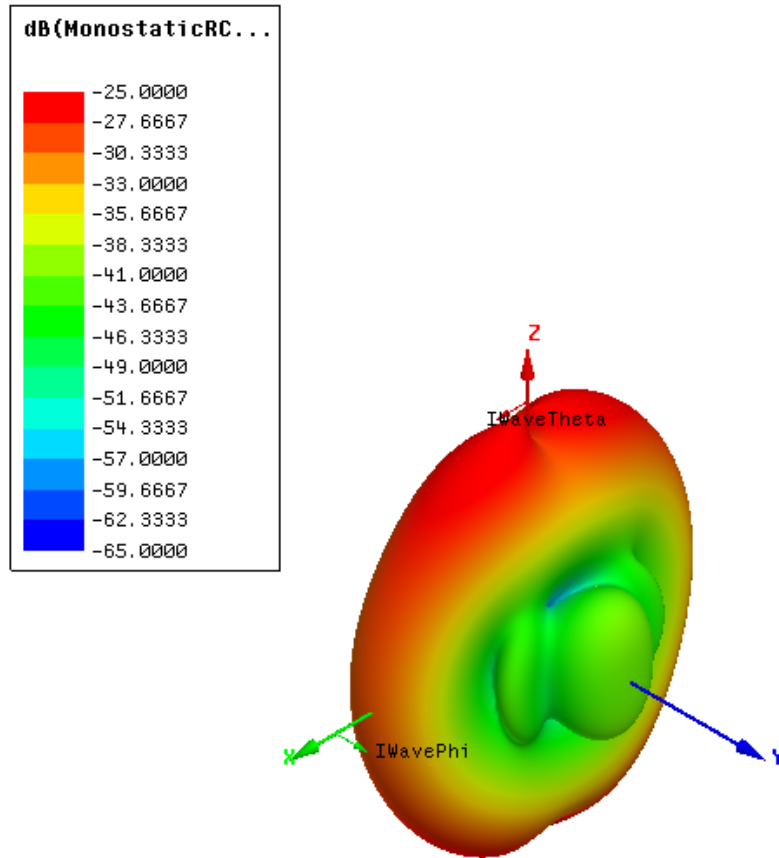


Figure 3.24: RCS pattern of HFSS simulated leaf for VV-pol. Notice that the cylinder provides a contribution to the RCS when the polarization is parallel to it as previously seen in the MATLAB simulation but was not present in the FEKO simulation.

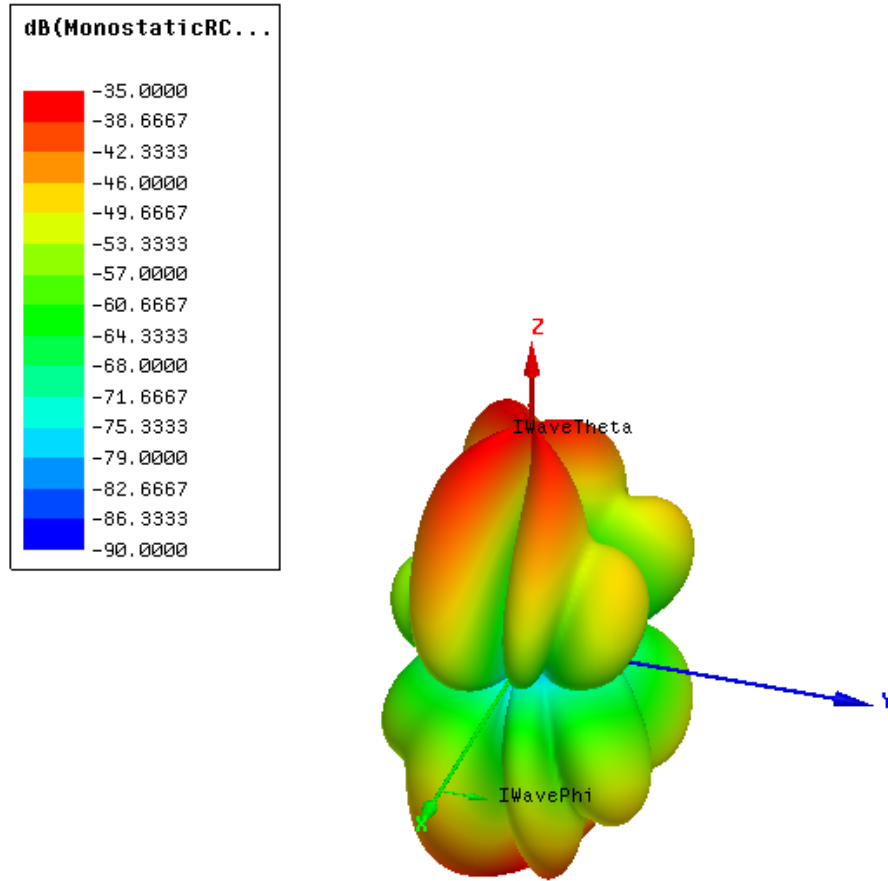


Figure 3.25: RCS pattern of HFSS simulated leaf for HV-pol. A small cross polarization contribution can be seen here and it is not entirely negligible at certain angles near broadside.

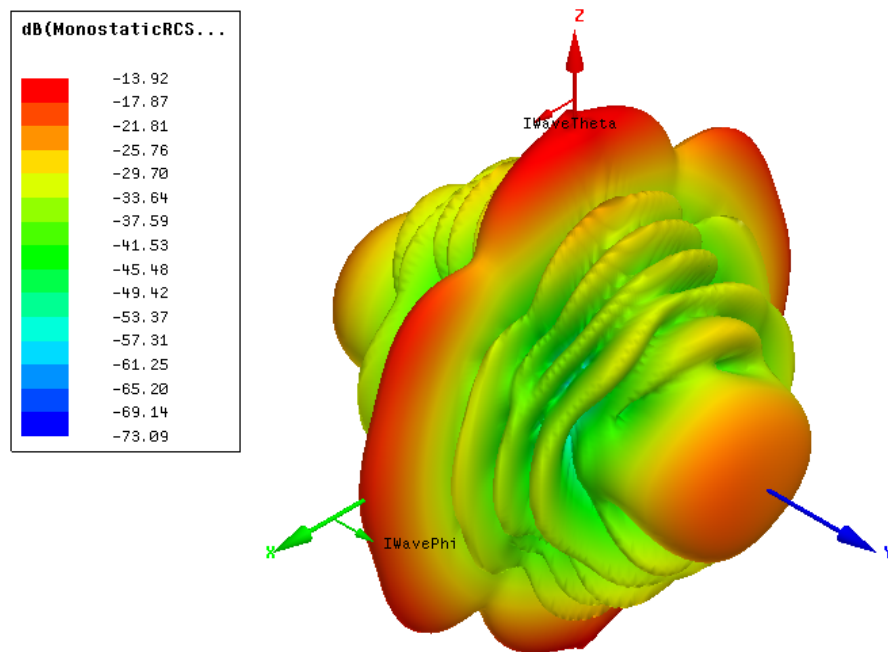


Figure 3.26: RCS pattern of HFSS simulated wood board 2 for HH-pol. RCS pattern is almost identical to the FEKO RCS pattern.

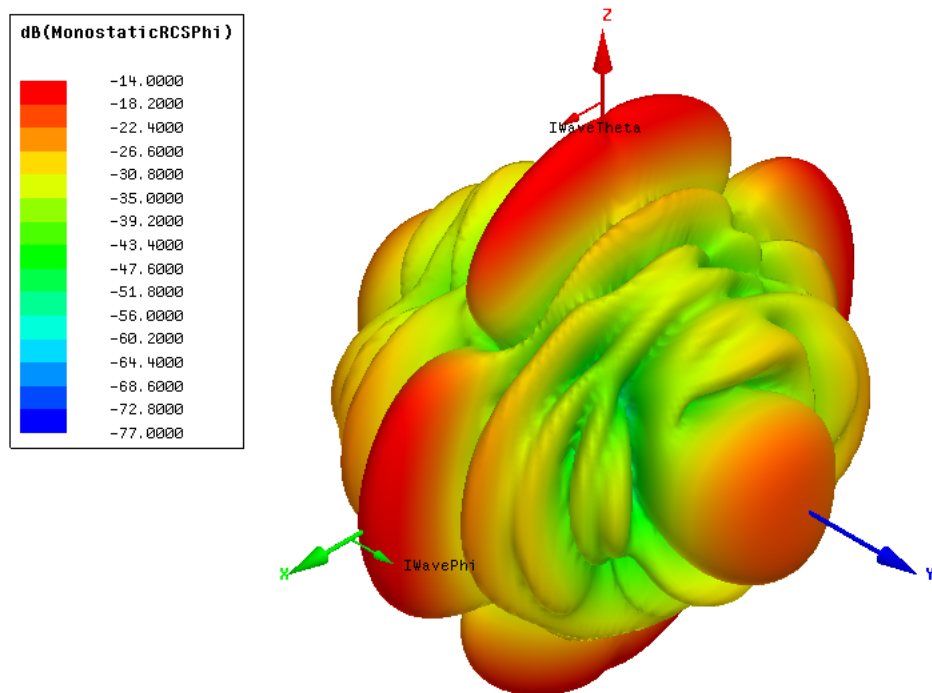


Figure 3.27: RCS pattern of HFSS simulated wood board 2 for VV-pol. RCS pattern is almost identical to the FEKO RCS pattern.

The leaf was simulated in HFSS. Figure 3.23 shows the RCS pattern for HH polarization. This pattern resembles that of the MATLAB and FEKO simulations well even in magnitude and it can be seen that it captures the effect of the cylinder's endcap by looking at the lobes along the  $y$  axis. Figure 3.24 shows the RCS pattern for the VV polarization. It agrees well with the MATLAB simulation where the side of the cylinder and sheet increase the RCS along the  $x$  axis but does not agree as well with the FEKO simulation that didn't capture this effect.

The Wooden board 2 was able to be simulated. In Figure 3.26 the RCS pattern for the HH polarization is shown. Similar to the FEKO simulation, the largest lobes are elongated because of the difference in the length and width dimensions. In Figure 3.27, the RCS pattern for the VV polarization can be seen and is very similar to that of the HH polarization with the exception that the lobes along the  $z$  axis become elongated due to the polarization being parallel to the largest dimension of the wooden board.

The HFSS simulations show very similar results compared to FEKO for the leaf and wooden board 2. Even though all the objects were not able to be simulated in HFSS, it provides answers in agreement with FEKO and shows that it can also be used to create the RCS library if the FEKO software is not available to the reader.

### **3.5 Conclusion**

The results provided here prove that an analytical solution of scattering can compare with a simulation by electromagnetic solvers for simple shapes. Depending on the needs and resources of research, analytical solutions may be used if accuracy can be sacrificed and electromagnetic solvers may be used if time and resources are of little concern. It is to be noted that there is a limit to electromagnetic solvers as it



may not be able to perform the simulation if the object's electrical size is too big as seen with the HFSS simulations.

The analytical model of the leaf fared well when compared against the results given from FEKO. This means that if the RCS of relatively simple objects is needed quickly, analytical models in MATLAB are feasible. But if not available, electromagnetic solvers can be used to generate the RCS patterns, and as compared with the leaf and the wooden board 2, FEKO and HFSS produce similar results making them both viable.

FEKO was the only solver able to simulate all the proposed scatterers and the results are turned into files that the tornado simulator can use to populate the simulated space with scattering debris. In order to verify that the simulations match real life observations, measurements of the wooden targets are obtained and shown in the following chapter.

## **Chapter 4**

### **Radar Cross Section Measurements**

#### **4.1 Introduction**

RCS measurements are important in industry and research. In the defense industry, RCS measurements are used to look into the scattering of a new design, to diagnose for places with high reflections, and to characterize potential targets for detection that friendly radars might encounter. For scientists, RCS measurements may be used to confirm theoretical results about scattering bodies, scattering mechanisms, and to even make a database for targets of interest. RCS measurements are taken in RCS measuring facilities which can be an outdoor or an indoor test range. Each one of these test ranges has its own advantage and disadvantage. Outdoor ranges are used when the target in question is large enough that it would require an inconveniently large and expensive indoor facility. Not only does a large object require more room but it will also dictate the distance requirement between the source and the target due to the far-field requirement. Having an outdoor test range means that measurements are vulnerable to weather, such as rain, wind, and dust that can disrupt measurements so fair days are required to make measurements [11], [23], [24]. Indoor test ranges, however, are impervious to inclement weather since measurements are made inside a building in an anechoic chamber. Although convenient,

anechoic chambers are costly and are relatively small so electrically large targets cannot be measured accurately because they might fail far-field requirement. This far-field requirement dictates that the test range, being indoors or outdoors, has to be large enough so that the source and the target are separated enough that the incident wave approximates a plane wave [7], [11], [13]. Literature suggests that the minimum distance should be [7], [11], [13]:

$$r \geq \frac{2D^2}{\lambda} \quad (4.1)$$

Where  $D$  is the largest dimension of the scatterer and  $\lambda$  is the wavelength of the incident wave. This approximation yields at most a 22.5 degree error [7], [11], [13]. This number is used as a rule of thumb but one that is used very often in electromagnetic research. The largest dimension of the largest target is 18 inches, or 45.72 cm, for the wooden sheet. At the operating frequency of 2.8 GHz the wavelength  $\lambda$  is 10.71 cm so the far field distance is 390.35 cm or almost 4 meters. the distance from the antennas to the target is 7 meters so the chambers are more than adequate to measure the largest target this thesis deals with.

The RCS measurements of the simulated debris are taken at the Radar Innovations Lab's so they can be compared to their simulations. The facility's anechoic chamber has the instrumentation necessary to make RCS measurements such as a network analyzer, azimuth rotating pedestal, transmitting rotating pedestal, S-band antennas, motor controls, and computer. The chamber operates from 300 MHz to 10 GHz, making it a versatile measuring range.

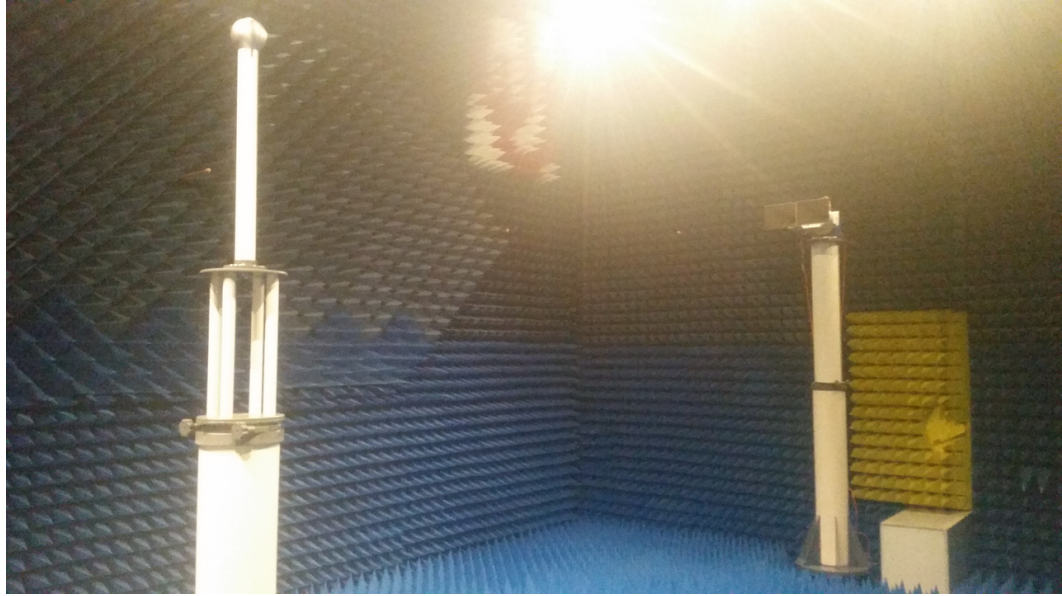


Figure 4.1: Inside the far-field anechoic chamber. The transmit and receive antennas are located in the far right of the picture, while the target to be measured rests in the pedestal on the left of the picture.

## 4.2 Monostatic vs Quasi-Monostatic Measurements

The antennas use for the measurements are two standard gain S-band horn antennas by Nearfield Systems Inc. (NSI) model NSI-RF-SG284 mounted side by side. The bracket used for mounting the antennas was machined in-house. The polarization of the antennas once mounted is H-pol. Mounting the horn antennas side by side, as seen in Figure 4.1, means that the measurements taken are not exactly monostatic but quasi-monostatic, meaning that the transmit and receive antennas are not collocated and create a small, but mostly negligible, bistatic angle [12]. Because our system is a Continuous Wave (CW) system, a true monostatic configuration is not possible so quasi-monostatic measurements are taken. To ensure that the quasi-monostatic measurements are not too different from true monostatic measurements, the RCS of a sphere is calculated in MATLAB in a monostatic and quasi-monostatic environment and compared. For this the bistatic angle created by the horn antennas

in the chamber is calculated. The distance separating the centers of the horn antennas once they are mounted is measured and the distance between the phase center and the target in the chamber is measured so that the quasi-monostatic angle can be calculated.

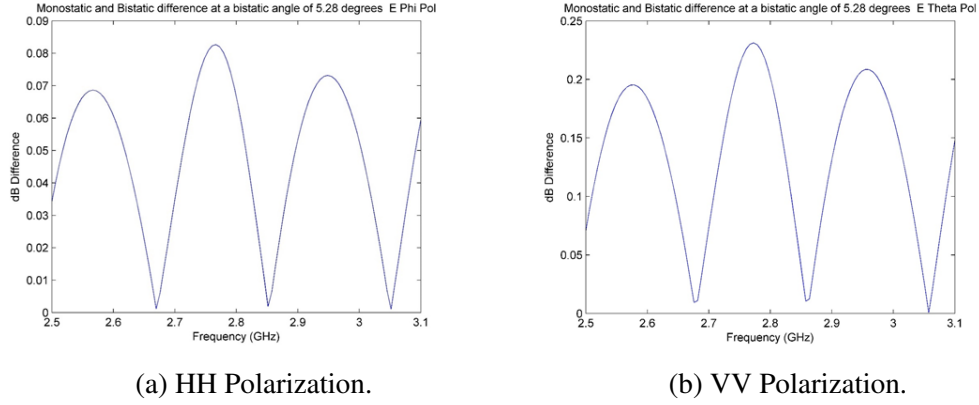


Figure 4.2: Difference between the monostatic and quasi-monostatic RCS configuration of a sphere. While the VV polarization exhibits the largest difference, both polarizations exhibit a negligible contribution from the quasi-monostatic configuration.

It is seen in Figure 4.2 that the values for monostatic and quasi-monostatic do vary, but so slightly that it is considered negligible so the measurements taken in the chamber are, for all intents and purposes, monostatic measurements.

### 4.3 Calibration

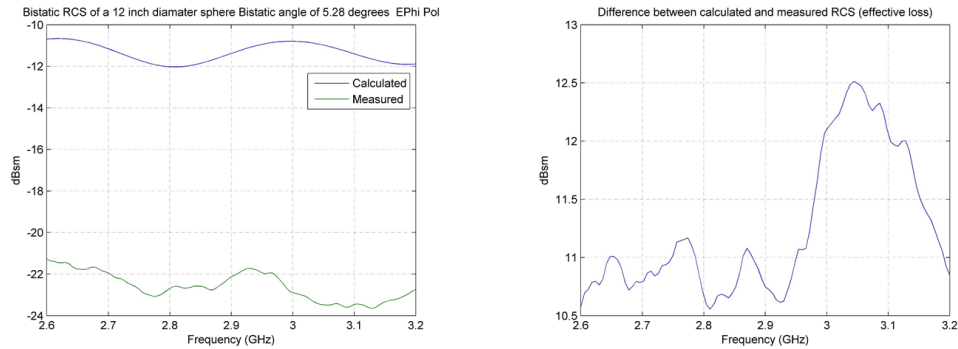
Before making measurements of the targets in the chamber, a calibration must be done. Calibration sets an absolute RCS that helps compute the losses in the measuring system. Metallic spheres are used as calibration targets due to their RCS being independent of aspect angle and is only dependent on frequency.

By taking a measurement of a calibration sphere in the chamber, we can compare the measurement to a calculated RCS of the same sphere in MATLAB and



Figure 4.3: 12 inch diameter calibration sphere. A metallic perfect sphere is used here for chamber calibration procedures since its RCS is independent of aspect angle.

effectively obtain the losses generated in the chamber and by the equipment and cables that otherwise would be difficult to calculate.



(a) Measured and calculated RCS.

(b) Difference of measured/calculated RCS.

Figure 4.4: Calibration by taking the difference between the measured and calculated RCS of a 12 inch diameter calibration sphere. The difference is the combined effective loss from the chamber, cables, and instrumentation. This loss is added to future measurements to obtain the target's true RCS.

A 12 inch diameter calibrations sphere, as seen in Figure 4.3, is used for the chamber calibration. A simulations of the RCS for a sphere of the same diameter is ran in MATLAB, where the difference between the measurement and the simulation

is considered the loss and it has to be added into the debris measurements and the results can be seen in Figure 4.4. This figure also gives insight about the limitations of absolute RCS measurements as it shows that the measurement of a perfect sphere has errors within 0.5 to 1dB. This means that the measurements of the following objects will also more than likely exhibit very small margin of error but will not impact the results in a major way.

#### 4.4 Chamber Characteristics

Pyramidal absorbers cover the walls, ceiling, and floor of the chamber to reduce unwanted reflections, though it does not cancel them completely. To keep the noise low in the measurements an IF bandwidth of 20 Hz was used. The bandwidth is directly related to the noise energy in the signal and using a low IF bandwidth will further reduce the noise contributed by the chamber and cables [25].

$$E^2 = 4RkTB \quad (4.2)$$

Where  $E$  is the noise voltage,  $R$  is the resistance,  $k$  is Boltzmann's constant,  $T$  is the absolute temperature, and  $B$  is the bandwidth. This shows that there is a direct relationship between bandwidth and noise power so a lower IF bandwidth results in less noise being introduced into the measurements. Unfortunately, there is an inverse relationship between measurement time and IF bandwidth [25] so a compromise is needed for a low noise and quick measurement. The 20 Hz IF bandwidth was selected to meet this compromise. The target support that goes in the chamber is important to take into account as it will create unwanted scattering. By manipulating the shape and material properties of the support column the scattering produced by it can be minimized [11], [24]. A pylon is a very common support

where the ogive cross section helps direct the scattering away from the receiver [11]. A support made from a dielectric material with low dielectric constant will still produce scattering but much lower than the target's RCS [11]. Support columns made from dielectric materials are not as structurally sound as metallic support columns so heavier targets may not be supported by these dielectric material supports. The targets used here are relatively light and can be supported by non-metallic materials.

The azimuth rotating positioner in the chamber has a large telescoping plastic tube that uses pneumatics to raise the target into the main beam of the antennas. The cross section of the plastic tube is rather large and do not wish to introduce this into the main beam to avoid unwanted scattering. To mitigate this, a cardboard poster tube with a much smaller cross section is used as a support column for the targets and is mounted on top of the large plastic tube. This allows for the larger plastic tube to be out of the main beam of the antennas and minimize any contribution to the RCS measurements.

Because of the inability to use pulses and range gating in the chamber, another method has to be used to ignore the scattering produced by the reflection of the chamber itself since the absorbers will not attenuate the scattering completely. To account for the chamber scattering, vector subtraction is performed between the chamber scattering and target scattering. To do this, a measurement of the chamber and the support column, without the target, is done and the I/Q data are recorded and stored. Next, a measurement of the target is done and its I/Q data are stored. To effectively remove the chamber's signature, a vector subtraction is done from the measurement of the target minus the measurement of the chamber. If the measurements go on for more than a day, a measurement of the chamber has to be done at the beginning of the next days as the variations in temperature and environment may occur and will have an effect on the repeatability of the measurements as it can



be seen in Figure 4.5.

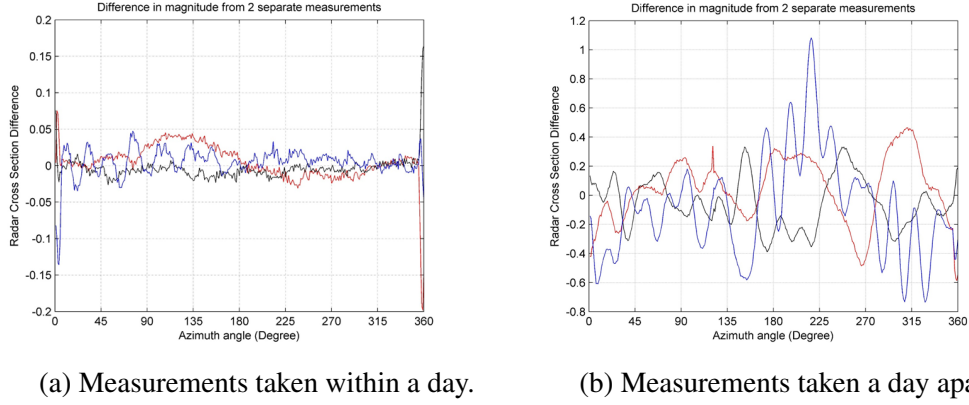


Figure 4.5: RCS difference of 2 sphere measurements taken at different times. Measurements taken within a day exhibit very little difference while measurements taken a day apart have a much larger difference that may impact the overall result.

Measurements are taken for all targets for a full azimuth sweep (360 deg). Only H-pol measurements are taken even though the ability to measure V-pol is available. The reason for taking H-pol measurements is because single pol weather radars are most commonly H pol. Something to note is that while the simulations can produce a 3D RCS pattern, the chamber measurements are limited to an azimuth cut due to the chamber only possessing an azimuth positioner and there is no other mechanism to change the elevation angle. Although a measurement of a leaf of comparable size to the previous simulations was planned, it was revealed during the ongoing measurements that the chamber did not have the necessary sensitivity to accurately measure such a small dielectric object. Agreement between simulations using PO and chamber measurements of a leaf have been recorded [7] which gives the PO simulations of the leaf high confidence.

## 4.5 Results

In this section the results of the measurements of the wooden targets are shown alongside a comparison between the chamber measurement and the FEKO simulation.



Figure 4.6: Picture of Wood board 1 to be measured. Length: 0.2794 m. Width: 0.1397 m. Thickness: 0.01587 m.

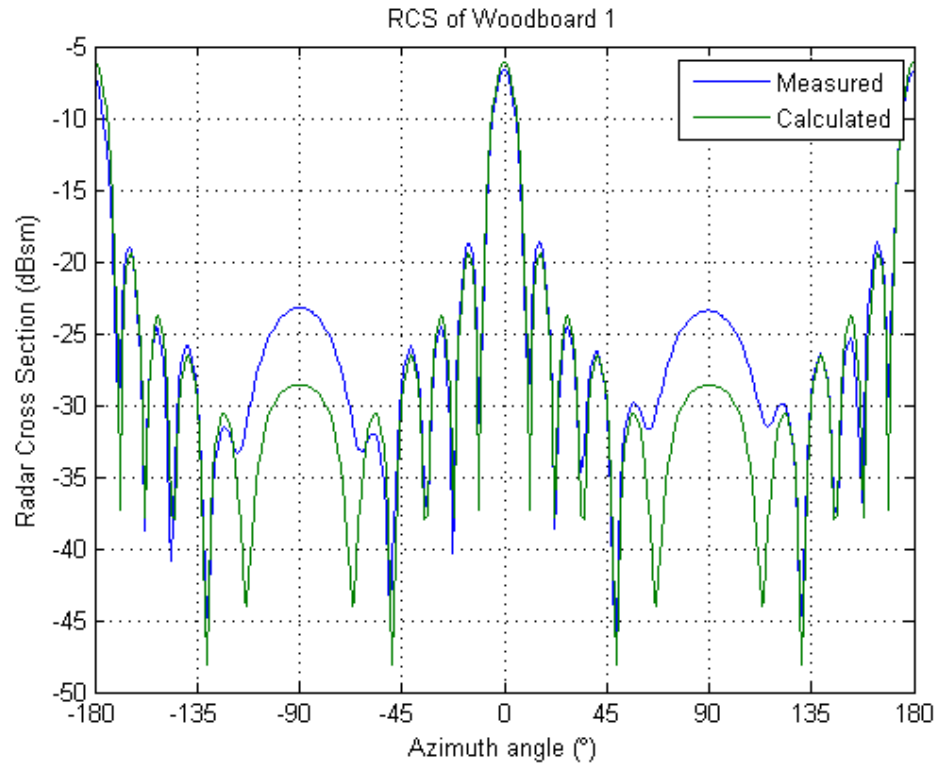


Figure 4.7: Comparison between measurement and FEKO simulation of wood board 1. Agreement between measurement and simulation is excellent at and near broadside with the larger discrepancies being around grazing angle.



Figure 4.8: Picture of Wood board 2 to be measured. Length: 0.3683 m. Width: 0.0889 m. Thickness: 0.0381 m.

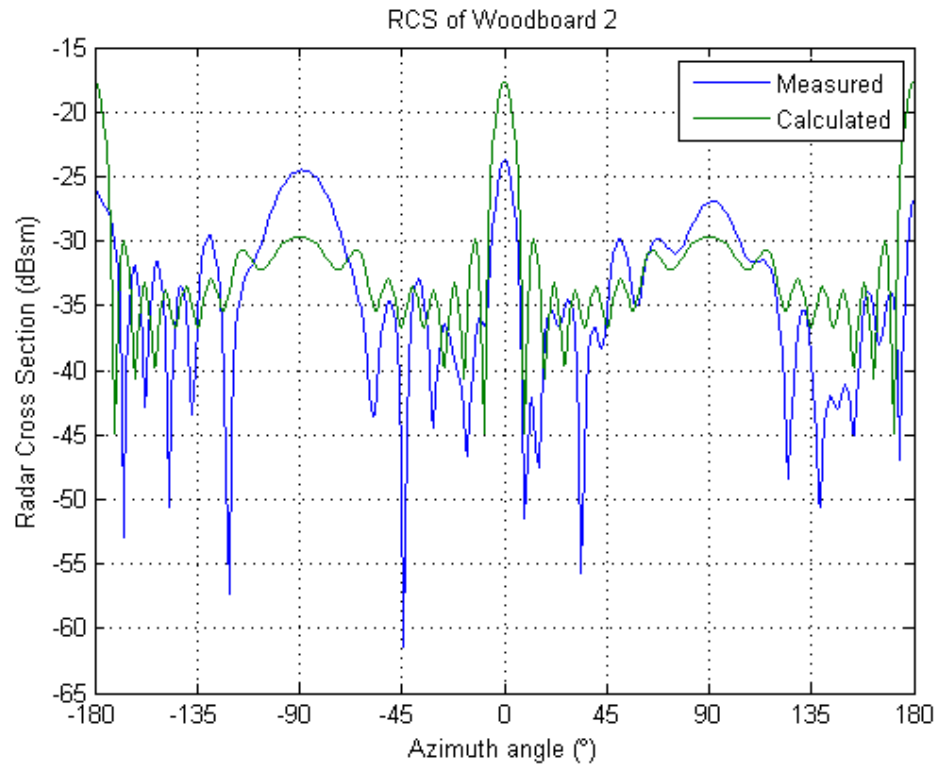


Figure 4.9: Comparison between measurement and FEKO simulation of wood board 2. There is discrepancy in the magnitude between the measured and calculated pattern throughout all angles. Misalignment of target to the main beam may be the cause.



Figure 4.10: Picture of Wood board 3 to be measured. Length: 0.3937 m. Width: 0.1397. Thickness: 0.0381 m.

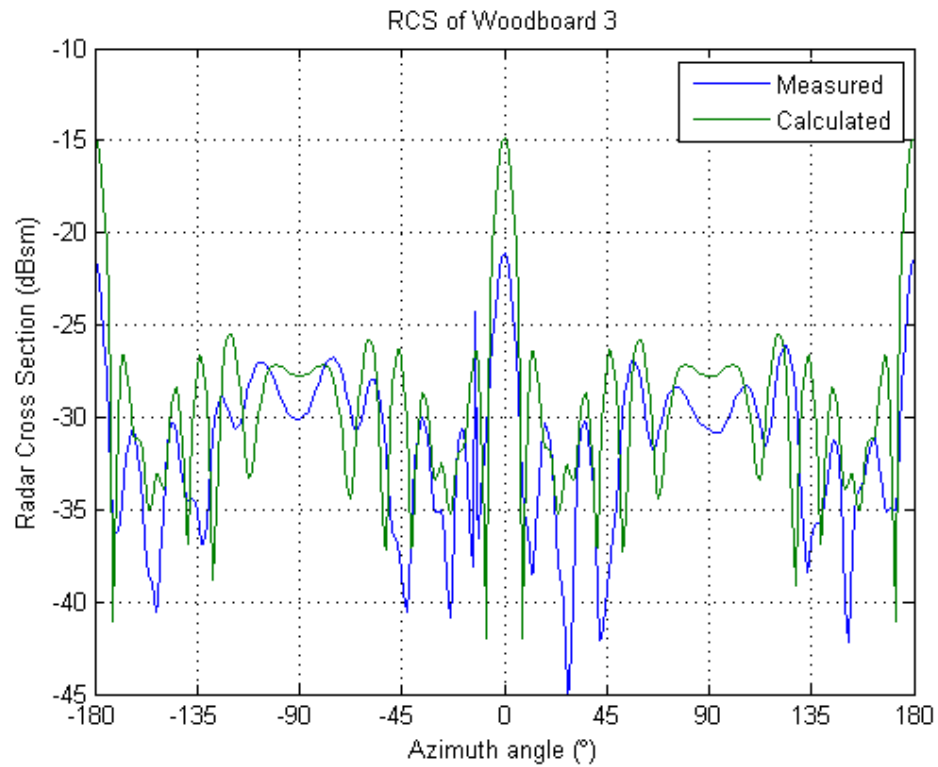


Figure 4.11: Comparison between measurement and FEKO simulation of wood-board 3. Magnitude discrepancies can be seen again between the measurement and the simulation, thought to be from misalignment between target and antenna beam. The patterns, however, are consistent between them.



Figure 4.12: Picture of Wood sheet to be measured. Length: 0.4572 m. Width: 0.4572. Thickness: 0.009525 m.

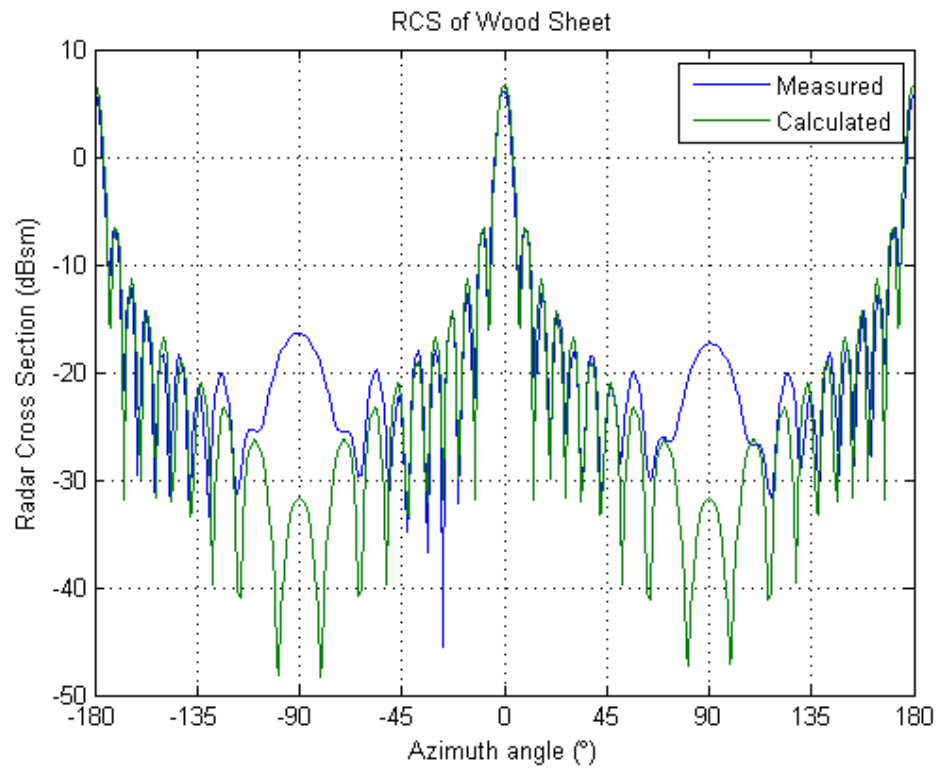


Figure 4.13: Comparison between measurement and FEKO simulation of wood sheet. Just like with Wood board 1, the patterns between the measurement and simulation agree well throughout most angles except near grazing angle.

The first target measured was Wooden board 1 as shown in Figure 4.6. Once the measurement was taken, it was plotted alongside the FEKO simulation for comparison. Figure 4.7 shows the plots from the measurements and FEKO. Both FEKO and the simulations agree quite well especially at and around broadside and become less agreeable near the grazing angle (90 degrees).

The second target is Wooden board 2 shown in Figure 4.8. The plot comparing its measurement and FEKO simulation is shown in Figure 4.9. Here the discrepancy between measurement and simulation is rather large despite the fact that the type of wood is the same for all wooden targets. This may be attributed to misalignment of the target to the antenna beam of the chamber.

Just like it happened in the measurement for Wooden board 2, Wooden board 3 (Figure 4.10) measurement's suffers from apparent misalignment as seen in Figure 4.11. The general pattern between measurement and FEKO simulation is fairly close but the magnitude offset is the biggest discrepancy seen that might be attributed to poor alignment between target and antenna beam.

And finally, the Wood sheet (Figure 4.12) is measured and compared to FEKO simulations. As shown in Figure 4.13, the agreement between measurement and simulation is excellent except at grazing angle, just like in the case for Wooden board 1.

Figure 4.7 and 4.13 show the best agreement between measurement and simulation. This may be due to their larger sizes which is easier for the equipment to detect. Wood board 2 (Figure 4.9) and 3 (Figure 4.11), however, show strong similarities in the RCS pattern shape but the magnitudes are offset. The materials of all the wooden structures are the same, which lead to believe that the smaller size was to blame for this discrepancy. The size combined with its dielectric properties, which make them reflect less power, might have put the target's RCS signature very

near the chamber's noise floor. It may also be because the target may not have been aligned correctly to the antenna beam. This shows that much care is needed if good RCS measurements are wanted.

## **4.6 Conclusion**

A twelve inch diameter sphere was used for the chamber calibration. This gives us the total chamber of the losses and it has to be done daily if the measurements require several days to complete. Even though the chamber has a quasi-monostatic configuration, this creates a negligible contribution and a monostatic configuration can be assumed.

The results of the FEKO simulations match the measurements taken of the wooden targets. It is to be noted that Wooden board 1 and the Wood sheet have a better match between measurements and simulations compared to the smaller wooden targets Wooden board 2 and 3. This may be because the chamber's ability to accurately measure a target is inversely proportional to the target size since CW configuration is used. Even though a low IF bandwidth is used to reduce the amount of noise introduced in the measurements, a range gated system may perform much better for the measurements of small targets. Nevertheless the agreement between the simulations and measurements of the larger wooden targets results in high confidence for the simulation results and that the RCS in the tornado simulator will be depicted accurately.



## **Chapter 5**

### **Multiple Scattering**

#### **5.1 Introduction**

An RCS library has been generated for the tornado simulator. With this RCS library, TDS can be recreated in the tornado simulator and the results analyzed giving scientists the ability to look into the mechanisms behind the TDS phenomena. The total scattering from the debris in the simulation volume is the added scattering from each individual scatterer using superposition. This, however, means that only single reflection scattering takes place in the simulator, meaning there's no electromagnetic interaction between the scatterers. On the other hand, multiple scattering occurs when the scattered waves interact and reflect off the rest of the targets before scattering back to the radar. In short, single scattering is when each target scatters independently from the other targets, and multiple scattering is dependent on the interaction between scatterers.

Because the complexity of multiple scattering of random targets is high, only single scattering was implemented in the tornado simulator, meaning that the effects of multiple scattering are not taken into account. Multiple scattering may be an important factor for the radar return signal as it may create constructive/destructive interference, depolarization, specular regions, etc. To explore whether multiple

scattering is needed in the tornado simulator, an analytical method is implemented to create multiple scattering between small cylinders and plates. Only first order multiple scattering is explored here.

## 5.2 Cylinder Multiple Scattering

The first object used for multiple scattering analysis is the small cylinder which yields a good starting point for creating the framework for multiple scattering. Cylinders that are electrically small can be modeled as dipoles due to the Rayleigh scattering mechanisms. Dipoles can be used as scatterers thanks to the scattering relationship with antenna parameters [26], [27].

The overall process for the multiple scattering from cylinders is as follows. An incident wave is launched at the cylinders to be used as scatterers. The current induced due to the incident field is calculated for each cylinder individually. Next, the scattered field from one of the cylinders due to the induced current is calculated and treated as an incident wave for the rest of the cylinders is taken to be an incident wave for the rest of the cylinders. The current induced by this secondary incident wave is calculated and added to the original induced current. The process is repeated until all the cylinders have had their scattered field contribute to the induced currents. All the current contributions in each cylinder are added and their total cylinder scattering fields calculated. The total cylinder scattered fields from all the cylinders are added to obtain the total scattered field and the total RCS. The theorems behind this model are explored next.

Using antenna theory, the far field radiated by a dipole with a linear current distribution of  $I_0$  is acquired. To satisfy this linear current approximation, the dipole must have a length of  $L \leq \lambda/50$  according to [28]. But since this is already an

approximation slightly larger cylinders would still be valid if needed. Calculated by using the operating wavelength we obtain a length of 1cm. The diameter for the dipole is chosen to be 1 mm since the approximation holds true for thin dipoles.

For a single small dipole, the radiated field by a linear current is [28]:

$$E_\theta \simeq j\eta \frac{kI_0 l e^{-j\beta r}}{8\pi r} \sin \theta. \quad (5.1)$$

where  $l$  is the length of the dipole  $I_0$  is a constant current due to the dimension of the dipole.

Because multiple dipoles are simulated together, mutual impedance effects take place and are taken into account. By evaluating small resonant scatterers, the mutual impedance of two nearby loaded cylinders is derived by [29]:

$$Z_m \approx \frac{\eta}{2\pi} \left[ \frac{(kb)^2}{12} - j \frac{3\ln(2b/a) - 7}{kb} \right]. \quad (5.2)$$

where  $a$  is the radius of the dipole and  $b$  is the length of the dipole. With the mutual impedance known, the open-circuit voltage on the dipole is needed so that the current can be solved for so that the scattered field can be known.

While the open-circuit voltage of a transmitting antenna can be readily computed, the open-circuit voltage for a receiving antenna has to be calculated by other means. The reciprocity theorem is employed as it can show the relationship between its receiving characteristics to its transmit characteristics [30], [31]. The derivation begins by using the reaction concept [30], [31] where two different source,  $\mathbf{J}_a$  and  $\mathbf{J}_b$ , close to each other radiate fields  $\mathbf{E}_a$ ,  $\mathbf{H}_a$  and  $\mathbf{E}_b$ ,  $\mathbf{H}_b$  respectively. The reaction between source  $\mathbf{J}_a$  and fields  $\mathbf{E}_b$  is:

$$\langle \mathbf{J}_a, \mathbf{E}_b \rangle = \int \mathbf{J}_a(\mathbf{r}) \cdot \mathbf{E}_b(\mathbf{r}) d\mathbf{r}. \quad (5.3)$$

A system is reciprocal if:

$$\langle \mathbf{J}_a, \mathbf{E}_b \rangle = \langle \mathbf{J}_b, \mathbf{E}_a \rangle \quad (5.4)$$

which holds true for passive antennas and is not true for active systems such as phased array antennas. By using the reciprocity theorem and computing a Thevenin equivalent, a derivation of the open-circuit voltage of an antenna results in [31]:

$$V_{oc} = \frac{1}{I_0} \frac{4\pi j r e^{j\beta r}}{\omega \mu} E^{inc} \hat{p} \mathbf{E}^t(\mathbf{r}) \quad (5.5)$$

where  $E^{inc}$  is the incident wave on the dipole and  $\mathbf{E}^t$  is the radiated field of the dipole as a transmitting antenna. Using (5.1) as the transmitted field for (5.5), the open-circuit voltage used for the simulations is:

$$V_{oc} = -\hat{\theta} \frac{\eta k l}{2\omega \mu} E_{inc} \sin \theta \quad (5.6)$$

The current induced on the dipole by the incident wave and with mutual coupling taken into account is:

$$I_0 = \frac{V_{oc}}{Z_m} \quad (5.7)$$

where  $Z_m$  is the mutual impedance shown in (5.2).

This multiple scattering model is implemented in MATLAB. The way it works is a plane wave is launched at the targets, in this case dipoles. The current induced on the dipoles due to the plane wave is calculated by finding the open circuit voltage and dividing it by its impedance by using equations (5.6) for the open circuit voltage and (5.7) for the mutual impedance. Once the current has been computed, a loop begins where the scattered field due to the current induced by the plane wave is calculated and used as an incident wave for the rest of the dipoles. The current

on the dipoles is calculated due to the scattered field of the first dipole and stored. Another cylinder is selected and the whole process is repeated until all the dipoles contributed to the total current. All the currents induced in each dipole are added, and the total scattered field is calculated by adding the scattered field from each dipole.

To ensure that multiple scattering is effectively happening in the MATLAB simulations, the RCS of two colinear dipoles is taken as a function of dipole length and distance from one another is shown. with no multiple scattering the scattering will undergo constructive and destructive interference every time the dipole reaches a multiple of  $\lambda/2$  length or a multiple of  $\lambda/4$  distance from the other dipole. With multiple scattering however, there is a coupling effect on the dipoles and will contribute to an increase of RCS in several positions.

RCS of 2 Dipoles as a function of dipole length and distance (No Multiple Scattering)

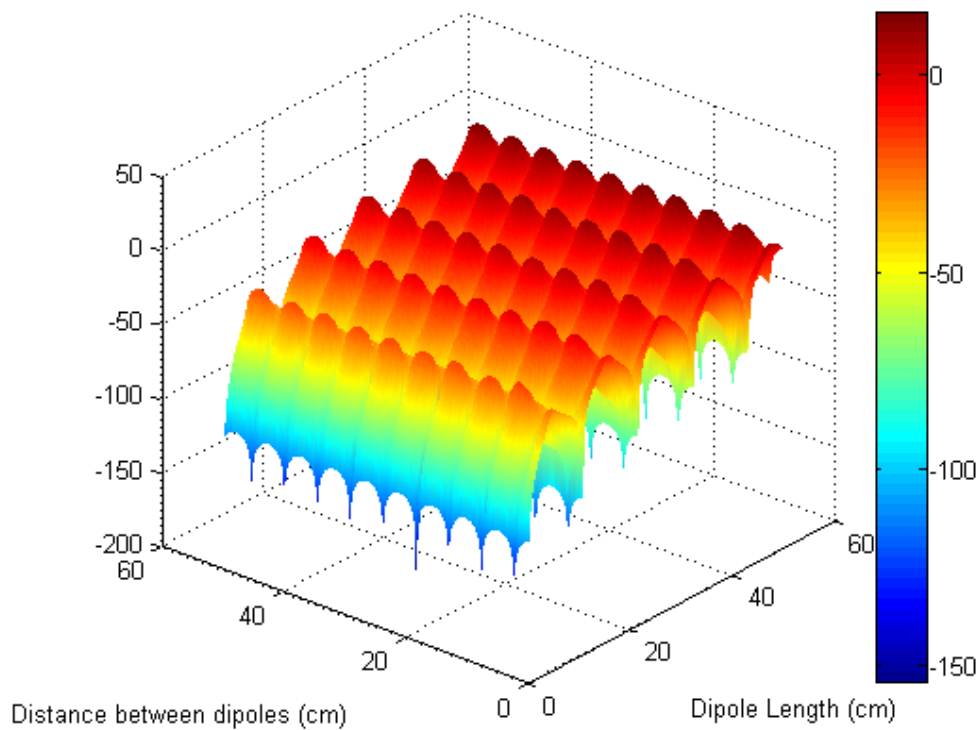


Figure 5.1: MATLAB RCS simulation of 2 cylinders with no multiple scattering taken into account (3D view). The RCS changes as a function of distance but due to the constructive/destructive interference at every time the dipoles are placed  $\lambda/4$  or  $\lambda/2$  distance apart. The RCS does increase as a function of size but this is to be expected since larger objects create larger RCS levels.

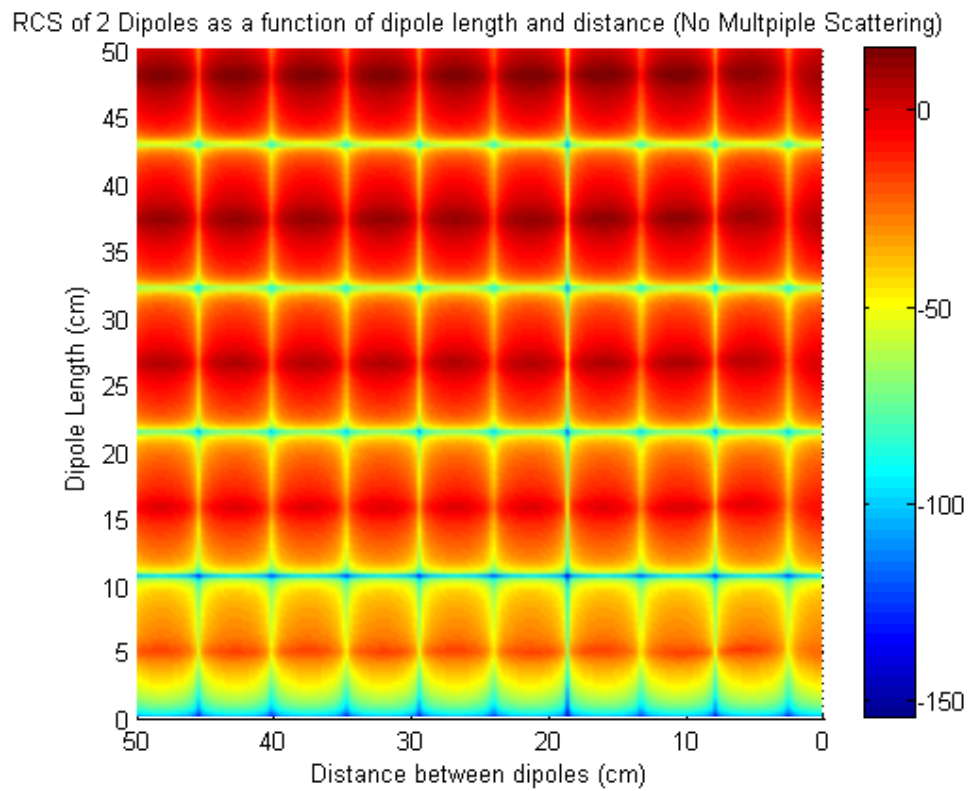


Figure 5.2: MATLAB RCS simulation of 2 cylinders with no multiple scattering taken into account (2D view). Same as Figure 5.1 but in 2D for easier viewing.

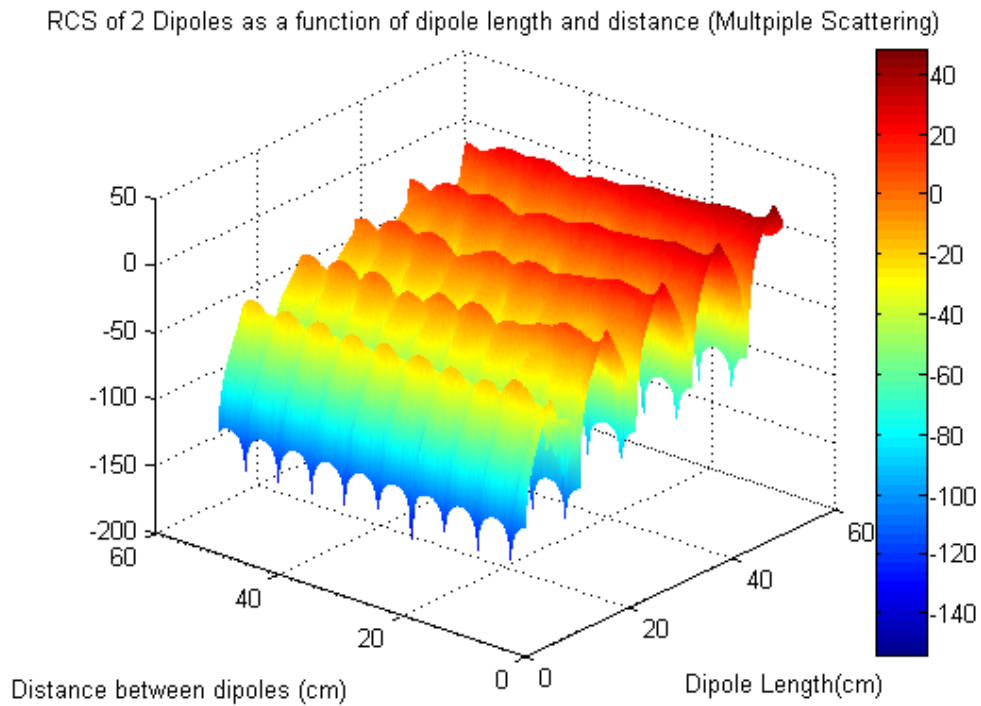


Figure 5.3: MATLAB RCS simulation of 2 cylinders with multiple scattering taken into account (3D view). In this plot, the effects of multiple scattering can be seen clearly for the RCS of the dipoles decreases as the distance between them increases. This can be seen for larger dipoles and multiple scattering has little effect with smaller dipoles.



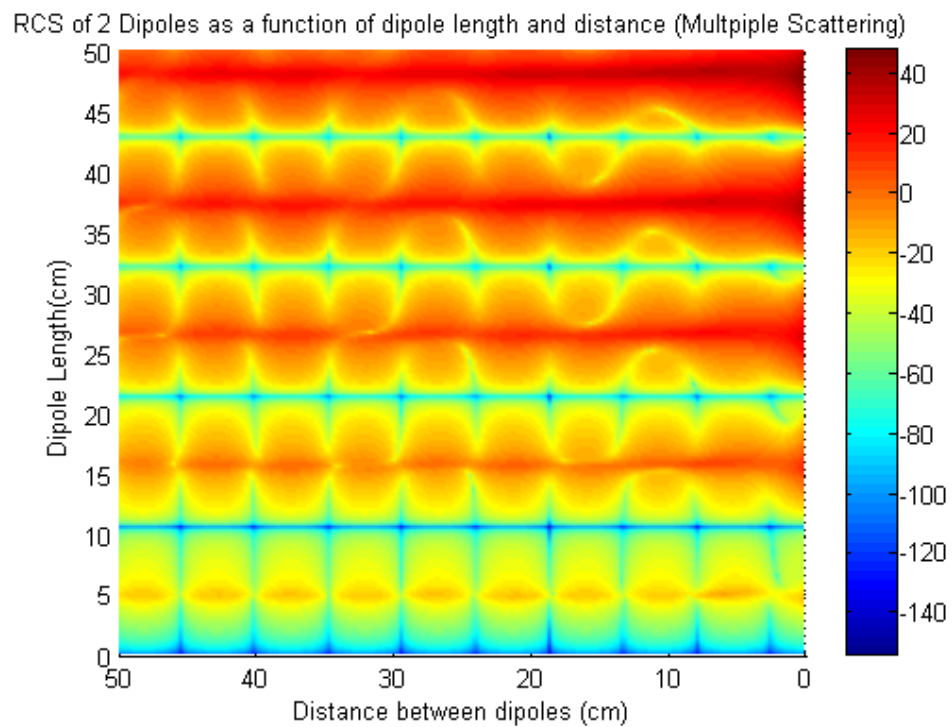


Figure 5.4: MATLAB RCS simulation of 2 cylinders with no multiple scattering taken into account (2D view). Same as Figure 5.3 but in 2D for easier viewing.

RCS difference of 2 Dipoles as a function of dipole length and distance (Multiple Scattering)

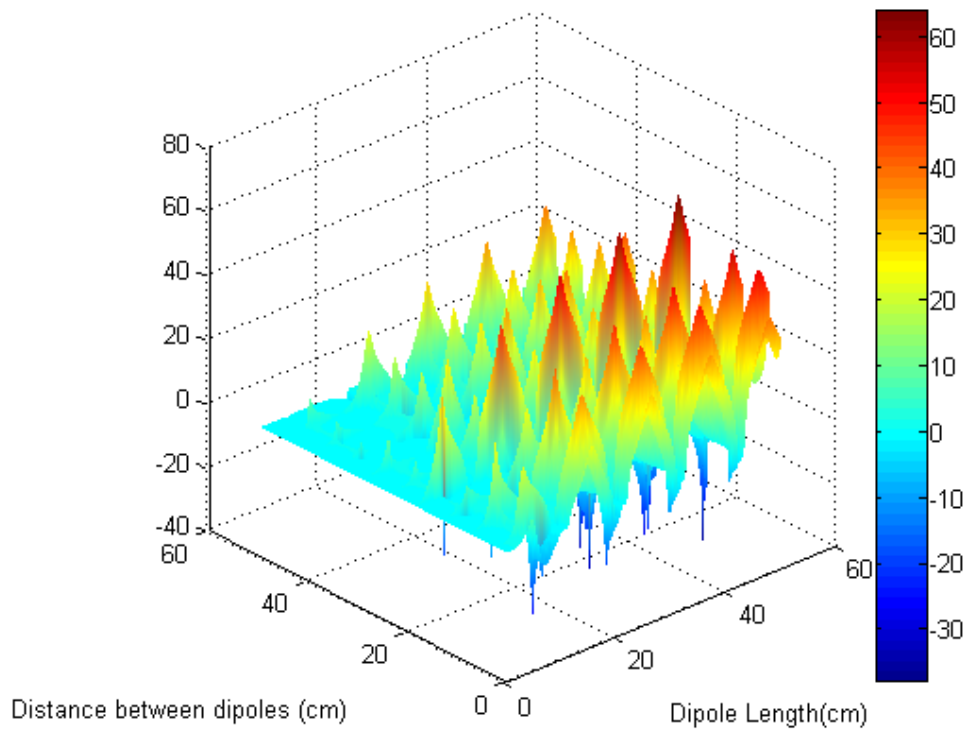


Figure 5.5: Difference between RCS simulation of 2 cylinders with and without multiple scattering (3D view). Notice how the larger differences occur for larger dipoles as the distance decreases between them.

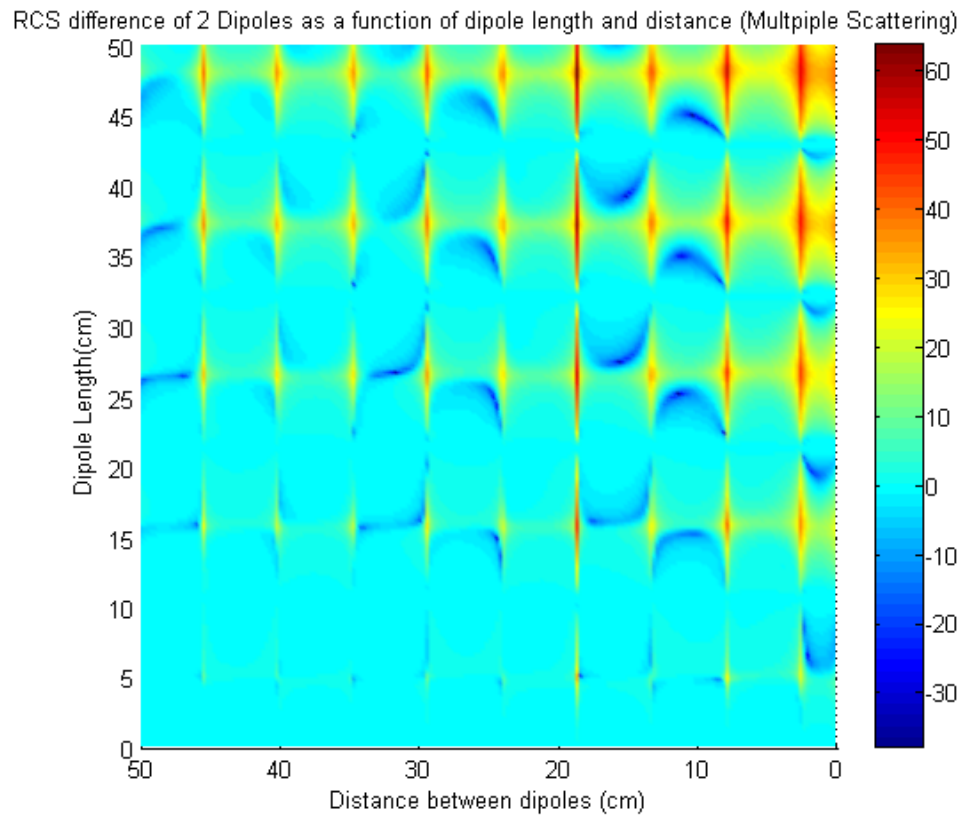


Figure 5.6: Difference between RCS simulation of 2 cylinders with and without multiple scattering (2D view). Same as Figure 5.5 but in 2D for easier viewing.

Figures 5.1 and 5.2 show the effects on the RCS of two cylinders as a function of cylinder length and distance from one another without adding the effects of multiple scattering. The figures show that the RCS on average increases as the length of the cylinders increase as it would be expected from any target. The nulls that appear as the cylinder changes in length is due to the fact that dipole, the object simulating the cylinder, resonates at every  $\lambda/2$  and has its poorest resonance at every  $\lambda$ . The RCS, however, does not increase or decrease overall as a function of distance between the cylinders due to the fact that the RCS has been previously shown to be independent of distance. The nulls and peaks, however, are a result of constructive and destructive interference every time the dipoles reach a distance of  $\lambda/4$  and  $\lambda/2$ .

The same setup is simulated with multiple scattering taken into account and is shown in Figures 5.3 and 5.4. With multiple scattering, the RCS still increases with increasing length but the RCS is higher than the no multiple scattering model when the cylinders are larger than 25 cm and close together. This means that the contribution from multiple scattering increases the overall RCS of the two cylinders. Also worth noting is that the distance between the dipoles now has an impact in the RCS. The closer the dipoles are the higher the RCS. This is true since the scattered field from each cylinder would be higher at closer distances, inducing a larger current on each other.

And finally, the difference between the no multiple scattering added and multiple scattering simulations are plotted in Figures 5.5 and 5.6. Here it is shown where the effects of multiple scattering affect the results the most. As expected, the difference is largest when the cylinder are the longest and closest to each other and is negligible the smaller and farther apart they are. A simple simulation is presented of two aligned dipoles placed 50 cm apart. To compare the result obtained from the MATLAB simulation, a FEKO simulation of the same configuration is plotted.

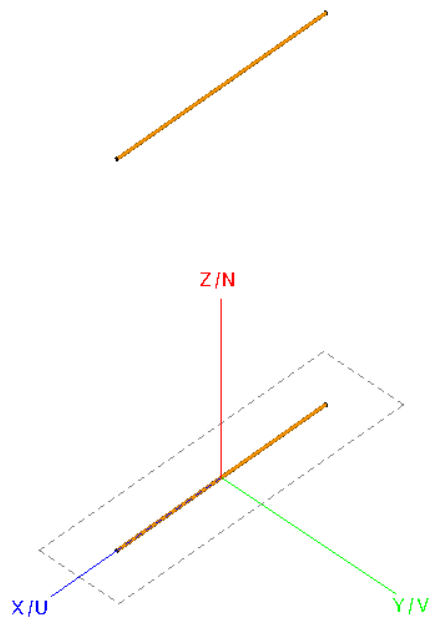


Figure 5.7: Placement of simulated dipoles in a global coordinate system. The first dipole is placed at the origin while the second dipole is placed 50 cm away in the positive  $z$  axis.

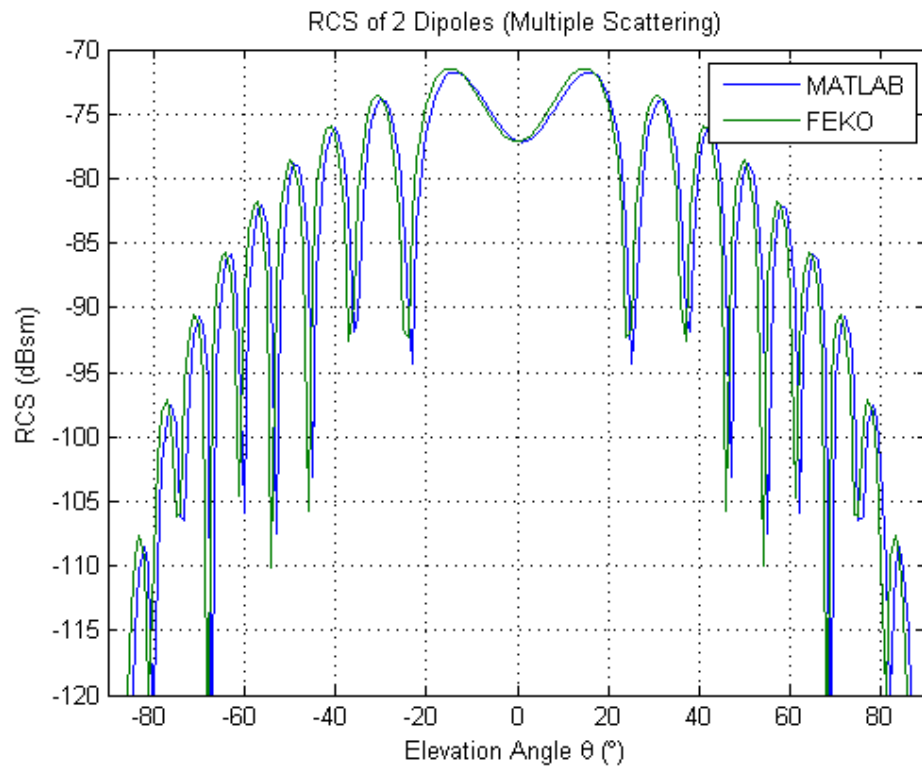


Figure 5.8: MATLAB and FEKO Scattering simulations from 2 dipoles placed 50 cm apart. The agreement between both simulations is excellent, meaning that the MATLAB model is functional and accurate.

The results agree very well between the MATLAB and FEKO simulations for the simple case, confirming that the procedure for calculating the currents is working as seen in Figure 5.8. The patterns are almost exactly the same except for a small shift in angle creating high confidence in the analytical model for multiple scattering for cylinders.

A more complex configuration is simulated to confirm that the multiple scattering simulation in MATLAB is working as intended, where two cylinders are arbitrarily rotated and positioned in space. Both FEKO and MATLAB simulations

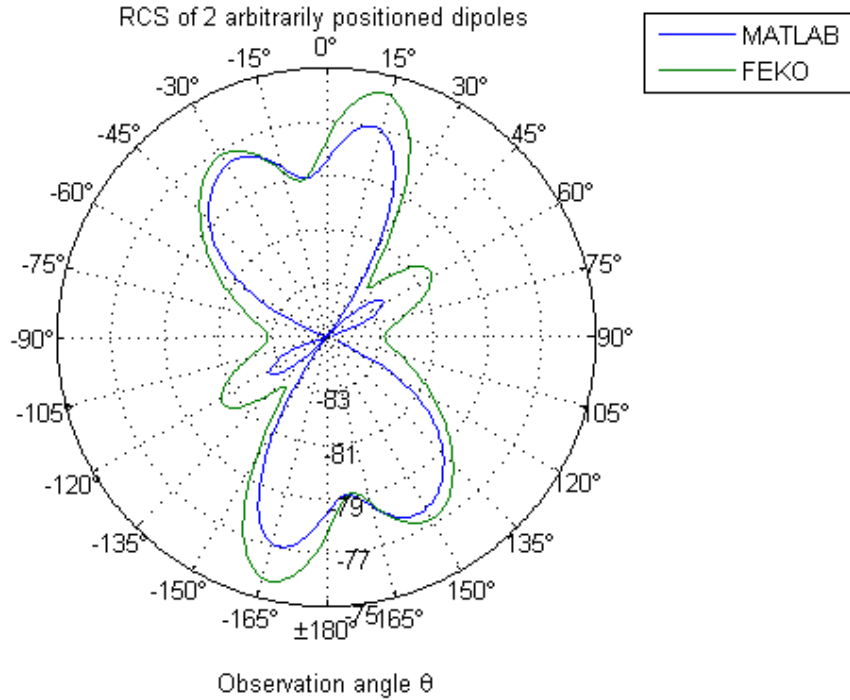


Figure 5.9: MATLAB and FEKO Scattering simulations from 2 arbitrarily rotated and placed dipoles. There is good agreement at the larger lobes and large discrepancies around the nulls.

agree with the exception of the nulls at the 90 and -90 degree mark. The pattern's several peaks have the same magnitude and occur at the same observation angle,

making this a very agreeable result that the multiple scattering model does indeed work. Even though the RCS of two small dipoles is very small, having larger and more cylinders simulated may contribute to a more significant RCS.

The MATLAB script used for calculating the multiple scattering can be used for any number of dipoles that is computationally feasible. In this case the largest number of dipoles simulated has been 500. But the larger the number of cylinders the longer the simulation takes and more memory it will use.

### **5.3 Plate Multiple Scattering**

Multiple scattering by small cylinders has been analyzed in the previous section. In this section multiple scattering by plates is explored. To calculate the multiple scattering due to plates the PO approximation is used to calculate the scattered fields which simplifies the problem and makes it possible to obtain an analytical solution. The PO is most accurate for flat surfaces and using it for this analysis is a good fit [32].

The approach here is similar to the one used with the cylinders, where the scattered fields are calculated individually for each target from the incident wave and the first order multiple scattering contribution from each plate is added to the total scattered field. The scattering created by the plates is done by using equations (2.47) and (2.48) for PEC plates and equations (3.12) and (3.13) for dielectric plates.

To observe the effects of multiple scattering on plates, a dihedral target is simulated. A dihedral is chosen due to its strong return dominated by multiple reflections when looking into the structure at a certain angle [33].



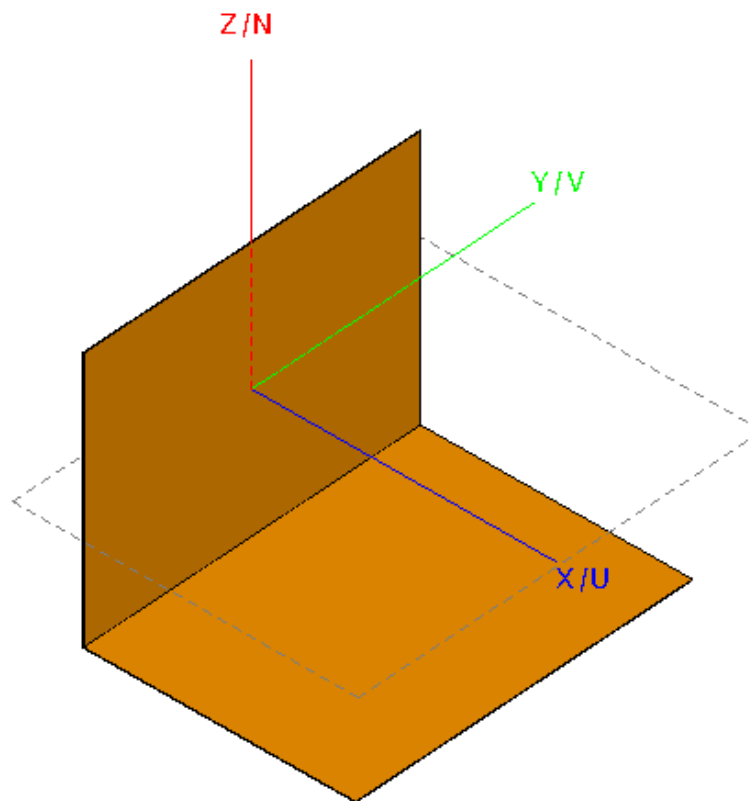


Figure 5.10: Geometry of the simulated dihedral reflector. The first plate is placed on the origin and rotated 90 degrees while the second plate is placed 3 cm along the positive  $x$  axis and 3 cm along the negative  $z$  axis without rotating the plate.

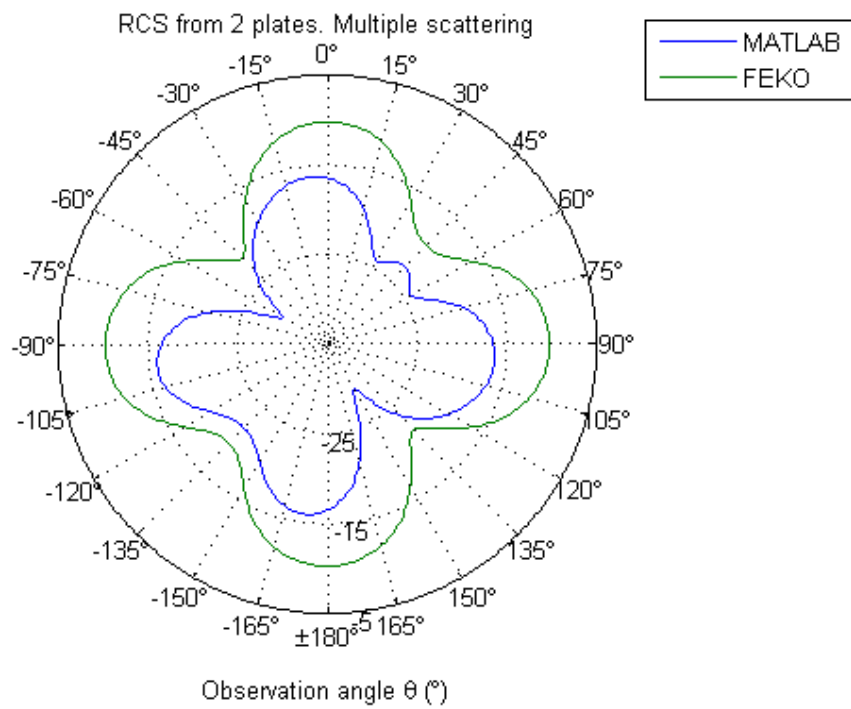


Figure 5.11: RCS pattern for the dihedral simulated in MATLAB and FEKO using PO. The FEKO simulation using PO failed to capture the multiple scattering.

The simulation was carried out in MATLAB and in FEKO for comparison and validation. In FEKO the PO solving scheme was selected to make a direct comparison. However, as seen in Figure 5.11 there is no evidence of multiple scattering as there are the patterns do not resemble results in [34] that use the PO approximation on dihedrals. Literature suggests that FEKO's PO solution should use multiple scattering in the simulation [35] but that is not the case here. The default MoM scheme was selected in FEKO to obtain the true result from the dihedral scattering.

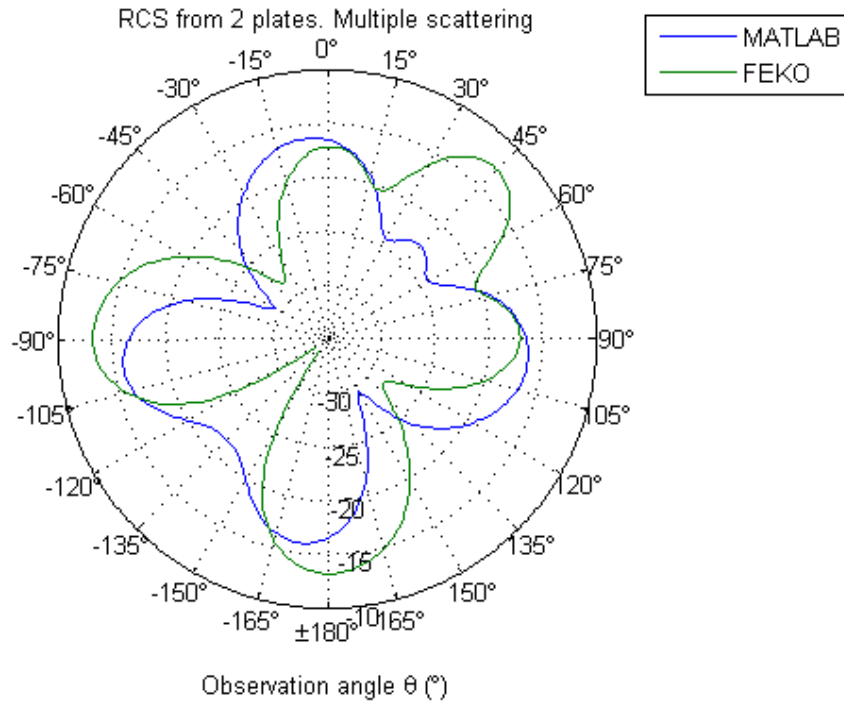


Figure 5.12: RCS pattern for the dihedral simulated in MATLAB and FEKO using MoM. Here FEKO did capture the multiple scattering effect while the MATLAB result does not match it well. A small lobe is seen at 45 degrees but the magnitude is too low.

A peak in RCS looking into the dihedral shows that multiple scattering is taken into effect using the MoM solution. Comparing the MoM FEKO and MATLAB simulations shows that the MATLAB simulation does not match the FEKO simula-

tion. The PO approximation is best used in the far-field and the plates making up the dihedral are close such that near-field and diffraction effects need to be taken into account. This renders the MATLAB simulation very inaccurate. To create a more accurate result, the plates are separated enough so that they are in the far-field region from each other.

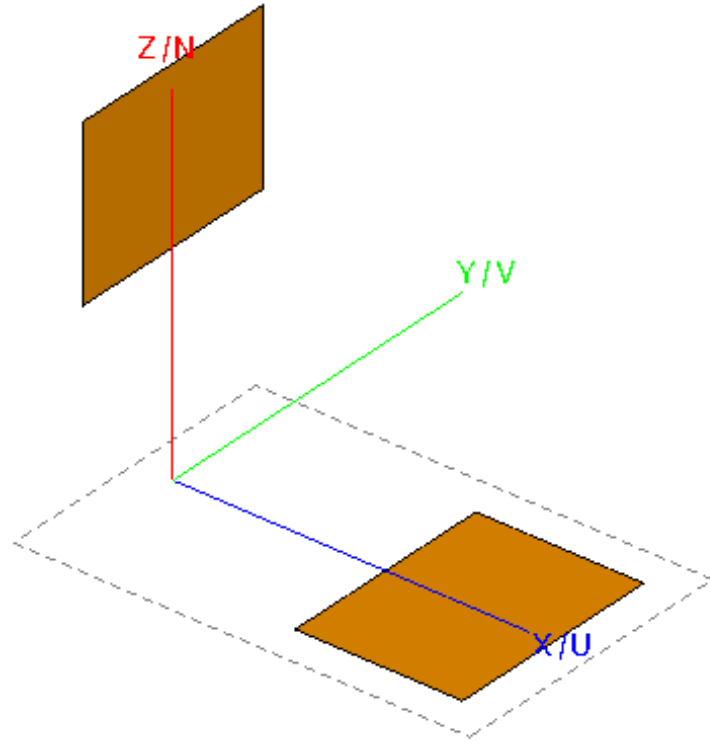


Figure 5.13: Geometry of the simulated separated dihedral reflector. The first plate is rotated 90 degrees and placed 10 cm along the positive  $z$  axis. The second plate is not rotated and placed 10 cm along the positive  $x$  axis.

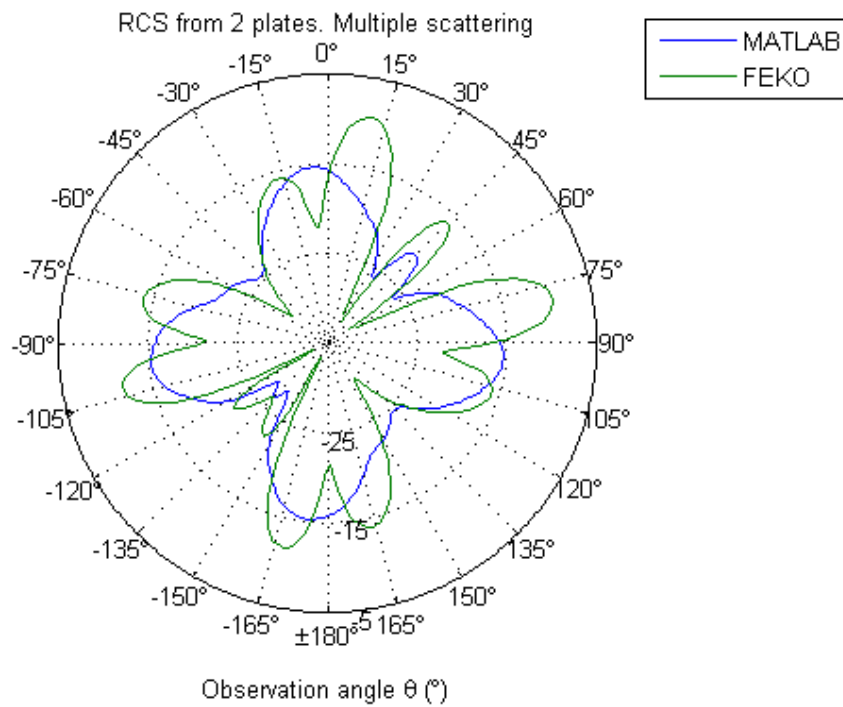


Figure 5.14: RCS pattern for the separated dihedral simulated in MATLAB. The peak at 45 degrees agrees better than in Figure 5.12 but some discrepancies can still be seen especially around the nulls.

The previous plot shows better agreement, especially for the peak at  $45^\circ$  where multiple scattering is strongest. The lobes around this peak are also very similar in magnitude between the simulations, but the shape in general is still a bit off. It is possible that diffraction effects are playing a roll in the scattering in the dihedral and the PO would not take this into account unless explicitly added. The results from the separated dihedral structure agree better than for the normal dihedral structure, so it may be safe to say that near fields affect the results considerably if the plates are too close to each other. This means that if the multiple scattering of debris needs to be modeled accurately a restriction on the distance between debris needs to be enacted so that they all end up on each other's far-field.

## 5.4 Conclusion

An analytical solution for the multiple scattering of cylinders and plates was presented. The reaction concept, reciprocity theorem, and an application of a Thevenin equivalency is used to calculate the induced current in a dipole and subsequently obtaining the scattered fields. A FEKO simulation is used to compare the analytical solution and agree very well. The analytical solution is a powerful tool since populating an electromagnetic solver with many targets is unfeasible and time consuming.

The multiple scattering between the cylinders was studied by plotting it as a function of length and distance between two dipoles. It was observed that without multiple scattering, the distance between dipoles had no effect on the overall RCS and an increasing length of dipoles creates a larger RCS as expected. But with multiple scattering enabled, it was seen that the overall RCS did in fact depend on the distance between dipoles. This is especially true for larger dipoles as the overall

RCS increased for larger dipoles as they were brought closer together.

By using the PO approximation on plates and finding the contributions due to reflections, an analytical method for calculating the multiple scattering from plates was created. The simulation of the dihedral did not agree very well with the analytical method except when the plates were separated enough. This may be due to near-field interaction and possibly diffraction contributions. Nevertheless, contribution from the multiple scattering was indeed seen in the analytical model, providing a good start towards achieving an accurate model for the multiple scattering for plates.

## **Chapter 6**

### **Conclusion**

The RCS of several targets thought to be common tornadic debris has been characterized. By using electromagnetic solvers, the RCS of a leaf and several wooden targets are turned into usable files so that the tornado simulator has access to a small RCS library that will produce accurate RCS information. Measurements of the wooden targets in an anechoic chamber confirm that the simulations are accurate even though the smaller targets suffered from lack of sensitivity in the chamber and produced less accurate measurements.

Multiple scattering using cylinders and plates using analytical solutions was presented with the intention of determining if it is necessary to implement in the tornado simulator for more accurate simulations. The multiple scattering by the small cylinders was implemented by using the reciprocity theorem in MATLAB and shown to make a difference in the scattering of two cylinders, provided that the dipoles are large and close together. The scattering of the cylinders however was limited to small cylinders that generate extremely low RCS. It did serve, however, to establish a framework for the analytical solution for multiple scattering by simple shapes. It also provides a faster way to compute multiple scattering since drawing each individual target in an electromagnetic solver is time consuming and if too many targets are used the solver may not be able to simulate it due to running out



of memory.

Using this framework, the analytical solution for the multiple scattering of plates was produced. By using the PO approximation, the scattering for the plates is calculated and first order multiple scattering was achieved. A dihedral target made of two plates was used to confirm the multiple scattering due to the target's RCS being dominated by multiple scattering between its sides.

Even though multiple scattering was introduced, a polarimetric analysis has yet to be done to verify whether multiple scattering is an important and dominating factor in the polarimetric products of a radar. As a best guess the multiple scattering will have an effect on the radar return signal provided that the debris pieces are large enough and close enough to each other, suggesting that multiple scattering will have a larger probability of having an impact when the tornado is loaded with a larger amount of debris.

## References

- [1] R. J. Doviak and D. S. Zrnic, *Doppler Radar and Weather Observations*. Dover Publications Inc., 2006.
- [2] R. E. Rinehart, *Radar for Meteorologists*. Rinehart Publications, 2005.
- [3] V. N. Bringi and V. Chandrasekar, *Polarimetric Doppler Weather Radar*. Cambridge University Press, 2001.
- [4] G. Zhang, *Weather Radar Polarimetry with MATLAB*. Taylor & Francis, 2016.
- [5] D. J. Bodine, R. D. Palmer, and G. Zhang, “Dual-Wavelength Polarimetric Radar Analyses of Tornadoic Debris Signature”, *Journal of Applied Meteorology and Climatology*, vol. 53, pp. 242–261, 2014.
- [6] B. L. Cheong, D. J. Bodine, C. J. Fulton, S. M. Torres, T. Maruyama, and R. D. Palmer, “Simradar: A Polarimetric Radar Time-Series Simulator for Tornadoic Debris Studies”, *IEEE Trans. Geosci. and Remote Sens.* *accepted*,
- [7] T. B. A. Senior, K. Sarabandi, and F. T. Ulaby, “Measuring and Modeling the Backscattering Cross Section of a Leaf”, *Radio Science*, vol. 22, no. 6, pp. 1109–1116, 1987.
- [8] F. T. Ulaby and R. Jedlicka, “Microwave Dielectric Properties of Plant Materials”, *IEEE Transactions on Geoscience and Remote Sensing*, no. 4, pp. 406–415, 1984.
- [9] L. R. Lemon, “The Radar ”Three-Body Scatter Spike”: An Operational Large-Hail Signature”, *Weather and Forecasting*, vol. 13, no. 2, pp. 327–340, 1998.
- [10] *NEXRAD technical information*, 1998. [Online]. Available: <https://www.roc.noaa.gov/wsr88d/Engineering/NEXRADTechInfo.aspx>.

- [11] E. F. Knott, J. F. Shaeffer, and M. T. Tuley, *Radar Cross Section*. SciTech Publishing, 2004.
- [12] D. C. Jenn, *Radar and Laser Cross Section Engineering*. American Institution of Aeronautics and Astronautics, Inc., 2005.
- [13] C. A. Balanis, *Advanced Engineering Electromagnetic*. John Wiley & sons, Inc., 2012.
- [14] J. W. Crispin and K. M. Siegel, *Methods of Radar Cross-Section Analysis*. Academic Press Inc., 1968.
- [15] J. W. Crispin and A. L. Maffett, “Radar Cross-Section Estimation for Simple Shapes”, *Proceedings of the IEEE*, vol. 53, no. 8, pp. 833–848, 1965.
- [16] S. Stavrou and S. Saunders, “Review of Constitutive Parameters of Building Materials”, in *Antennas and Propagation, 2003.(ICAP 2003). Twelfth International Conference on (Conf. Publ. No. 491)*, IET, vol. 1, 2003, pp. 211–215.
- [17] *RCS of a sphere*, 2009. [Online]. Available: [https://commons.wikimedia.org/wiki/File:Radar\\_cross\\_section\\_of\\_metal\\_sphere\\_from\\_Mie\\_theory.svg](https://commons.wikimedia.org/wiki/File:Radar_cross_section_of_metal_sphere_from_Mie_theory.svg).
- [18] L. Rayleigh, “On the Incidence of Aerial and Electromagnetic Waves Upon Small Obstacles in the Form of Ellipsoids or Elliptic Cylinders, and on the Passage of Electric Waves Through a Circular Aperture in a Conducting Screen”, *Phil. Mag.*, vol. 44, 1897.
- [19] J. R. Wait, “Scattering of a Plane Wave from a Circular Dielectric Cylinder at Oblique Incidence”, *Canadian Journal of Physics*, vol. 33, no. 5, pp. 189–195, 1955.
- [20] *User manual/working with CADFEKO*, Altair Engineering Inc., 2014.
- [21] R. Olmi, M. Bini, A. Ignesti, and C. Riminesi, “Dielectric Properties of Wood from 2 to 3 GHz”, *Journal of Microwave Power and Electromagnetic Energy*, vol. 35, no. 3, pp. 135–143, 2000.
- [22] *HFSS getting starting guides/radar cross section (RCS) model*, HFSS, 2015.

- [23] R. B. Dybdal, "Radar Cross Section Measurements", *Proceedings of the IEEE*, vol. 75, no. 4, pp. 498–516, 1987.
- [24] C.-F. Hu, J.-D. Xu, N. Li, and L.-X. Zhang, "Indoor Accurate RCS Measurement Technique on UHF Band", *Progress In Electromagnetics Research*, vol. 81, pp. 279–289, 2008.
- [25] *Understanding and improving network analyzer dynamic range*, Agilent Technologies, 2002.
- [26] R. F. Harrington, "Theory of Loaded Scatterers", *Electrical Engineers, Proceedings of the Institution of*, vol. 111, no. 4, pp. 617–623, 1964.
- [27] R. Hansen, "Relationships Between Antennas as Scatterers and as Radiators", *Proceedings of the IEEE*, vol. 77, no. 5, pp. 659–662, 1989.
- [28] C. A. Balanis, *Antenna Theory Analysis and Design*. John Wiley & Sons, Inc., 2005.
- [29] R. F. Harrington, "Small Resonant Scatterers and Their Use for Field Measurements", *IRE Transactions on Microwave Theory and Techniques*, vol. 10, no. 3, pp. 165–174, 1962.
- [30] V. Rumsey, "Reaction concept in Electromagnetic Theory", *Physical Review*, vol. 94, no. 6, p. 1483, 1954.
- [31] Warnic and Jensen, *Receive Antennas*, 2015. [Online]. Available: <https://ecen665web.groups.et.byu.net/notes/ln3.pdf>.
- [32] E. F. Knott, "A Progression of High-Frequency RCS Prediction Techniques", *Proceedings of the IEEE*, vol. 73, no. 2, pp. 252–264, 1985.
- [33] J. A. Jackson, "Analytic Physical Optics Solution for Bistatic, 3D Scattering from a Dihedral Corner Reflector", *IEEE Transactions on Antennas and Propagation*, vol. 60, no. 3, pp. 1486–1495, 2012.
- [34] T. Griesser and C. A. Balanis, "Backscatter Analysis of Dihedral Corner Reflectors Using Physical Optics and the Physical Theory of Diffraction", *IEEE Transactions on Antennas and Propagation*, vol. 35, no. 10, pp. 1137–1147, 1987.

- [35] D. P. Xiang and M. M. Botha, “Acceleration of Multiple Reflection Physical Optics Scattering Analysis with the MLFMM”, in *2016 10th European Conference on Antennas and Propagation (EuCAP)*, IEEE, 2016, pp. 1–3.
- [36] D. J. Bodine, M. R. Kumjian, R. D. Palmer, P. L. Heinselman, and A. V. Ryzhkov, “Tornado Damage Estimation Using Polarimetric Radar”, *Weather and Forecasting*, vol. 28, no. 1, pp. 139–158, 2013.

## Appendix A

### Derivations

#### A.1 Equivalence of Transmit and Receive Antennas

The reciprocity theorem was invoked in chapter 5 alongside a Thevenin equivalent to solve for the open-circuit voltage of a dipole to be used as a scatterer. The entire derivation of the open-circuit voltage is provided by [31] and is as follows.

Invoking the reaction concept shown in chapter 5(5.3) the current filament  $\mathbf{J}_a$  is aligned with the z-axis so that the reaction between  $\mathbf{J}_a$  and  $\mathbf{E}_b$  is

$$\langle \mathbf{J}_a, \mathbf{E}_b \rangle = \int \mathbf{J}_a(\mathbf{r}) \cdot \mathbf{E}_b(\mathbf{r}) d\mathbf{r}. \quad (\text{A.1})$$

$$= \int [-I_a \hat{z} \delta(x) \delta(y)] \cdot \mathbf{E}_b(\mathbf{r}) d\mathbf{r}. \quad (\text{A.2})$$

$$= -I_a \int_{z_1}^{z_2} \hat{z} \cdot \mathbf{E}_b(\mathbf{r}) dz. \quad (\text{A.3})$$

$$= -I_a \int_{z_1}^{z_2} \mathbf{E}_b(\mathbf{r}) \cdot d\mathbf{l}. \quad (\text{A.4})$$

$$= I_a V_{oc}(a). \quad (\text{A.5})$$

Where  $V_{oc}(a)$  is the open circuit voltage induced across the antenna  $a$ . Similarly for antenna  $b$  the reaction is

$$\langle \mathbf{J}_b, \mathbf{E}_a \rangle = I_b V_{oc}(b). \quad (\text{A.6})$$

Using the reciprocity theorem

$$I_a V_{oc}(a) = I_b V_{oc}(b). \quad (\text{A.7})$$

Proving that the pattern for a receiving and transmitting antenna are equal.

To solve for the open-circuit voltage on a receiving antenna a Thevenin equiva-

lent is used

$$V_{oc}(a) = \frac{1}{I_0} \int \mathbf{J}_b \cdot \mathbf{E}_a. \quad (\text{A.8})$$

the reciprocity theorem is applied to a third configuration

$$\mathbf{J}_a = \mathbf{J}_0 + \mathbf{J}_{a,eq} \quad (\text{A.9})$$

where  $\mathbf{J}_{a,eq}$  is the equivalent current for antenna a with the excitation  $\mathbf{J}_0$ . The reciprocity theorem requires that

$$\int \mathbf{J}_b \cdot \mathbf{E}_a d\mathbf{r} = \int (\mathbf{J}_0 + \mathbf{J}_{a,eq}) \cdot \mathbf{E}_b d\mathbf{r} \quad (\text{A.10})$$

where  $\mathbf{E}_b$  is the radiated field by the antenna  $b$  without antenna  $a$  present. Combining all the previous equations results in

$$V_{oc}(a) = \frac{1}{I_0} \int (\mathbf{J}_0 + \mathbf{J}_{a,eq}) \cdot \mathbf{E}_b d\mathbf{r} \quad (\text{A.11})$$

For an antenna with a small gap between the terminals, the above equation reduces to

$$V_{oc} = \frac{1}{I_0} \int \mathbf{J}_{eq} \cdot \mathbf{E}_{inc} d\mathbf{r} \quad (\text{A.12})$$

by ignoring the contribution from  $J_0$ . To solve for the open circuit voltage, the incident wave is assumed to be a plane wave

$$\mathbf{E}^{inc} = \hat{p} E_{inc} e^{-j\beta^{inc} \cdot \mathbf{r}} \quad (\text{A.13})$$

so that

$$V_{oc}(a) = \frac{1}{I_0} \int \mathbf{J}_{eq} \cdot \hat{p} E_{inc} e^{-j\beta^{inc} \cdot \mathbf{r}} d\mathbf{r} \quad (\text{A.14})$$

Equation (A.14) is very similar to the radiation integral

$$\mathbf{E}(\mathbf{r}) = -j\omega\mu(1 - \hat{r}\hat{r} \cdot) \frac{e^{-j\beta r}}{4\pi r} \int \mathbf{J}_{eq} \cdot \hat{p} E_{inc} e^{-j\beta^{inc} \cdot \mathbf{r}} d\mathbf{r} \quad (\text{A.15})$$

Equations (A.14) and (A.15) are related by

$$(1 - \hat{r}\hat{r} \cdot) \int \mathbf{J}_{eq}(\mathbf{r}') e^{-j\beta \hat{r} \cdot \mathbf{r}'} d\mathbf{r}' \quad (\text{A.16})$$

and can be shown that

$$\hat{p} \cdot (1 - \hat{k}^{inc} \hat{k}^{inc}) \int \mathbf{J}_{eq}(\mathbf{r}) e^{-j\boldsymbol{\beta}^{inc} \cdot \mathbf{r}} d\mathbf{r} = \int \hat{p} \mathbf{J}_{eq}(\mathbf{r}) e^{-j\boldsymbol{\beta}^{inc} \cdot \mathbf{r}} d\mathbf{r} \quad (\text{A.17})$$

Using this result to combine equations (A.14) and (A.15) leads to the usable form of the open circuit voltage equation

$$V_{oc} = \hat{p} \frac{1}{I_0} \frac{4\pi j r e^{j\beta r}}{\omega \mu} E^{inc} \cdot \mathbf{E}^t(\mathbf{r}) \quad (\text{A.18})$$



## Appendix B

### Code

#### B.1 Leaf RCS

Main program and dielectric sheet and cylinder functions

Listing B.1: Leaf RCS calculation main script

```
for m = 1:numel(Alpha)
    for n = 1:numel(Beta)
        num = num+1;
        alpha = m*pi/180;
        beta = n*pi/180;
        [Sx, Ssheet, Scyl, dB_sheet, dB_cyl, ang_sheet,
         ang_cyl] = dielectric_sheet_rcs(2);
        offset = zr_hat(2)*(cl-lh)/2;
        S_cyl = S_cyl*exp(1i*2*k*offset);
        S_leaf(m,n,,:) = S_cyl + S_sheet;
        r_hat(m,n,:) = zr_hat;
    end
end
\newpage

Functions to compute the RCS of the dielectric sheet and
dielectric cylinder
\begin{lstlisting}[frame=single, caption=Dielectric sheet
RCS]

% Define transformation matrix between coordinate systems
.
% A vector p in the RADAR coordinate system is equal to
% P = Tp in the LOCAL coordinate system
ca = cos(alpha); cb = cos(beta); cg = cos(gamma);
sa = sin(alpha); sb = sin(beta); sg = sin(gamma);
T = [ ca*cb*cg-sa*sg ca*cb*sg+sa*cg -ca*sb; ... %
      transformation matrix changed so that we have z-y'-z''
```

```

-sa*cb*cg-ca*sg -sa*cb*sg+ca*cg sa*sb; ...
sb*cg          sb*sg          cb          ];

% Unit vectors for plotting the RADAR axes in the LOCAL
coordinate system:
u_hat = T*[1 0 0; ...
          0 1 0; ...
          0 0 1];
xr_hat = u_hat(:,1);
yr_hat = u_hat(:,2);
zr_hat = u_hat(:,3);
% Radar sits at z = R0, y = 0, x = 0, or at an angle in
the radar coordinate
% system of R = R0, theta = 0, phi = 0.
% In the Local system, the radar is at an angular
location that is in line
% with zr_hat, so that according to the target the angle
of incidence is
Theta0 = acos(zr_hat(2))*180/pi; %With respect to the
radar (y component of zr_hat)
Phi0 = atan2(zr_hat(1), zr_hat(3))*180/pi; %With respect
to the radar (x component of zr_hat, z component of
zr_hat)
% ***IMPORTANT NOTE***
% Here, Theta0 = angle from y axis in local coordinate
system and
% Phi0 = angle from z axis along z-y plane. These are NOT
the "normal"
% spherical coordinates. This is done to make the
calculations more simple
% for the sheet and cylinder below
%%%%%%%%%%%%%%
%% Sheet RCS %%
%%%%%%%%%%%%%%
% The angle of incidence from normal (with zero degrees
corresponding to the +Y half of the sphere) is:
ThetaNorm = acos(zr_hat(3))*180/pi; %Like phi in "normal"
spherical coordinates
Theta0S = acos(abs(zr_hat(3)))*180/pi; %(for sarabandi
paper we need just absolute angle from x axis
% The rotation angle can be found by projecting the
zr_hat vector onto
% the X-Y plane in the LOCAL coordinate system; what
results is that
% the counter-clockwise rotation angle of the sheet

```

```

    relative to the
% nominal problem setup that's been solved and
    demonstrated by Ye
% (based on the Sarabandi paper) is:
%   PhiRot = atan2(xr_hat(2), xr_hat(3))*180/pi*sign(
    xr_hat(1));

% The unit vector corresponding to the plane of incidence
    as seen on the X-Y plane is

Denom = sqrt(zr_hat(1)^2+zr_hat(2)^2);
zt_hat(3) = 0;
if Denom == 0
    zt_hat(1) = -1; % deals with a singularity condition
    zt_hat(2) = 0;
else
    zt_hat(1) = zr_hat(1)./Denom; %Vector magnitude junk
        here
    zt_hat(2) = zr_hat(2)./Denom;
end
% The unit vector in the direction of the parallel E
    field vector for the
% equivalent rotated sheet problem is:
tm_hat = -zt_hat*cos(ThetaNorm*pi/180) + [0 0 1]*sin(
    ThetaNorm*pi/180);

% The unit vector in the direction of the perpendicular E
    field vector for the
% equivalent rotated sheet problem is:
te_hat = cross(zr_hat, tm_hat);
% Note: The angle of incidence for either polarization is
    Theta0S from above
% Resistivity
R = -1i*Z0/(k*tau*(er-1)); % negative because of e^jwt
    convention
% Material properties
% Perpendicular reflection coefficient -- appears to be
    reasonable
gammaE = 1./(1+(2*R/Z0)*cos(Theta0S*pi/180)); % using
    same negative sign convention as Sarabandi
% Parallel reflection coefficient -- appears to be
    reasonable
gammaH = 1./(1+(2*R/Z0)*sec(Theta0S*pi/180));

%Width and length projected onto radar coordinate system

```

```

    from original
Zw = k*lh*cos(Theta0*pi/180);           %just changed the
    variable name from Xw to Zw
Zl = k*lw*sin(Theta0*pi/180)*sin(Phi0*pi/180); %same
    thing, from Xl to Zl
% "Tilted" circle: ellipse
% Note: sin(phi) here because unlike sarabandi's paper (x
    = 0) we have leaf at x = 0

Sx = 1i/(2*pi)*k^2*lh*lw*cos(Theta0S*pi/180)*sinc(Zw/pi)*
    sinc(Zl/pi); %Radar cross section for the rectangular
    sheet (probably scattering but could be power density)

% Remember: Theta0S is from the z-axis in the yz plane
    and Phi0S is
% from the
% "far-field amplitude" in sarabandi paper
%   Se = -gammaE*S; % perpendicular
%   Sh = -gammaH*S; % parallel
Se = -lambda/sqrt(pi)*gammaE*Sx; % perpendicular RCS (
    complex amp)
Sh = -lambda/sqrt(pi)*gammaH*Sx; % parallel RCS (complex
    amp)

%RCS for circular sheets may just replace Sx with Sxc

% Note: negative sign here fixes a sign problem in the
    paper

%Sec =      % perpendicular RCS (complex amp)
%Seh =      % parallel RCS (complex amp)

% The two incident unit vectors are xr_hat for H and
    yr_hat for V.
% The projection matrix from this basis to the Te (perp)
    / Tm (parallel) basis is:
%   [Te] = [A B][H] = TP * [H]
%   [Tm] = [C D][V]   [V]
TP = [te_hat*xr_hat te_hat*yr_hat; tm_hat*xr_hat tm_hat*
    yr_hat]; %changed, as now xr_hat is H-pol and yr_hat
    is V-pol
%   [Shh; Shv] = TP^(-1)*diag([RCSe RCSh])*TP*[1;0]
%   [Svh; SvV] = TP^(-1)*diag([RCSe RCSh])*TP*[0;1]

S_sheet = TP^(-1)*diag([Se Sh])*TP;

```

```

% [Se Sh] = cylinder_rcs(cd/2, cl, f, Theta0*pi/180);
[Se Sh] = dielectric_cylinder_rcs(cd/2, cl, er, f, Theta0
    *pi/180); %Changes Se and Sh for cylinder measurements
% ***IMPORTANT REMINDER***
% Here, Theta0 = angle from y axis in local coordinate
    system and
% Phi0 = angle from z axis along z-y plane. These are NOT
    the "normal"
% spherical coordinates.
Theta0_hat = [cos(Theta0*pi/180)*sin(Phi0*pi/180) -sin(
    Theta0*pi/180) cos(Theta0*pi/180)*cos(Phi0*pi/180)];
Phi0_hat = [cos(Phi0*pi/180) 0 -sin(Phi0*pi/180)];
TC = [Phi0_hat*xr_hat Phi0_hat*yr_hat; Theta0_hat*xr_hat
    Theta0_hat*yr_hat];
S_cyl = TC^(-1)*diag([Se Sh])*TC;

dB_sheet = 20*log10(abs(S_sheet([1 4])));
dB_cyl = 20*log10(abs(S_cyl([1 4])));
ang_sheet = 180/pi*angle(S_sheet([1 4]));
ang_cyl = 180/pi*angle(S_cyl([1 4]));
Ssheet = S_sheet([1 4]);
Scyl = S_cyl([1 4]);

```

### Listing B.2: Dielectric cylinder RCS

```

% compute the scattered fields for TM and TE incidence
for n = -nmode:nmode

    % derivatives of Bessel function
    jn_d = n*besselj(n,u)/(u) - besselj(n+1,u);

    % derivatives of Hankel function
    hn_d = 1.0/2*(besselh(n-1,2,v)-besselh(n+1,2,v));

    D_TM = (hn_d./(v.*besselh(n,2,v))-K_tm*jn_d./(u.*besselj(n
        ,u)))...
       .*(hn_d./(v.*besselh(n,2,v))-N^2/K_tm*jn_d./(u.*besselj
            (n,u)))...
        -(1./v.^2-1./u.^2).^2*n^2.*cti.^2;

    D_TE = (hn_d./(v.*besselh(n,2,v))-K_te*jn_d./(u.*besselj(n
        ,u)))...
       .*(hn_d./(v.*besselh(n,2,v))-N^2/K_te*jn_d./(u.*besselj
            (n,u)))...

```

```

        -(1./v.^2-1./u.^2).^2*n^2.*cti.^2;

% This is an_s/(E0sin(theta))
an_spp_TM = 1j^n.*(-besselj(n,v)./besselh(n,2,v)...
-2.*1j.*(hn_d./(v.*besselh(n,2,v))-K_tm*jn_d./(u.*besselj(
    n,u)))...
./ (pi*v.^2.*besselh(n,2,v).^2.*D_TM));

an_spp_TE = 1j^n.*(-besselj(n,v)./besselh(n,2,v)...
-2.*1j.*(hn_d./(v.*besselh(n,2,v))-K_te*jn_d./(u.*besselj(
    n,u)))...
./ (pi*v.^2.*besselh(n,2,v).^2.*D_TE));

% This is bn_s/(E0sin(theta))
bn_spp_TM = (beta2/(u0*omega)).*(1j)^n.*(2./(pi*v.^2)
    .*(1./(u.^2)-1./(v.^2))*n.*cti./(besselh(n,2,v).^2.*
    D_TM)); %added (beta2/(ur_2*omega)) whish was on the
    paper
bn_spp_TE = (beta2/(u0*omega)).*(1j)^n.*(2./(pi*v.^2)
    .*(1./(u.^2)-1./(v.^2))*n.*cti./(besselh(n,2,v).^2.*
    D_TE));

sum_tm_co_pol = sum_tm_co_pol + an_spp_TM*li^n;
sum_tm_cross_pol = sum_tm_cross_pol + bn_spp_TM*li^n;
sum_te_co_pol = sum_te_co_pol + an_spp_TE*li^n;
sum_te_cross_pol = sum_te_cross_pol + bn_spp_TE*li^n;
end

% calculate the RCS for E (perpendicular E) polarization and
    H (parallel E) polarization
Sch = sum_tm_co_pol.*sqrt(4*li*l^2/pi*sti).*sinc(beta2*l*cti
    /pi); %Sch = sum_tm_co_pol.*sqrt(4*l^2/pi*sti).*sinc(
    beta2*l*cti);
Sce = sum_te_co_pol.*sqrt(4*li*l^2/pi*sti).*sinc(beta2*l*cti
    /pi); %Sce = sum_te_co_pol.*sqrt(4*l^2/pi*sti).*sinc(
    beta2*l*cti); %Sce = sum_te_co_pol.*sqrt(4*li*l^2/pi*sti)
    .*sinc(beta2*l*cti/pi);

Sch = Sch*exp(li*pi/4); % This appears to give it the
    correct phase relative to HFSS
Sce = -Sce*exp(li*pi/4);

```

## B.2 Chamber Measurements RCS

The following code is used to plot the measured RCS and the FEKO RCS as well. The parts of the script that are used for the sphere RCS calculations were obtained from the digital content in [13] and modified to fit the needs of this thesis.

Listing B.3: RCS pattern of measured target and target simulated in FEKO

```
for n = 1:101
    frequency = frequency + 0.006e9;
    for k = 1:nTheta
        [eTheta(k,:) a] = mie(radius, frequency, theta(k),
            0.0, nMax);
        [a ePhi(k,:)] = mie(radius, frequency, theta(k), pi/2,
            nMax);
    end

    ePhii(n) = ePhi(end);
    et(n) = (20*log10(abs(eTheta(end))) - 20*log10(abs(eTheta(1))
        ));
    ep(n) = (20*log10(abs(ePhi(end))) - 20*log10(abs(ePhi(1)))));

end
...
I = spherei - nospherei;
Q = sphereq - nosphereq;

S = (I.^2)+(Q.^2);
S = 10*log10(4*pi*S);
S = transpose(mean(S));
cal = s-S;
cal = cal.';
cal = repmat(cal,361,1);
...
I = woodi - nowoodi;
Q = woodq - nowoodq;

s = (I.^2)+(Q.^2);
S = 10*log10(4*pi*s)+cal;
sphere = 10*log10(sqrt(spherei.^2+sphereq.^2));
nosphere = 10*log10(sqrt(nospherei.^2+nosphereq.^2));

[M,I] = max(S(:,34));
y1 = circshift(S(:,34),181-I);
phi = -180:1:180;
```

```

figure(1)
plot(phi,y1,'k')
title(['Measured_RCS_of_11x5.5x0.75_Inch_Wooden_Plank'])
xlim([-180 180])
set(gca,'XTick',-180:45:180)
grid on
ylabel('Radar_Cross_Section_(dBsm)')
xlabel('Azimuth_angle_(Degree)')
dim = [.2 .6 .3 .3];
legend('2.9GHz')
hold off
[M,I] = max(y1)
spheresweep = 'FEKODataSylvesterPine';
A = xlsread(spheresweep);
wood = A(1:end,2);
diff = abs(y1-wood);

```

Listing B.4: Mie series to calculate the RCS of a sphere obtained from [13]

```

% compute spherical bessel, hankel functions
[J(mode)] = besselj(mode + 1/2, k*radius); J = J*s;
[H(mode)] = besselh(mode + 1/2, 2, k*radius); H = H*s;
[J2(mode)] = besselj(mode + 1/2 - 1, k*radius); J2 = J2*s;
[H2(mode)] = besselh(mode + 1/2 - 1, 2, k*radius); H2 = H2*s
;

% derivatives of spherical bessel and hankel functions
% Recurrence relationship, Abramowitz and Stegun Page 361
kaJ1P(mode) = (k*radius*J2 - mode .* J );
kaH1P(mode) = (k*radius*H2 - mode .* H );

% Ruck, et. al. (3.2-1)
An = -((i).^mode) .* ( J ./ H ) .* (2*mode + 1) ./ (mode.*(
mode + 1));

% Ruck, et. al. (3.2-2), using derivatives of bessel
functions
Bn = ((i).^(mode+1)) .* (kaJ1P ./ kaH1P) .* (2*mode + 1) ./
(mode.*(mode + 1));

[esTheta esPhi] = mieScatteredField(An, Bn, theta, phi,
frequency);

return

```



Listing B.5: Scattered fields from the Mie series obtained from [13]

```
% compute coefficients for scattered electric far field
for iMode = 1:length(An)

    % derivative of associated Legendre Polynomial
    if abs(cosTheta) < 0.999999
        if iMode == 1
            dp = cosTheta*plm(1)/sqrt(1.0 - cosTheta*cosTheta);
        else
            dp = (iMode*cosTheta*plm(iMode) - (iMode + 1)*plm(
                iMode - 1))/sqrt(1.0 - cosTheta*cosTheta);
        end
    end

    if abs(sinTheta) > 1.0e-6
        term1 = An(iMode)*p/sinTheta;
        term2 = Bn(iMode)*p/sinTheta;
    end

    if cosTheta > 0.999999
        % Ruck, et. al. (3.1-12)
        val = ((i)^(iMode-1))*(iMode*(iMode+1)/2)*(An(iMode) -
            i*Bn(iMode));
        S1 = S1 + val;
        S2 = S2 + val;
    elseif cosTheta < -0.999999
        % Ruck, et. al. (3.1-14)
        val = ((-i)^(iMode-1))*(iMode*(iMode+1)/2)*(An(iMode)
            + i*Bn(iMode));
        S1 = S1 + val;
        S2 = S2 - val;
    else
        % Ruck, et. al. (3.1-6)
        S1 = S1 + ((i)^(iMode+1))*(term1 - i*Bn(iMode)*dp);
        % Ruck, et. al. (3.1-7)
        S2 = S2 + ((i)^(iMode+1))*(An(iMode)*dp - i*term2);
    end

    % recurrence relationship for next Associated Legendre
    Polynomial
    if iMode > 1
        plm(iMode + 1) = (2.0*iMode + 1)*cosTheta*plm(iMode)/
            iMode - (iMode + 1)*plm(iMode - 1)/iMode;
    end
    p = plm(iMode + 1);
end
```

```

end

% complex-value scattered electric far field, Ruck, et. al.
% (3.1-5)
esTheta = S1*cos(phi);
esPhi = -S2*sin(phi);

% normalize electric field so square of magnitude is RCS in
% square meters
esTheta = esTheta*sqrt(4.0*pi)/k;
esPhi = esPhi*sqrt(4.0*pi)/k;

return

```

### B.3 Cylinder Multiple Scattering

The following script is used to calculate the RCS of cylinders using multiple scattering. It is set to randomly select the position and orientation but it was fixed for the experiments done for this thesis.

Listing B.6: Multiple scattering script for small cylinders

```

for t = 1:length(e1)
    theta_ang_obs = ((t-1)*pi)/180; %Theta observation angle
    sweep (0 to 360)

    for n = 1:sctrs
        ca = cos(alpha(n)); cb = cos(beta(n)); cg = cos(gamma)
        ; %Transformation Matrix stuff
        sa = sin(alpha(n)); sb = sin(beta(n)); sg = sin(gamma)
        ; %
        T = [ca*cb*cg-sa*sg -ca*cb*sg-sa*cg ca*sb; ... %
            sa*cb*cg+ca*sg -sa*cb*sg+ca*cg sa*sb; ... %
            -sb*cg sb*sg cb ]; %

        u_hat = T*[1 0 0; ... %Rotated Unit Vectors
                    0 1 0; ... %
                    0 0 1]; %
        xr_hat = u_hat(:,1); %X' Unit Vector
        yr_hat = u_hat(:,2); %Y' Unit Vector
        zr_hat = u_hat(:,3); %Z' Unit Vector
        K_hat = [-sin(theta_ang_obs) 0 -cos(theta_ang_obs)]; %
        % incident wave unit vector
        dotx = dot(-K_hat,xr_hat); %K and X' dot product
        doty = dot(-K_hat,yr_hat); %K and Y' dot product
    end
end

```

```

dotz = dot(-K_hat,zr_hat); %K and Z' dot product
theta_ang = acos(dotz); %Theta (Elevation) angle
    between incident wave and rotated dipole
theta_angle_mult(n,t) = theta_ang; %Store previous
    theta angle for multiple scattering implementation
phi_ang = atan2(doty,dotx); %Phi (azimuth) angle
    between incident wave and rotated dipole
theta_hat = [cos(theta_ang)*cos(phi_ang)... %Theta
    unit vector for dipole on dipole coordinate system
    cos(theta_ang)*sin(phi_ang)... %
    -sin(theta_ang) ]; %
theta_hat_obs = [cos(theta_ang_obs)*cos(phi_ang_obs)
    ... %Theta unit vector for incident wave
    cos(theta_ang_obs)*sin(phi_ang_obs)... %
    -sin(theta_ang_obs) ]; %
theta_hat_obs_mult(:,t) = theta_hat_obs;
phi_hat = [-sin(phi_ang) cos(phi_ang) 0];
theta_hat_prime1 = T*theta_hat.';
phi_hat_prime = T*phi_hat.';
theta_prime_mult(:,n,t) = theta_hat_prime1;
R = 100; %Distance from
    source to origin (meters)
Rt = dot(K_hat,pnts(:,n).')+R; %Distance from
    source to scatterer
Rr(n,t) = Rt;
V_oc = ((-1*eta*k*b*exp(1i*k*Rt))/(2*w*mu*Rt))*sin(
    theta_ang)*dot(theta_hat_obs,theta_hat_prime1); %
    Open circuit voltage on dipole
I_dipole = V_oc/Z; %Current induced on dipole
I_dipole_mult(t,n) = I_dipole_mult(t,n) + I_dipole;
E_dipole = ((1i*eta*k*I_dipole*b*exp(1i*k*Rt))/(8*pi*
    Rt))*sin(theta_ang)... %ETheta field radiated by
    dipole by induced current
    *((dot(theta_hat_prime1.',theta_hat_obs))^2)*
    theta_hat_obs; %
E_no_mul(:,t) = E_dipole.' + E_no_mul(:,t);
dI_dipole = zeros(1,sctrs);
for m = 1:sctrs
    r1 = pnts(1:3,n)-pnts(1:3,m);
    dotx = dot(r1,xr_hat);
    doty = dot(r1,yr_hat);
    dotz = dot(r1,zr_hat);
    theta1 = acos(dotz);
    phi1 = atan2(doty,dotx);
    m1 = sqrt(sum((r1).^2));

```

```

theta_hat = [cos(thetal)*cos(phi1) cos(thetal)*sin(
    phi1) -sin(thetal)];
theta_hat_prime1 = T*theta_hat.';
ca = cos(alpha(m)); cb = cos(beta(m)); cg = cos(
    gamma);
sa = sin(alpha(m)); sb = sin(beta(m)); sg = sin(
    gamma);
Tr = [ ca*cb*cg-sa*sg -ca*cb*sg-sa*cg ca*sb; ... %z
    -y'-z'' convention so far, might change
    sa*cb*cg+ca*sg -sa*cb*sg+ca*cg sa*sb; ...
    -sb*cg sb*sg cb ];
ur_hat = Tr*[1 0 0; ...
    0 1 0; ...
    0 0 1];
xrr_hat = ur_hat(:,1);
yrr_hat = ur_hat(:,2);
zrr_hat = ur_hat(:,3);
dotx = dot(-r1,xrr_hat);
doty = dot(-r1,yrr_hat);
dotz = dot(-r1,zrr_hat);
theta2 = acos(dotz);
phi2 = atan2(doty,dotx);
theta_hat = [cos(theta2)*cos(phi2) cos(theta2)*sin(
    phi2) -sin(theta2)];
theta_hat_prime2 = Tr*theta_hat.';
V_oc = ((-1i*(eta^2)*(k^2)*(b^2)*I_dipole*exp(-1i*k
    *m1))/(16*pi*w*mu*m1))... %Open circuit voltage
    induced on mth dipole
    *sin(theta2)*sin(thetal)*dot(theta_hat_prime2,
    theta_hat_prime1);
dI_dipole(m) = V_oc/Z; %Current induced on
    mth dipole by nth dipole
end
dI_dipole(isnan(dI_dipole)) = 0;
I_dipole_mult(t,:) = I_dipole_mult(t,:) + dI_dipole; %
    <-----
end
E_no_mul(:,t) = abs(dot(E_no_mul(:,t),conj(E_no_mul(:,t))
    ));
end
...
for t = 1:length(el)
    for n = 1:sctrs
        E_dipole = ((1i*eta*k*I_dipole_mult(t,n)*b*exp(1i*k*Rr
            (n,t)))/(8*pi*Rr(n,t)))...

```

```

        *sin(theta_angle_mult(n,t))*(abs(dot(reshape(
            theta_prime_mult(:,n,t),1,3),theta_hat_obs_mult
            (:,t).'))^2);
    Etotal(:,t) = Etotal(:,t) + E_dipole*
        theta_hat_obs_mult(:,t);
    Ephase(:,t) = Ephase(:,t) + E_dipole*
        theta_hat_obs_mult(:,t);
end
Es(t) = abs(dot(Etotal(:,t),conj(Etotal(:,t))));
phase(t) = angle((sqrt(sum(real(Ephase(:,t)).^2))+1i*sqrt
    (sum(imag(Ephase(:,t)).^2)))/(exp(1i*k*R)/R))*(180/pi)
;
end
rscs_mult = 10*log10((4*pi*(R^2)*(Es(:)))/(1/R^2)).');

```

## B.4 Plate Multiple Scattering

The following script is used to compute the RCS of plates with multiple scattering.

Listing B.7: Multiple scattering script for plates

```

%%% Loop to obtain angles and distance from source to target
%%%
for m = 1:sctrs
    for n = 1:length(theta_i)
        ca = cos(alpha(m)); cb = cos(beta(m)); cg = cos(gamma(
            m)); %Sines and Cosines for transformation matrix
        sa = sin(alpha(m)); sb = sin(beta(m)); sg = sin(gamma(
            m));
        T_local = [ ca*cb*cg-sa*sg ca*cb*sg+sa*cg -ca*sb; ...
            %Global vector transformed to local coordinates
            -sa*cb*cg-ca*sg -sa*cb*sg+ca*cg sa*sb; ...
            sb*cg sb*sg cb ];
        K_hat = [-sin(theta_i(n)) 0 -cos(theta_i(n))]; %Unit
            K vector from incident direction
        R_hat_prime = T_local*K_hat.'; %R hat
            vector transformed to local coordinates
        dotx = dot(-R_hat_prime,X_hat); %Dot
            product of R_hat' and X_hat
        doty = dot(-R_hat_prime,Y_hat); %Dot
            product of R_hat' and Y_hat
        dotz = dot(-R_hat_prime,Z_hat); %Dot
            product of R_hat' and Z_hat
        theta_ang(n,m) = acos(dotz); %Theta
            angle between incident wave and n_hat
    end
end

```

```

        phi_ang(n,m) = atan2(doty,dotx);                                %Phi
        angle between incident wave and n_hat
        Rt(n,m) = dot(K_hat,pnt(m,:))+R;                                %Range
        from source to center of plate (R+R')
    end
end
...
%%% Loop to calculate Multiple Scattering Fields %%%
for n = 1:sctrs
    for m = 1:sctrs
        if n==m

        else
            %%%Secondary reflecting plate, m
            ca = cos(alpha(m)); cb = cos(beta(m)); cg = cos(
                gamma(m)); %Sines and Cosines for transformation
                matrix
            sa = sin(alpha(m)); sb = sin(beta(m)); sg = sin(
                gamma(m));
            T_local = [ ca*cb*cg-sa*sg ca*cb*sg+sa*cg -ca*sb;
                ... %Global vector transformed to local
                coordinates
                -sa*cb*cg-ca*sg -sa*cb*sg+ca*cg sa*sb; ...
                sb*cg sb*sg cb ];
            point = T_local*(pnt(m,:)-pnt(n,:)).'
            mag_point = sqrt(sum(point.^2));
            Rr = sqrt(sum((pnt(m,:)-pnt(n,:)).^2));
            dotx = dot(-point./mag_point,X_hat);
            doty = dot(-point./mag_point,Y_hat);
            dotz = dot(-point./mag_point,Z_hat);
            theta_ms = acos(dotz)
            phi_ms = atan2(doty,dotx)

            %%%Primary reflecting plate, n
            ca = cos(alpha(n)); cb = cos(beta(n)); cg = cos(
                gamma(n)); %Sines and Cosines for transformation
                matrix
            sa = sin(alpha(n)); sb = sin(beta(n)); sg = sin(
                gamma(n));
            T_local = [ ca*cb*cg-sa*sg ca*cb*sg+sa*cg -ca*sb;
                ... %Global vector transformed to local
                coordinates
                -sa*cb*cg-ca*sg -sa*cb*sg+ca*cg sa*sb; ...
                sb*cg sb*sg cb ];
            point = T_local*(pnt(n,:)-pnt(m,:)).';

```

```

mag_point = sqrt(sum(point.^2));
dotx = dot(-point./mag_point,X_hat);
doty = dot(-point./mag_point,Y_hat);
dotz = dot(-point./mag_point,Z_hat);
theta_is = acos(dotz)
phi_is = atan2(doty,dotx)

X = ((k*a)/2)*((sin(theta_s(:,n)).*cos(phi_s(:,n)))
+ (sin(theta_i(:,n)).*cos(phi_i(:,n)))); %X
    variable for sinc function
Y = ((k*b)/2)*((sin(theta_s(:,n)).*sin(phi_s(:,n)))
+ (sin(theta_i(:,n)).*sin(phi_i(:,n)))); %Y
    variable for sinc function
N_phi_i = (2*a*b)*(H_i).*...
    ((cos(theta_i(:,n)).*sin(phi_i(:,n)).*sin(phi_s
    (:,n)))+( cos(theta_i(:,n)).*cos(phi_i(:,n)).*
    cos(phi_s(:,n)))).*...
    *(sinc(X/pi)).*(sinc(Y/pi));

X = ((k*a)/2)*((-sin(theta_i(:,n)).*cos(phi_i(:,n))
)+ (sin(theta_ms).*cos(phi_ms)));
Y = ((k*b)/2)*((-sin(theta_i(:,n)).*sin(phi_i(:,n))
)+ (sin(theta_ms).*sin(phi_ms)));
H_ms = 1i*((a*b*k)/(2*pi*eta)).*(exp((-1i*k.*(Rr)))
/Rr).*...
    ((cos(theta_i(:,n)).*sin(phi_i(:,n)).*sin(
    phi_ms))+(cos(theta_i(:,n)).*cos(phi_i(:,
    n)).*cos(phi_ms)))).*...
    *(sinc(X/pi)).*(sinc(Y/pi));
H_ms_store(:,m) = H_ms;

X = ((k*a)/2)*((sin(theta_s(:,n)).*cos(phi_s(:,n)))
);
Y = ((k*b)/2)*((sin(theta_s(:,n)).*sin(phi_s(:,n)))
);
N_phi_ms = (2*a*b.*(H_ms)).*...
    .*((cos(theta_is).*sin(phi_is).*sin(phi_s(:,n)
    )))+( cos(theta_is).*cos(phi_is).*cos(phi_s
    (:,n)))).*...
    *(sinc(X/pi)).*(sinc(Y/pi));
Efb_phi(:,n) = (1i*k/(4*pi)).*(exp(-2i*k*Rt(:,n)))
    *(-eta.*N_phi_i);
Esb_phi(:,n) = (1i*k/(4*pi)).*(exp(-1i*k*Rt(:,n)))
    *(-eta.*N_phi_ms);

```

```
        end
      end
    end
```